IEKP-KA/2015-22

Studies on the response behaviour of pixel detector prototypes at high collision rates for the CMS experiment

Zur Erlangung de akademischen Grades eines
DOKTORS DER NATURWISSENSCHAFTEN
von der Fakultät für Physik des
Karlsruher Institutes für Technologie

genehmigte

DISSERTATION

von

Dipl.-Phys. Andreas Kornmayer
aus Oberharmersbach

Tag der mündlichen Prüfung: 04.12.2015
Referent: Prof. Dr. Thomas Müller
Korreferent: Prof. Dr. Ulrich Husemann

Contents

Chapter 1

Introduction

The Large Hadron Collider (LHC) located at the European Center for Nuclear Research (CERN) finished its first successful running period in 2013. With the data collected from the collisions, produced by the world's largest particle accelerator, the existence of the Higgs Boson was proven [C+12]. This elusive particle was the last missing puzzle piece in the Standard Model of Particle Physics.

The performance of the LHC steadily increased since it was switched on. Starting its second run period in 2015 at maximum collision energy of 13.0 TeV it is expected that the LHC will reach an instantaneous luminosity of $1.5 \cdot 10^{34}\text{cm}^{-2}\text{s}^{-1}$ by the year 2018.

Due to their excellent position resolution, unambiguous hit positions and radiation hardness pixelated silicon particle detectors are currently the best choice of detector type for particle tracking in environments with high track density . Nowadays all major high energy particle physics experiments use some kind of pixelated detector close to the interaction point:

- The ATLAS detector uses silicon sensors with long pixels of $50\,\mu\text{m} \times 400\,\mu\text{m}$ read out by the FE chip.
- CMS has almost square silicon pixels, with a size of $150\,\mu\text{m} \times 100\,\mu\text{m}$, read out by the PSI46 readout chip.
- Belle II will use the DEpleted P-channel Field Effect Transistor technology with pixel sizes of $50\,\mu\text{m} \times 75\,\mu\text{m}$.

In the scope of this thesis two applications of silicon pixel detectors in the CMS experiment have been studied:

The Pixel Luminosity Telescope

The Pixel Luminosity Telescope (PLT) is a new component of the CMS detector for the second run period of the LHC. Eight three-layer particle telescopes, based on the CMS pixel readout chip, are placed close to the beam pipe on each end of CMS viewing the interaction point at a small angle. Each plane will provide a fast signal of the number of pixel clusters found at a rate of 40 MHz. The luminosity provided to CMS by the LHC is measured on a bunch-by-bunch basis by forming three-fold coincidences in the telescopes. The PLT will serve as a new, independent luminometer in CMS.

The CMS Pixel Detector Upgrade

The innermost layer of the CMS experiment, the CMS Pixel detector, was designed for an instantaneous luminosity of $1.0 \cdot 10^{34}\text{cm}^{-2}\text{s}^{-1}$. The better than expected performance of the LHC will push the detector over the limits of its capabilities. In order to maintain efficient and robust tracking at the CMS experiment the pixel detector needs to be replaced and improved. This replacement and upgrade of the CMS pixel detector is generally referred to as the *Phase 1 Upgrade*. For the upgrade a new readout chip,

the PSI46dig, was developed. The thesis at hand will describe this new chip in detail and focus on testing its capabilities at high particle rates to qualify it for the use in the CMS experiment.

After the introduction, the second chapter will give an overview of the LHC accelerator and the CMS experiment. This will place the presented work into the larger picture of the experiment.

The third chapter explains the theoretical basics of semiconductors, silicon and silicon sensors. The technology of hybrid pixel detectors is introduced.

The fourth chapter covers the two readout chips used in the PLT and the CMS upgrade. The data handling mechanisms of both chips are explained and the sources of random data loss are demonstrated. The differences between the PSI46v2 and the new PSI46dig are described.

Chapter five will cover the first example of a hybrid pixel detector used in the CMS experiment, the Pixel Luminosity Telescope. The mechanical setup of the PLT and its novel cooling structure are shown. The full readout chain of the detector is detailed to understand the results of the first threshold unification calibration performed on the full detector. Results from the first beam collisions observed with the PLT at its nominal position are shown.

The following three chapters, chapter six, seven and eight, will cover the setup, measurement and simulation of a high rate beam test for the new PSI46dig chip. By comparing measurements at highest particle rates with results from a full beam test simulation, a judgement on the qualification of the chip as the front-end readout chip of the upgaded CMS Pixel detector is given.

The last chapter summarises the work and gives recommendations for future beam tests of pixelated tracking detectors at high particle rates.

Chapter 2

The LHC and the CMS Detectors

2.1 The Large Hadron Collider

The Large Hadron Collider (LHC) is the world's largest and most powerful particle accelerator. With a circumference of 27 km the LHC is also the world's biggest machine. Its purpose is to accelerate particles, protons or lead ions, to relativistic velocities close to the speed of light. Two particle beams are being accelerated, one clockwise, the other counterclockwise, and collided in four distinct points around the accelerator ring. In 2010, following a two year downtime due to an accident, the LHC started to collide protons with a centre of mass energy of 7 TeV. In 2012 the collision energy was increased to 8 TeV. After the first Long Shutdown (LS1) in the years 2013 and 2014 the centre of mass collision energy $\sqrt{s}$ was increased to 13 TeV. The limiting factor for the collision energy of the LHC is the magnetic field strength to bend the proton or ion beams to a radius of about 2.8 km. The LHC is built from 9593 superconducting magnets. These magnets are cooled down by liquid helium to cryogenic temperatures of 1.9 K and create magnetic field strengths of up to 8.3 T to bend and focus the beams. The LHC tunnel is not a perfect circle, but contains eight straight sections where the experiments and services for the synchrotron are located.

The Accelerator Chain

The accelerator chain of the LHC is demonstrated using the example of a proton beam. A proton beam is created from hydrogen gas by stripping off the electrons in a Duroplasmatron. These protons are injected into a linear accelerator (Linac 2) and accelerated to an energy of 50 MeV. From here the proton beam reaches the Proton Synchrotron Booster (PSB) where it is further accelerated to 1.4 GeV. The particles pass two further accelerator stages before reaching the LHC: first the Proton Synchrotron (PS) where the particles reach an energy of 26 GeV and then the Super Proton Synchrotron with 450 GeV. In this step the beam also receives its 25 ns bunch spacing that it will keep in the LHC. From the SPS many experiments and beam lines are supplied with particle beams. After the LHC has been filled with particles circulating at an energy of 450 GeV they are further accelerated, or 'ramped up', to the desired collision energy of 6.5 TeV, resulting in a center-of-mass energy of 13 TeV.

Experiments at the LHC

International collaborations built particle physics experiments at the four collision points of the LHC. The two general purpose detectors, CMS (Compact Muon Solenoid) and ATLAS (A Toroidal LHC ApparatuS), are designed to cover various fields of interest in the physics world, from measuring the properties of the Higgs boson discovered in 2012 to discovering new physics beyond the Standard Model. The ALICE (A Large Ion Collider Experiment) and the LHCb (Large Hadron Collider Beauty) experiments are more specialised in their purpose.

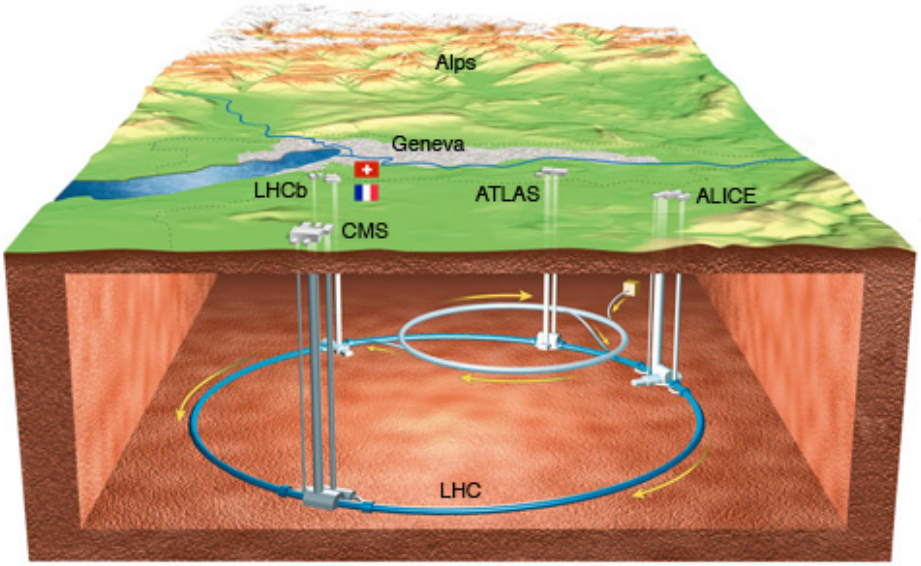

Figure 2.1: **The LHC Ring** [LHC15]
A schematic of the LHC accelerator ring and the four big experiments underneath Geneva and the Jura mountains.

ALICE is designed to research lead-lead collisions and the quark-gluon plasma they produce during special run periods of the accelerator and LHCb is built to measuring CP-violation in the decays of b-hadrons.

2.2 Luminosity

Two key parameters determine the performance of any collider experiment: the beam energy and the luminosity. The luminosity is a measure for the ability of a partcile detector to create particle collisions. For an interaction with a cross section σ_p the instantaneous luminosity $\mathcal{L}$ is defined as

$$\frac{dN_p}{dt} = \mathcal{L} \cdot \sigma_p, \tag{2.1}$$

with the rate of interesting events $\frac{dN_p}{dt}$. Therefore, instantaneous luminosity is measured in units of $\mathrm{cm}^{-2}\mathrm{s}^{-1}$.

The ultimately important number for any particle collision experiment is the integrated luminosity $\mathcal{L}_{\mathrm{int}}$, which is defined as the integral of the instantaneous luminosity over the sensitive time of the experiment

$$\mathcal{L}_{\mathrm{int}} = \int_0^{\mathrm{T}} \mathcal{L}(t)dt. \tag{2.2}$$

The number of events recorded in an experiment like CMS or ATLAS is then directly proportional to the integrated luminosity.

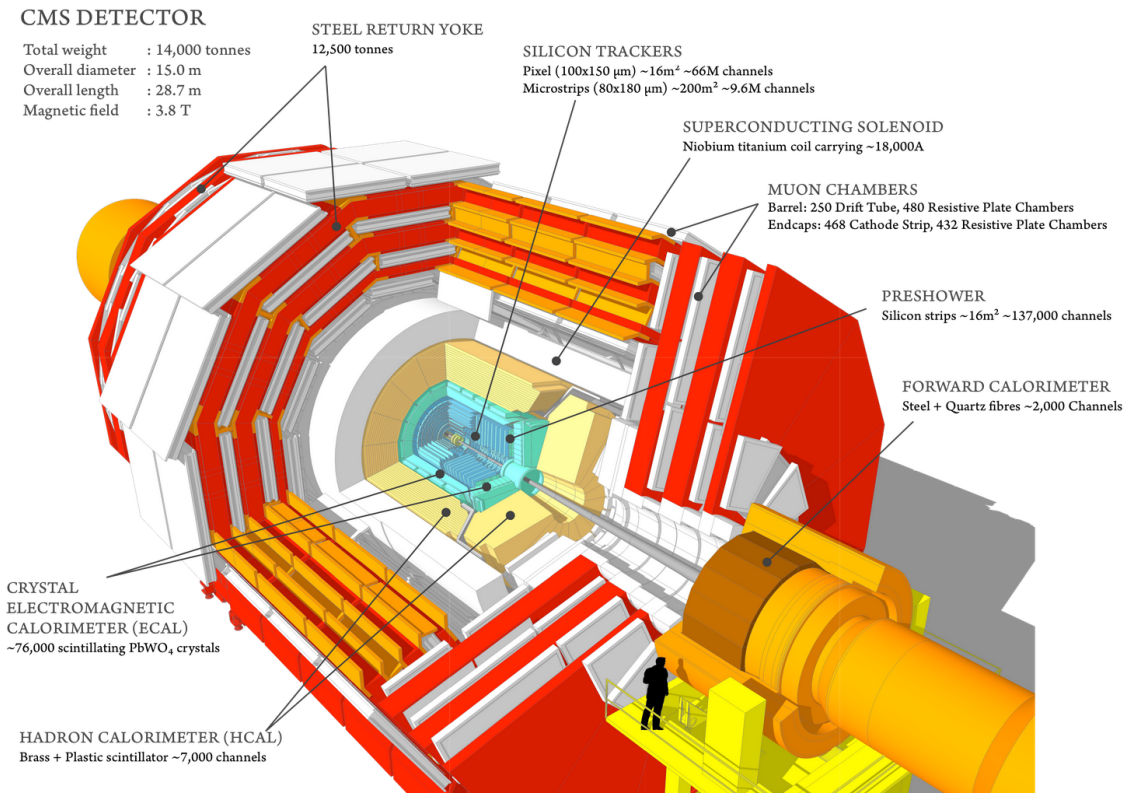

Figure 2.2: **The CMS Detector** [SM14]

2.3 The Compact Muon Solenoid

The Compact Muon Solenoid (CMS) is a general purpose particle physics experiment. Just like the ATLAS experiment it detects the decay products of the particle collisions created by the LHC synchrotron. The purpose of both of these experiments are to research the physics at the Terascale, study the properties of the newly found Higgs-Boson and compare it to predictions from the Standard Model of particle physics and to look for new physics beyond this Standard Model, such as Supersymmetry (SUSY) or extra dimensions. CMS is built in several layers, each measuring a specific property of the decay products of the particle collisions while they traverse the detector.

The magnet

All of the CMS Tracker (see below) and the calorimeters of CMS (described later in the text) are immersed within a uniform magnetic field of 3.8T produced by a superconducting NbTi solenoid. Charged particles moving inside this magnetic field are forced on a curved trajectory by the Lorentz force. The high field strength results in a good resolution ($\approx 10\%$) on the measurement of a particle's momentum for energies up to 1TeV [Col06].

The tracking volume

The inner most part of the CMS experiment is reserved for a high resolution tracking detector made of two parts, the CMS Pixel detector and the CMS Strip Tracker. To track the path a particle takes within the high magnetic field of CMS, three pixel layers and ten strip tracker

layers in the barrel region and two pixel layers and 14 strip tracker layers each in the two forward region detect the passing particle and take position measurements.

The CMS Pixel detector

The detector closest to the interaction point is the CMS Pixel detector. In the barrel region it consists of three concentrical cylinders around the beam pipe at radii of 4.4 cm, 7.3 cm and 10.2 cm. At ±34.5 cm and ±46.5 cm the forward disks are placed on each end of CMS. In total 66 million pixels are distributed over a surface area of 1.06 m^2. With a pixel size of 100 μm by 150 μm the pixel detector delivers a measurement of the three-dimensional track with an resolution of 10−20 μm. This information is used to do a fast online track reconstruction in the High Level Trigger (HLT) for primary vertex reconstruction, electron/photon identification, muon reconstruction, tau identification and b-tagging [Col12]. Because of its proximity to the interaction point the Pixel detector has to withstand an overall fluence of $1.6 \cdot 10^{14}$–$32.0 \cdot 10^{14}$ n_{eq}/cm^2[1] during its lifetime in CMS [Col06], until is is replaced at the end of the year 2016 in the Phase 1 Upgrade described in section 2.4.

The CMS Tracker

The CMS Silicon Strip Tracker, as the name implies, is made entirely from silicon sensors. With an overall surface of more than 200 m^2 and 10 million readout channels it is the largest silicon-only tracking device ever built for a high energy particle physics experiment [Col06]. By measuring the track a charged particle follows within the solenoid's magnetic field it is possible to provide precise momentum and charge information. This information is essential in reconstructing the decay processes occurring in the proton-proton collisions.

Within the Tracker there are four different regions, Tracker Inner Barrel (TIB), Tracker Inner Disks (TID), Tracker Outer Barrel (TOB) and Tracker End Cap (TEC). Each region has a special configuration of sensor thickness. The strip length and pitch-to-width ratio was matched to the particular conditions of the region, taking future radiation damage, cooling power or material budget among other things into consideration.

The electromagnetic calorimeter

The electromagnetic calorimeter (ECAL) measures the energy of particles that interact only or mostly through the electromagnetic force, such as photons or electrons. It is made from 80.000 lead tungstate scintillator crystals. Electromagnetically interacting particles stop in the ECAL and deposit all their energy in an electromagnetic shower. This energy is converted in the scintillator into a light pulse proportional to the amount of deposited energy. A photodiode at the base of each crystal translates the light pulse into an electrical signal for the readout electronics.

The hadron calorimeter

The hadron calorimeter (HCAL) is a so called sampling calorimeter. It consist out of interleaved layers of brass absorbers and scintillator material. It is used to measure the energy of neutral hadrons (neutron, π^0, etc.) and charged hadrons (proton, $\pi^{\pm}$, etc.).

[1] The NIEL (Non Ionising Energy Loss) hypothesis states that any flux of ionising particles can be scaled to the a flux of 1 MeV neutrons creating the same damage in the detector. The unit is given in 'equivalent neutrons per area': $[\phi] = n_{eq}/cm^2$

The muon system

The outermost layer of the CMS detector is reserved for the muon system. Unlike other particles the muons produced in particle collisions are not being stopped in the calorimeters Muons penetrate the entire detector. This can be understood from the Bethe formula (3.19) describing the energy loss of a particle in a material. Due to its high mass m the muon loses only little energy, compared to an electron, when passing through material. The muon system is a very important part of CMS and played an integral role in discovering the Higgs-Boson. The decay of a Higgs-Boson into two Z-Bosons and their subsequent decay into four leptons ($H \rightarrow 4l$) leaves a distinctive signal in the detector with little background.

Luminosity measurement

The luminosity delivered to the CMS experiment is measured in two different modes. The offline luminosity measurement is done by cluster counting in the second and third barrel layer of the CMS Pixel detector. The Pixel detector can only be operated during stable beam conditions, thus only providing an offline measurement of the luminosity.

Several online luminometers exist in CMS: the Pixel Luminosity Telescope (described later in detail in chapter 5), the Beam Conditions Monitor and the Hadron Forward Calorimeter. These three detectors can be operated independent of the status of the beam in the LHC. They provide a real-time measurement of the bunch-by-bunch luminosity in CMS.

During the first running period of the LHC, the CMS detector collected a total integrated luminosity of $23.3\,\mathrm{fb}^{-1}$ at a centre-of-mass collision energy of 8 TeV.

2.4 The Phase 1 Pixel Upgrade

During an extended winter shutdown of the LHC in the year 2016/2017 it is planned to exchange the entire CMS Pixel detector. This opportunity will be used to replace the radiation damaged sensor material, improve the sensor cooling system and also prepare the data readout for the high instantaneous luminosity provided by the LHC, surpassing assumptions made during the construction of the current Pixel detector. The entire CMS Pixel detector will be replaced by a new detector with more layers in the barrel and forward part, improved front-end readout chip and lighter detector mechanics.

2.4.1 Upgrade Mechanics

One of the most important upgrades made to CMS, making the changes in the CMS Pixel detector possible, was the replacement of the central beam pipe during Long Shutdown 1 in 2014. The old beam pipe of CMS had a diameter of 59.6 mm at its thinnest part. It was replaced by the new beam pipe with a smaller diameter of only 45 mm and a wall thickness of 0.8 mm. The innermost layer of the upgraded pixel detector will be able to move as close as 3.0 cm to the interaction point, making space for an additional fourth layer of pixel detectors in the barrel region. The radius of each layer, the number of facets per layer and the number of modules per layer for the new barrel pixel detector can be seen in table 2.1.

One of the requirements for the upgraded pixel detector is that the material budget inside the detector volume should not be increased, to keep the number of nuclear interaction with inactive material low. This is achieved by moving connectors and auxiliary electronics into the region of pseudorapidity $|\eta| > 2.5$ (see figure 2.3). Additionally the cooling tubes for the new CO_2 cooling will double as mechanical support structure. Compared to the current

Table 2.1: **Radii of the new Pixel detector layers**

layer	radius (mm)	facets	modules
1	30	12	96
2	68	28	224
3	109	44	352
4	160	64	512

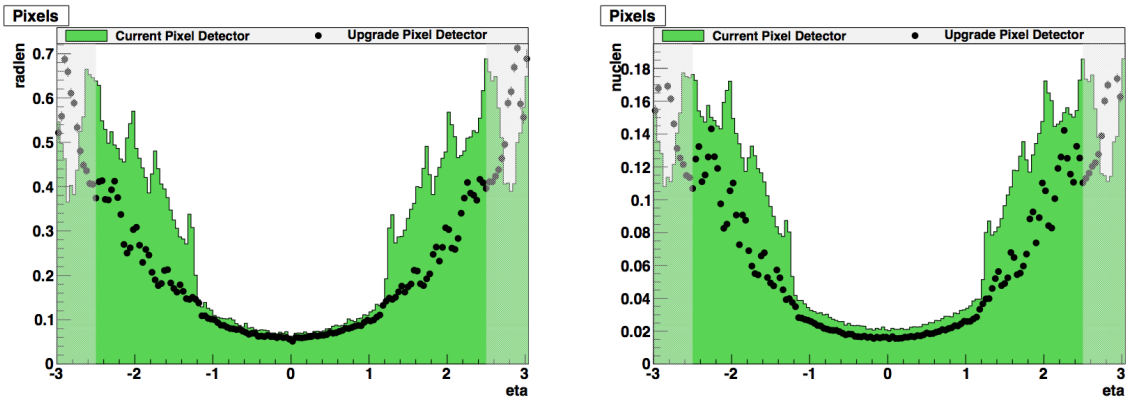

Figure 2.3: **Material budget of the current detector compared to the Phase 1 upgrade**
(left) The figure on the left shows the detector's material amount in units of radiation length as a function of η. (right) The plot on the right shows the material budget in units of nuclear interaction length. In both plots the histogram in green shows the detector currently installed in CMS whereas the black dots show the simulation of the Phase 1 Upgrade detector [Col12].

detector the cooling tubes are smaller in diameter and change from liquid C_6F_{14} cooling to a two phase CO_2 cooling reduces the amount of material in the tracking region significantly, see figure 2.3.

Similar to the upgrade of the CMS Barrel pixel detector, the CMS Forward Pixel detector is also extended by an additional disk on each end. In total the F-Pix will have three disks on each end of CMS, positioned at $\pm z = 291$, 366 and 461 mm from the interaction point.

2.4.2 Electronics Upgrade

One essential part of the CMS Phase 1 Upgrade of the Pixel detector is the upgrade of the front end and back end electronics. The readout of the current Pixel detector is based on the PSI46v2 readout chip. This chip will be replaced by the PSI46dig, the readout chip for the second, third and fourth layer of the new Barrel Pixel detector and all three forward disks. Both chips will be explained in chapter 4. The first layer will be equipped with a further evolution, the Layer-1 chip.

The readout chips are grouped to modules, each containing 16 ROCs and controlled by a Token Bit Manager chip. While for the current detector many different modules and half-module types existed, the production process and construction for the new Pixel detector is made as simple as possible. All pixel modules in the barrel and forward region of the new

detector are built identically.

The service electronics for the upgraded CMS Pixel detector will be housed by eight service cylinder half shells. They are positioned at both ends of the CMS experiment just outside the pixel detector. The service cylinders hold all electronics that are responsible for providing the detector with low-voltages [Kle14] and the conversion of electrical signals to optical signals and vice versa.

For the Phase 1 Upgrade of the CMS Pixel detector a new high speed μTCA based data acquisition system will replace the current VME-based system. 56 new Front-End Drivers (FEDs) will be needed to for the new DAQ system. The FEDs receive and decode the data coming from the detector modules. The detector is controlled by the Front-End Controllers, that manage the detector slow control and the programming of detector parameters in the ROCs and TBMs. Additional electronics is needed for the clock and trigger signals coming centrally from CMS.

Chapter 3

Semiconductor Tracking Detectors

Over the last decades semiconductor detectors gained in importance in high energy particle physics. They are mostly used as tracking detectors but developments are made to use them as calorimeters as well. The basic principles needed to understand the physics and the working principle of a semiconductor detector are given in this chapter.

3.1 Semiconductor Physics

A semiconductor is a material that acts as an isolator at 0K but becomes conductive at higher temperatures. Distinctive for semiconductors is the small band gap energy between valence band and conduction band and a strong temperature dependence of the electrical conductivity. Since the discovery of the rectifier effect by Ferdinand Braun in 1874 and the development of the pn-junction, transistors and semiconductor hetero structures, semiconductors have become vital part of everyday life and many applications in physics.

Semiconductor band structure

To calculate the eigenstates of the electrons in a semiconductor one has to solve the Schrödinger equation. For a solid with 10^{23} atoms per cubic centimetre this problem is not trivially solvable and several approximations have to be made.

Born Oppenheimer Approximation:
The mass of the atomic nucleus in a solid is much higher than the mass of the electrons ($m_{\text{atom}} \gg m_{\text{electron}}$) and the electrons' movements follow adiabatically the nuclei's movements. The Schrödinger equation can be solved for a fixed lattice. Interactions between electrons and phonons have to be considered by perturbation theory.

Neglecting Valence Electrons:
The valence electrons are bound to the core of the atom. Only the free electrons of the conduction band describe properties such as chemical bonds, optical transitions or conductivity. The interaction of free electrons and the inner valence electrons can be described by an effective potential V_{eff}.

One Electron Approximation:
The Coulomb term of the Schrödinger equation does not allow for a separation ansatz, it can only be calculated by approximation. By variation of the energy this approximation can be optimised and the Hartree equation for a single electron is obtained.

$$\left[-\frac{\hbar^2}{2m_0}\Delta_j + V_{\text{eff}}(\mathbf{r}_j) + e^2 \sum_{i \neq j} \int \frac{|\phi_i(\mathbf{r}_i)^2|}{|\mathbf{r}_i - \mathbf{r}_j|} d\tau \right] \phi_j(\mathbf{r}_j) = E_j \phi_j(\mathbf{r}_j) \tag{3.1}$$

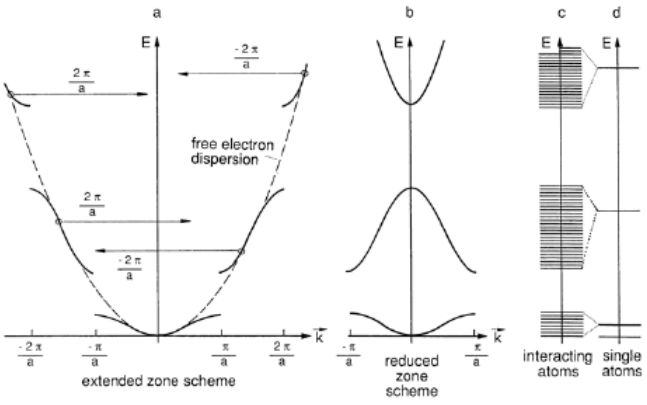

Figure 3.1: **Reduced zone scheme**
Reduced zone scheme (**b**) of the energy bands in a crystalline solid state body. Derived from the free electron (**a**) or atomic orbitals (**c**,**d**). [Kli07]

Here $\hbar$ is the reduced Planck constant, m_0 is the mass of the electron, Δ_j is the Laplace operator for electron j, ϕ_j is the one particle wave function of electron j and E_j are the Eigenstates of electron j in the semiconductor. Taking also the Pauli principle into consideration one reaches the Hartree Fock equation

$$\left[-\frac{\hbar^2}{2m_0}\Delta_j + V_{\text{eff}}(\mathbf{r}_j) + e^2\sum_{i\neq j}\int\frac{|\phi_i(\mathbf{r}_i)^2|}{|\mathbf{r}_i-\mathbf{r}_j|}d\tau\right]\phi_j(\mathbf{r}_j)$$
$$-e^2\sum_{i\neq j}\int\frac{\phi_i^*(\mathbf{r}_i)\phi_j(\mathbf{r}_i)}{|\mathbf{r}_i-\mathbf{r}_j|}d\tau\phi_i(\mathbf{r}_i) \quad = \quad E_j\phi_j(\mathbf{r}_j). \tag{3.2}$$

Averaging over the fields one arrives at the Schrödinger equation for a single particle

$$\left[-\frac{\hbar^2}{2m_0}\Delta + \tilde{V}_{\text{eff}}(\mathbf{r})\right]\Psi(\mathbf{r}) = E\Psi(\mathbf{r}) \tag{3.3}$$

The effective potential $\tilde{V}_{\text{eff}}$ contains the Coulomb interaction as well as the exchange interaction and the electronic correlation between two electrons.

Bloch wave

The Schrödinger equation for a single particle, equation 3.3, can be solved by the class of Bloch functions. Since the Hamiltonian in a periodic lattice is invariant under translation by a lattice vector $\vec{R}$ the following approach for the wave function $\Psi_n(\vec{k},\vec{r})$ is used:

$$\Psi_n(\vec{k},\vec{r}) = e^{i\vec{k}\vec{r}}u_n(\vec{k},\vec{r}) \tag{3.4}$$

Functions of this type are called Bloch waves. The reciprocal latice vector is denoted as $\vec{k}$ and $u_n(\vec{k},\vec{r})$ are periodic functions in $\vec{r}$. There are two explanations for the development of a band structure in semiconductors:

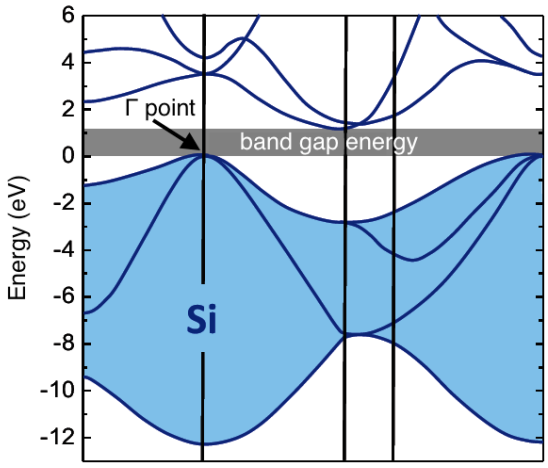

Figure 3.2: **Reduced zone scheme of Silicon**
Silicon is an indirect semiconductor with a band gap energy of 1.17 eV [GM12].

Nearly Free Electron Model:
In this model the electrons can move quasi freely through the solid state body, quantum mechanically they are described as waves. At the edge of the Brillouin zone, the smallest subsection of the reciprocal lattice, reflexions occur. At these points the energy levels split into allowed and forbidden areas, see figure 3.1(a). The energy levels occupied by electrons are called bands.

Tight Binding Model:
For a single atom the electrons have discrete energy levels. Within a solid state body a lot of atoms congregate and the quantum mechanical wave functions overlap. Through the interaction of the orbitals the energy levels split. The multitude of atoms creates quasi-continuous energy bands, as shown in figure 3.1(c)(d).

Based on the band structure one can differentiate between two different types of semiconductors, the ones with a **direct** band gap and the ones with an **indirect** band gap. In a semiconductor with direct band gap the conduction band minimum is above the valence band maximum at $\vec{k} = 0$, also known as the Γ-point. Examples of this kind of semiconductor material are GaAs or GaP. A semiconductor with a shifted valence band maximum and conduction band minimum in $\vec{k}$ is called an indirect semiconductor. The reduced zone scheme of the indirect semiconductor silicon is shown in figure 3.2.

3.1.1 Intrinsic semiconductors

Semiconductor materials that contain no impurity atoms are called intrinsic semiconductors. At room temperature a small number of electrons has been exited by thermal energy from the valence band into the conduction band. Contrary to metals the conductance of semiconductors increases with temperature.

Electrons are fermions, thus obeying the Pauli exclusion principle. Their energy distribution follows Fermi-Dirac statistics, see e.g. [Gri05].

$$f(E,T) = \frac{1}{e^{(E-E_F)/k_B T} + 1} \tag{3.5}$$

where k_B is the Boltzmann constant, T the absolute temperature and E_F the Fermi energy. The density of states for electrons and holes is given by

$$D_h = \frac{V}{2\pi^2}\left(\frac{2m_h^*}{\hbar^2}\right)^{3/2}\sqrt{-E} \tag{3.6}$$

$$D_e = \frac{V}{2\pi^2}\left(\frac{2m_e^*}{\hbar^2}\right)^{3/2}\sqrt{E-E_g} \tag{3.7}$$

Using these equations the density of free charge carriers in the intrinsic semiconductor can be calculated, see e.g. [Har09].

$$n = \int_0^\infty D(E)\cdot f(E,T)\,\mathrm{d}E \tag{3.8}$$

The electron density in the conduction band is

$$n = \underbrace{2\left(\frac{m_e^* k_\mathrm{B} T}{2\pi\hbar^2}\right)^{3/2}}_{N_C} e^{-\frac{E_C-E_F}{k_\mathrm{B}T}}. \tag{3.9}$$

The hole density in the valence band is

$$n = \underbrace{2\left(\frac{m_h^* k_\mathrm{B} T}{2\pi\hbar^2}\right)^{3/2}}_{N_V} e^{-\frac{E_F-E_V}{k_\mathrm{B}T}}. \tag{3.10}$$

From the fact that in an intrinsic semiconductor the number of holes and electrons has to be the same at all times, the Fermi energy can be determined.

$$n = p \Rightarrow E_F = \frac{1}{2}E_g + \frac{3}{4}k_\mathrm{B}T\ln\left(\frac{m_h^*}{m_e^*}\right) \tag{3.11}$$

Additionally this results in the mass action law, valid in intrinsic and extrinsic semiconductors.

$$n\cdot p = n_i^2 = N_C N_V e^{\frac{-E_g}{k_\mathrm{B}T}}\ . \tag{3.12}$$

3.2 Extrinsic semiconductors

Often the intrinsic charge carrier concentration of a semiconductor material is too low to be used in electrical devices. To increase this concentration by several orders of magnitude the semiconductor material has to be doped with impurities. An extrinsic semiconductor is a semiconductor that has been doped. For semiconductor technology the ability to design materials and electrical devices by doping is vital.
Two different types of doping can be distinguished. When doping a semiconductor with donors one speaks of an **n-type** material. The donors emit an additional electron into the conduction band. Adding acceptors to the semiconductor creates a **p-type** semiconductor. The acceptor traps an electron from the valence band and creates a free hole.
In the following part the different types of doping for silicon (Si), a tetravalent semiconductor, will be discussed.

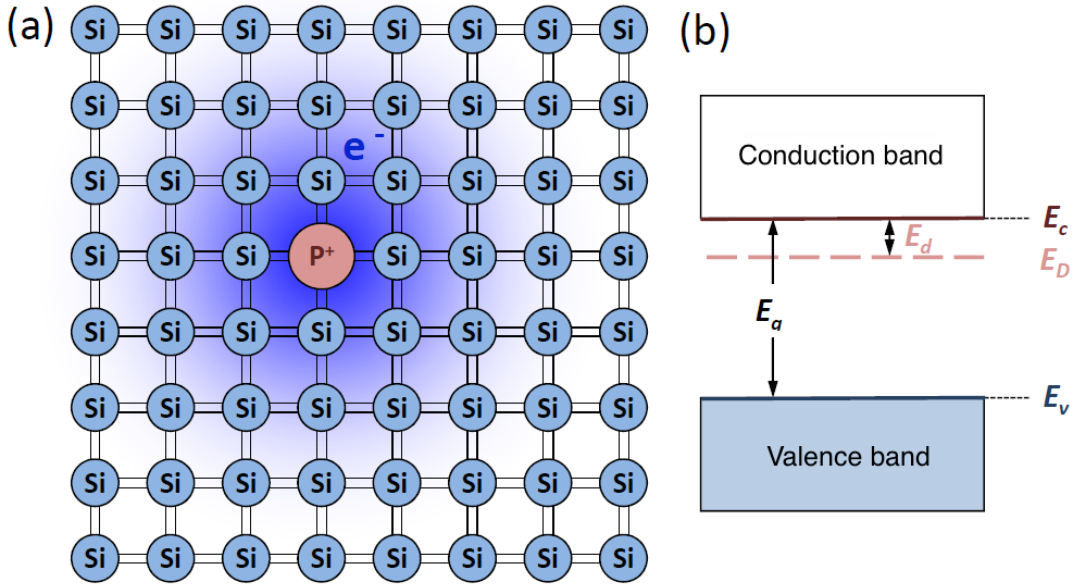

Figure 3.3: **n-type doped silicon**
(a) Phosphorus atom in a silicon crystal lattice. (b) energy level of a donor, E_d is the ionisation energy necessary to elevate the electron into the conduction band [GM12].

n-type semiconductors

Within silicon, elements from the 5th main group of the periodic table, such as phosphorus, arsenic or antimony, act as electron donors (see figure 3.3). Only four of the five available valence electrons are used to form a covalent bond within the crystal lattice of silicon. The remaining electron is only weakly bound to the atomic core and can be released by a very small excitation energy. Thereby a free electron is available for the conduction band. The energy level of the donor is just below the conduction band. The majority charge carriers in n-type semiconductors are electrons.

p-type semiconductors

Silicon can also be doped with atoms from the 3rd main group like boron or aluminium. If one of these atoms replaces a silicon atom in the crystal lattice one electron is missing to form the covalent binding to the neighbouring atoms (see figure 3.4). This hole can be easily populated by another electron, thus creating a wandering hole. The impurity acts as an electron acceptor with an energy level just above the valence band. The majority charge carriers of p-type semiconductors are holes. Only few free electrons exist in the conduction band, electrons are the minority carriers.

3.2.1 pn-junction

The system of two half-infinite semiconductors, one n-type, the other p-type, can be reduced to a one-dimensional problem (see figure 3.5(a)). While the two halves are still separated the chemical potentials μ are on different levels: slightly above the acceptor level in the p-type

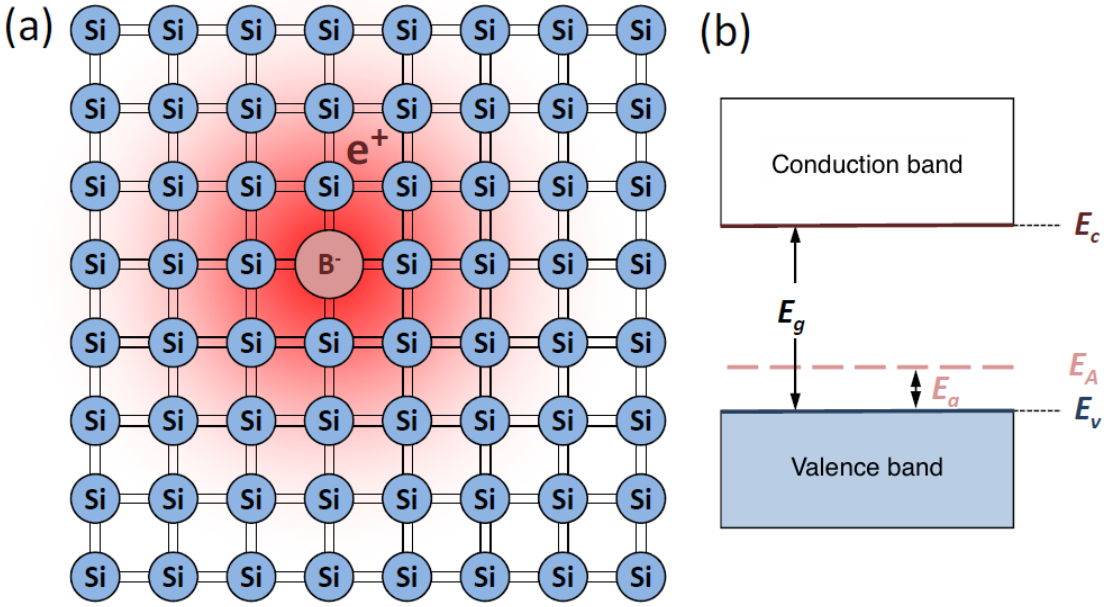

Figure 3.4: **p-type doped silicon**
(a) Boron atom in a silicon crystal lattice. (b) energy level of an acceptor, E_a is the energy needed for an hole to move to the valence band. [GM12]

and slightly below the donor level in the n-type.
As soon as both halves are in contact the chemical potential has to be in thermodynamic equilibrium over the entire semiconductor and the chemical potential has a constant value everywhere, as shown in figure 3.5(b). This results in an adjustment of the band structure in the different doping regions, best described by the creation of the potential ϕ. The difference in majority carrier and minority carrier densities in the two halves leads to diffusion of these charge carriers (see figure 3.5(c)). Electrons diffuse from the n-type to the p-type semiconductor where they recombine with holes, the leading majority carriers. Similarly holes from the p-type semiconductor diffuse into the n-type and recombine with the electrons. The boundary surface is depleted of moving charge carriers. The missing charge creates a positive space charge region in the n-type and a negative space charge region in the p-type. The electric field associated with this space charge region leads to a drift current, also called generation current. In thermodynamic equilibrium the diffusion current and the drift current are equal in absolute value but opposite in direction.

The diffusion voltage can be calculated by

$$U_D = \phi(\infty) - \phi(-\infty) = \frac{k_\mathrm{B} T}{e} \ln\left(\frac{n_n \cdot n_p}{n_i^2}\right), \tag{3.13}$$

where ϕ is the electric potential, n_n the donor density in the n-doped material, n_p the acceptor density in the p-doped semiconductor and n_i the intrinsic charge carrier density.

Using the Schottky approximation also the width of the space charge region can be determined. For this the pn-junction is assumed to be abrupt and the change in free charge carrier concentration can be estimated by a Heaviside function. Under these preconditions the Poisson equation is solvable, see e.g. [GM12].

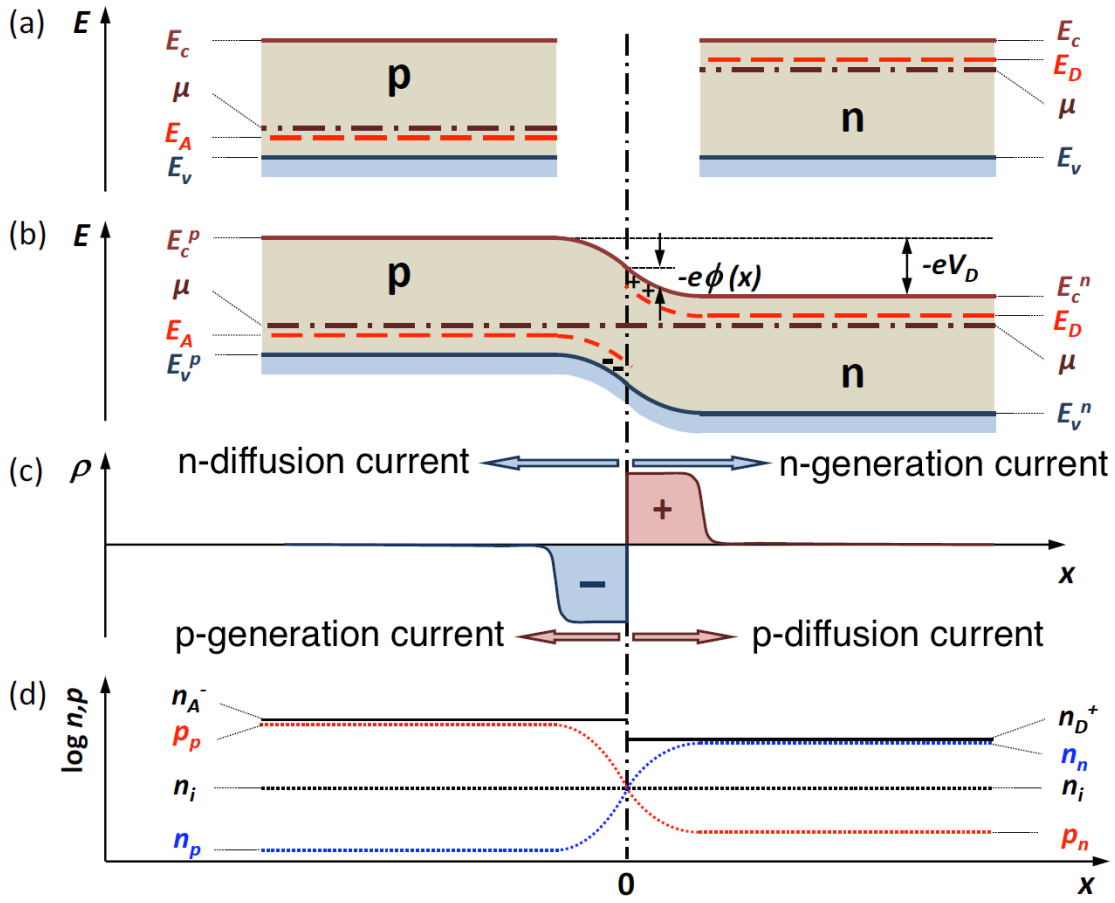

Figure 3.5: **pn-junction**
(a) energy levels in seperated half-infinite semiconductors, (b) energy levels after contact of semiconductors in thermodynamic equilibrium, (c) space charge and currents, (d) charge carrier concentration in both halves of the pn-junction [GM12].

$$\frac{\partial^2\phi}{\partial x^2} = \frac{e}{\epsilon\epsilon_r}\begin{cases}0 & \text{if } x < x_p\\ N_A & \text{if } x_p < x < 0\\ N_D & \text{if } 0 < x < x_n\\ 0 & \text{if } x > x_n\end{cases} \tag{3.14}$$

$\Rightarrow$ Solution :

$$\phi = \begin{cases}-N_A x_p^2 & \text{if } x < x_p\\ N_A\left(x^2 - 2xx_p\right) & \text{if } x_p < x < 0\\ -N_D\left(x^2 - 2xx_n\right) & \text{if } 0 < x < x_n\\ N_D x_n^2 & \text{if } x > x_n\end{cases} \tag{3.15}$$

with ϵ the vacuum permittivity and ϵ_r the relative permittivity of the semiconductor material.

From the definition of the diffusion voltage the width of the space charge region w is calculated to be

$$U_D = \phi(\infty) - \phi(-\infty) = \frac{e}{2\epsilon\epsilon_r} N_D x_n^2 + N_A x_p^2 \tag{3.16}$$

$$\Rightarrow w = \sqrt{\frac{e}{2\epsilon\epsilon_r} U_D \frac{N_A + N_D}{N_A N_D}} \tag{3.17}$$

The depletion zone width decreases with the doping concentration. The ratio for each region is also dependent on the doping concentration in the n-type and p-type region.

3.2.2 pn-junction with applied voltage

One of the applications of the pn-junction is the possibility to apply an external voltage. This results in a shift of the chemical potential μ in the n-doped and p-doped region. Depending on the orientation of the applied voltage one differentiates **forward bias** and **reverse bias**. For the thickness of the space charge region or depletion layer with external voltage U one obtains the formula

$$w = \sqrt{\frac{e}{2\epsilon\epsilon_r}\left(U_D - U\right)\frac{N_A + N_D}{N_A N_D}} \tag{3.18}$$

If the pn-junction is forward biased, the applied positive voltage U decreases the width of the depletion layer. Majority carriers can flow through the diode and recombine in the vicinity of the junction. The pn-junction conducts electrical current.
In reverse bias mode the applied voltage U increases the width of the space charge region. The electric-potential barrier is being increased. No carriers can pass the junction anymore and the diode acts as an insulator. If the entire semiconductor material is depleted, the diode has reached its depletion voltage U_{depl}.

3.3 Silicon particle tracking detectors

Many particle physics experiments like ATLAS and CMS or high energy astrophysics experiments like the Fermi telescope [Bre11] use silicon detectors to track the trajectory of particles. Silicon particle tracking detectors provide high position accuracy, high track separation and short response times.

3.3.1 Working principle of silicon tracking detectors

All silicon tracking detectors work after the same principle. They make use of the pn-junction, described in section 3.2.1, in reverse-bias and the fact that charged particles like electrons, pions or protons lose energy by ionisation when passing through matter.

The silicon sensor itself is a pn-junction operated in reverse bias. When an ionising particle passes through the detector material it will create electron-hole pairs by exiting an electron from the valence band to the conduction band. In silicon 3.6 eV are needed to create an electron-hole pair. This is significantly higher than the actual energy difference between valence band maximum and conduction band minimum or band gap energy (see figure 3.2). The higher energy needed to create an electron-hole pair is due to the additionally needed phonon for the indirect band gap transition. The mean energy loss per distance $-dE/dX$ for a particle is given by the Bethe formula:

$$-\frac{dE}{dx} = \frac{4\pi}{mc^2} \cdot \frac{nz^2}{\beta^2} \cdot \left(\frac{e^2}{4\pi\varepsilon_0}\right)^2 \cdot \left[\ln\left(\frac{2m_e c^2\beta^2}{I\cdot(1-\beta^2)}\right) - \beta^2\right] \tag{3.19}$$

with electron density n, mean excitation potential I, c is the speed of light, ε_0 the vacuum permittivity and e the charge of the muon. In addition the amount of energy lost in the detector varies statistically. In a material of finite thickness the number of collisions between particle and shell electrons of the silicon fluctuates statistically. This leads to the energy deposited in the material following approximately an asymmetric Landau distribution. The ionising particle passing through the sensor material creates electron-hole pairs in an amount directly correlated to the deposited energy. For a minimal ionising particle (MIP) the most probable number of electron-hole pairs produced per 1 µm of silicon sensor material is 76, while the average is 108, see e.g. [Har09].

Operating the pn-junction in reverse bias creates a depletion zone deprived of free charge carriers in the silicon. Subjected to the electric field in the space charge region the electrons and holes produced by an ionising particle cannot recombine with each other. The charges start to drift, electrons towards the anode, holes towards the cathode. A current pulse is produced on the electrodes. The integral of this pulse is equivalent to the generated charge and a direct measure of the deposited energy in the silicon semiconductor material. At the full depletion voltage the space charge region extends over the full width of the bulk material. Using high resistivity silicon allows to apply bias voltages without the risk of breakdown, the sudden increase of current under reverse bias of a semiconductor.

3.3.2 Sensor Concepts

When designing the sensor for a silicon tracking detector the first choice that needs to be made is the combination of substrate and readout electrode implantation. As it was discussed before silicon can be p-doped or n-doped, so four different sensor types exist where the first letter describes the readout electrode implant and the second letter the bulk doping: p^+-in-n, n^+-in-n, n^+-in-p and p^+-in-p. In the scope of this work only the two types with n-doped bulk material are discussed.

p^+-in-n Type Sensors

This sensor type is characterised by a n-doped substrate material that has pixelated p^+-doped electrodes on top. The backside of the sensor is unstructured what gives it a cost advantage

over other sensor designs. The p^+-pixels are electrically insulated from each other by design [Ros06] and due to the missing inter-pixel insulation structure the electrical breakdown voltage of this type is higher than from other types. In an unirradiated p^+-in-n type sensor the depletion zone starts growing from the p^+-implants. After irradiation and consequently type inversion, see section 3.4, of the bulk material from n-type to p-type, the depletion zone starts to grow from the backside of the sensor. In an under depleted state ($U_{\text{applied}} < U_D$) all pixel implants are shorted, the sensor can still be operated though.

In applications with low radiation and the possibility to always operate the sensor fully depleted this sensor type is preferred. It is cheaper to produce and easier to handle than the n^+-in-n type described in the following.

n^+-in-n Type Sensors

This sensor type is produced from a n-doped bulk material that has n^+-doped readout electrodes. The backside also has to be processed and is implanted with a p^+ layer as contact. Additionally the backside needs a guard ring structure to keep all sensor edges at ground potential. The pixels implanted on the top layer are not electrically insulated from each other intrinsically. An additional p-type implant provides the necessary insulation. Two different methods of creating the implant exist: p-spray and p-stop. Before irradiation and type inversion the depletion zone starts growing from the backside. After type inversion this changes and the space charge zone is created close to the pixels. This gives this sensor type an advantage when it is operated in high radiation environments since it is possible to operate it highly under-depleted.

The n^+-in-n is the favoured sensor type for small detectors in experiments expecting high doses of ionising radiation. This sensor type was chosen by the CMS Barrel and the CMS Forward pixel detector groups for the current CMS Pixel detector and the future Phase 1 Upgrade, see section 4.3.

3.3.3 Hybrid Pixel Detectors

The two predominant forms of silicon tracking devices used in high energy particle physics experiments are microstrip detectors and pixel detectors. Microstrip detectors have a fairly low number of channels per square centimetre, usually of the order of 10^2. The readout of each strip can be routed to the edge of the sensor material to connect it to the readout electronics chip by conventional ultrasonic wire bonding. A pixel detector on the other hand has in the order of $10^3 - 10^4$ readout channels per square centimetre. In this case an edge readout is impossible and the connection between sensor and readout chip has to be made vertically.

Detector Layout

As shown in figure 3.6a and 3.6b a hybrid pixel detector consists out for two parts: the highly segmented silicon pixel sensor and the corresponding readout chip. The size of a single pixel and the size of a logical readout cell on the readout chip have to be the same to make the vertical integration of both via bump bonding possible. Typical pixel sizes are in the order of few 100µm or even smaller. Between readout chip and sensor is typically a gap of $10 - 20$µm (see fig. 3.6a). The sensor and readout channel are directly connected (DC coupling). High currents through the sensor by localised discharges or a sensor breakdown can overload the readout chip electronics and even destroy it.

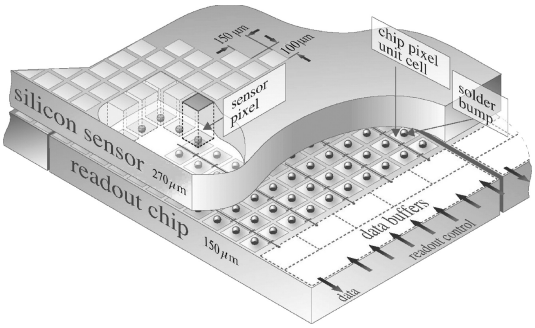

(a) **Layout of a hybrid pixel detector**
A hybrid pixel detector is made from the silicon pixel sensor and the readout chip. Both are vertically integrated by bump bonds to connect every sensor pixel with the corresponding pixel unit cell. The size of the readout cell has to match exactly the size of the sensor pixel to make this possible. Data storage, readout chip control and readout connections are typically made in the readout chip periphery protruding the area of the silicon sensor [CDF+09].

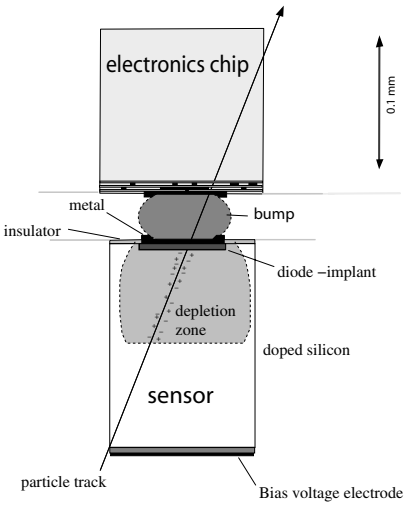

(b) **Vertical view of a single pixel**
The hybrid pixel detector works by collecting the charge deposited in the depletion zone of a silicon sensor operated in reverse bias mode. Every sensor pixel is connected by a bump solder bond to a readout cell in the readout chip. [CDF+09].

Figure 3.6: **Hybrid pixel detectors**

The hybrid pixel detector follows the same readout principle as most charge sensitive devices. The signal collected in the sensor is amplified before being fed to a pulse shaper. Then the signal is converted to a digital value by an ADC and read out. Readout chips with zero-suppression capabilities compare the shaped pulse to an adjustable threshold before digitisation.

Due to the close proximity between readout chip and sensor special emphasis has to be put on proper electrical isolation between both parts. By placing a guard ring structure on the backplane of the sensor the electrical field generated by the bias voltage is contained in the sensor material and potentially destructive sparks between both parts can be avoided. The proximity also bears the risk of introducing noise into the system by the readout signals used. Thus signal standards with a low swing such as LVDS[1] or LCDS[2] are commonly used.

The hybrid pixel detectors used in the CMS Pixel detector and the CMS Pixel Luminosity Telescope are built after this principle. More details on sensor and readout chip design are given in chapter 4.

3.3.4 Charge Sharing

Splitting the charge deposited in a silicon sensor between two or more readout channels is called '*charge sharing*'. This happens often when the particle passes close to the border of two pixels or when the particle passes at an angle through the sensor, traversing the volume of several pixels. Charge sharing is a favourable process in particle physics experiments since it can improve the spatial resolution of silicon based detectors.

One reason why a signal can be spread over several readout channels is the Shockley-Ramo theorem. This theorem says that a current is induced in every readout channel of the detector by the drifting charge carriers in the silicon bulk independent of where the particle passed. For every readout channel i the induced current I_i is

$$I_i = \mathrm{e}\left(\vec{v}\cdot\vec{\nabla}\Phi_{wi}(\vec{x})\right). \tag{3.20}$$

Here e is the elementary charge of the electron, $\vec{v}$ the velocity of the charge carrier. $\Phi_{wi}(\vec{x})$ is the weighting field potential at the position $\vec{x}$ for a specific readout channel i. The weighting field can be obtained by setting the potential created by electrode i to 1 and the potential from all other electrodes to 0. When a charge is moved within the weighting field from $\vec{x}_1$ to $\vec{x}_2$ the induced charge in electrode i is

$$\Delta Q = q\left(\Phi_{wi}(\vec{x}_2) - \Phi_{wi}(\vec{x}_1)\right). \tag{3.21}$$

Free charge carriers in semiconductors spread by diffusion. The diffusion length σ_{diff} depends on the diffusion constant D and the drift time t of the charge carriers.

$$\sigma_{\mathrm{diff}} = \sqrt{2Dt} \tag{3.22}$$

In the silicon sensor this can be approximated to

$$\sigma_{\mathrm{diff}} \approx \sqrt{2\frac{k_{\mathrm{B}}T}{e}\frac{d^2}{U}} \tag{3.23}$$

[1] LVDS: Low Voltage Differential Signaling, a technical standard that specifies a low-power, differential, serial communication protocol commonly used in data transmission.

[2] LCDS: Low Current Differential Signaling, a low-power, differential, serial communication protocol.

with k_B the Boltzmann constant, T the sensor temperature, d the sensor thickness and U the applied voltage [Spi06].

Another way of spreading charge among pixels is by decreasing the incident angle of the particle on the silicon sensor. This can be achieved by tilting the sensor or applying a magnetic field. The magnetic field will change the trajectory of a charged particle due to the Lorentz force

$$\vec{F_L} = q\left(\vec{E} + \vec{v} \times \vec{B}\right). \tag{3.24}$$

Not only does a magnetic field, as it is used in many experiments such as CMS or ATLAS, bend the particle trajectory, the magnetic field also influences the drift direction of charge carriers in the silicon sensor itself. The drift is no longer parallel to the electric field in the silicon, but under an angle, the *Lorentz angle*. In CMS this angle is measured to be up to 25 ° in the Barrel pixel sensors.

Many pixelated silicon detectors are designed in a way to use these effects to their fullest. Pixel sizes and thicknesses are chosen to optimise charge sharing and thus to improve the position resolution of the detector.

3.3.5 Spatial Resolution

The most important factor for the spatial resolution of a detector is the pitch of the readout channels. Although not the entire surface of the sensor is covered by the readout electrodes, no field free volume exists in the silicon sensor. Within the bulk material the electrical field lines run parallel to each other and only bend close to the surface where they end at the doping implants. Also the type of readout and how the hit position is reconstructed has an influence on the position resolution of a detector.

Binary Readout

A pixel is hit when the corresponding readout channel responds to the charge deposited in the sensor. Binary readout describes a readout mode where only information about the fact that a pixel was hit or not hit exists. This leads to limitations of the spatial resolution of a detector due to statistical effects.

Looking at the simplified two-dimensional case where a detector is hit at a random position x between two readout pads with the pitch p, the standard deviation σ of this distribution is given by

$$\sigma^2 = \int_{-p/2}^{p/2} \frac{x^2}{p} dx = \frac{p^2}{12}, \tag{3.25}$$

So the best possible spatial resolution of a detector with binary readout is $\frac{p}{\sqrt{12}}$. Since the pitch cannot be made arbitrarily small this limits the resolution of the detector.

Non-binary Readout

In this readout mode not only the position of a hit pixel but also the measured charge of the hit is available. The free charge carriers created by an ionising particle in the sensor follow the electric field line and create a signal in the pixels surrounding the hit trajectory. If charge is spread on more than one readout channel two additional methods can be applied to increase the spatial resolution of a detector.

Centre-of-Gravity Method

For the centre-of-gravity method it is assumed that the charge is distributed linearly between pixels for a particle passing through the sensor vertically. By linearly weighting the measured charge in a pixel q_i by the relative position of the pixel x_i the particle track position $\bar{x}$ can be calculated

$$\bar{x} = \frac{\sum_i q_i x_i}{\sum_i q_i}. \tag{3.26}$$

This method allows for a simple interpolation between two or more adjacent pixel hits, also called a cluster.

η-Method

In many cases the assumption of a linear charge distribution proves to be too simplistic. The η-method assumes a more complex charge distribution between pixels. This so called η function is measured in an experiment where the exact point of charge creation is known and its distribution between pixels can be measured. In the laboratory this can be realised by inducing charge carriers with a laser for example.

By applying the η function to the charge distribution of a found pixel cluster to reconstruct the particle impact position the spatial resolution of a silicon sensor can be improved.

3.4 Radiation Damage in Semiconductors

Silicon semiconductor sensors in high energy particle physics experiments like CMS are exposed to large amounts of ionising and non-ionising radiation. Particles passing through the sensor do not only create ionisation that can be read out as a signal, but also create defects in the silicon crystal lattice. These defects in the atomic structure of the solid can be described on a microscopic scale, yet also have a large impact on the macroscopic performance of the sensor.

Microscopic Effects

The largest effect radiation has on a silicon sensor is the damage it creates in the bulk material. Through the interaction of the incident particles with the atomic nuclei of the silicon lattice, silicon atoms are displaced. A displaced atom to an interstitial position and the vacant place it left in the lattice structure are called a *Frenkel pair*. Several lattice defects in the same region created by the incident particle, or the primary knock-on atom, are called a defect cluster.

The damage done by radiation strongly depends on its type and energy. Since charged hadrons mainly interact through Coulomb interaction, they primarily create point line defects in the silicon. Neutral hadrons on the other hand interact mainly through nucleus-nucleus scattering, thus transferring more energy and creating mostly cluster defects. For better comparison of the bulk damage created by radiation, particle fluences are scaled to an equivalent fluence Φ_{eq} of 1 MeV neutrons creating the same damage. The unit of this equivalent fluence is $[\Phi_{\mathrm{eq}}] = \mathrm{n_{eq}/cm^2}$.

Apart from the damage occurring in the sensor bulk also the sensor implant silicon-dioxide layers are affected by ionising radiation. Damages to the crystal lattice do not matter in this

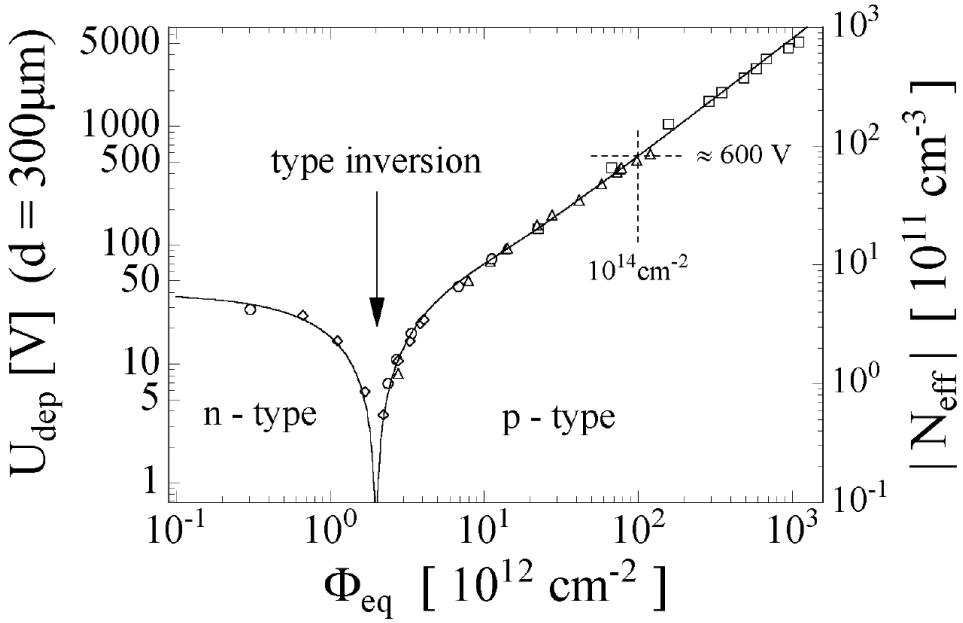

Figure 3.7: **Depletion Voltage of n-type sensor after irradiation**
At first a n-type sensor shows a decrease in depletion voltage after irradiation. This continues until the number of acceptors created in the bulk material outweigh the number of donors. The sensor then effectively behaves like a p-type sensor. With further irradiation the voltage needed to fully deplete the sensor keeps increasing. [Mol99].

case. Only the charge carrier pairs created by radiation in the silicon dioxide are regarded. While most of them recombine, the higher electron mobility creates an accumulation of holes in p-bulk silicon sensors. Slow moving electrons are trapped close to the silicon-silicon-dioxide interface, effectively shortening the n-implanted readout pads. A p-stop or p-spray isolation technique is used to prevent this shortening of readout channels.

Macroscopic Effects

There are three big effects of radiation on a semiconductor sensor that are of macroscopic relevance: an increase in leakage current I_{leak}, a change in the full depletion voltage U_{depl} and a reduction in the charge collection efficiency. All of these effects can be explained by the previously described microscopic damage due to the radiation particles. The leakage current I_{leak} increases due to additionally created defect levels close to the center of the band gap in the semiconductor material. These levels act as generation and recombination centres, making it easier for electrons to be released from the valence band to the conduction band by thermal stimulation. The same is true for the excitation of holes from the conduction band to the valence band. It was found that the increase in current per sensor volume V is linear with the equivalent fluence Φ_{eq} the sensor was irradiated with.

$$\frac{\Delta I_{\text{leak}}}{V} = \alpha \Phi_{\text{eq}} \tag{3.27}$$

The dependence of the leakage current on temperature can lead to a potentially destructive

effect called *thermal runaway*. The increased leakage current in the irradiated sensor at a fixed bias voltage also increases the power the sensor needs to dissipate $P = U \cdot I$. If this power is not dissipated by sensor cooling, the sensor temperature increases further. With higher sensor temperature the leakage current increases again. Without a proper sensor cooling in place this thermal runaway of the sensor leakage current can destroy the sensor if no external current limiters are installed.

Changes in the full depletion voltage are created by defects with energy levels close to the band gap edges. These defects are easily ionised thus contributing to the fixed space charges in the bulk material of the semiconductor sensor. Most of the defects created by radiation in silicon are acceptor-like. In a p-type sensor the bulk material is already doped with acceptors. With irradiation the depletion voltage increases. In a n-type sensor the acceptors created in the bulk material compensate the already existing donors. The reduced effective doping leads to a decrease of the depletion voltage. When the radiation-created acceptors outnumber the donors the bulk starts to behave like a p-type sensor. This effect is called type inversion.

The last macroscopic effect of radiation on a semiconductor sensor is a decreased charge collection efficiency. If the bias voltage applied to the detector is not adjusted accordingly, the increase in the full depletion voltage leads to a smaller depletion region and thus a lower number of charge carriers collected from a passing ionising particle. Additionally, trapping centres created by the radiation can capture charge carriers for longer than the integration time of the readout electronics lasts. This results in an additional loss in signal height.

Chapter 4

The CMS Pixel Readout Chip

The previous chapter covered the general concept of pixelated silicon hybrid detectors used for particle tracking purposes. This chapter will go further into detail by explaining the hybrid pixel detectors used closest to the interaction point in the CMS experiment. The currently installed detector, made from a n-in-n silicon pixel sensor and the PSI46v2 readout chip (ROC), will be described. It will be shown that an increased readout performance will be necessary for further operation of the CMS experiment in the high instantaneous luminosity environment provided by the LHC. The evolutionary upgrade of the current readout chip, the PSI46dig, will be introduced and its new and improved readout mechanism presented. Since the understanding of both readout chips is integral for the work presented in later chapters of this thesis, the analogue PSI46v2 being used in the PLT (see chapter 5) and the digital PSI46dig ROC being used for the upgraded Pixel Detector (see chapter 2.4 and following), the readout mechanism is explained in greater detail.

4.1 The PSI46v2 Readout Chip (ROC)

The PSI46 readout chip (ROC) was designed for the CMS Pixel Detector [K+06]. It has function in a magnetic field of 4 T and at particle rates as high as $40\,\mathrm{MHz\,cm^{-1}}$ without significant data loss or dead time. The ROC records the hit position and amount of deposited charge in the silicon sensor with a time resolution of 25 ns, which is the originally intended time between two bunch crossings of the LHC and will also be the nominal value during Run II operations. The recorded information can be stored for a programmable amount of time of up to 6.375 µs. After this time has expired, saved hits that are not validated by an external trigger signal are discarded, while validated hits are marked for readout and transmitted to the detector back-end upon the arrival of an external readout token. The analogue encoded readout of hit data is shown in figure 5.1.

A second possibility to gain information about the pixel hits on the ROC is the *Fast-OR* signal described in detail in section 5.4.4. This signal provides an estimate of the number of particles crossing the detector for every bunch crossing. The only use case for the *Fast-Or* mechanism is the Pixel Luminosity Detector (PLT) described in chapter 5.

The PSI46v2 was produced using a radiation hard fabrication process with 250 nm feature size [K+06]. It houses a total of 1.3 million transistors and can be separated into three functional blocks: control and supply, an array of pixel unit cells and the double column periphery.

Control and Supply

This block is responsible for the input and output signals and the supply voltages. The ROC requires two separate external voltages to be operational: 1.5 V for the analogue part and 2.5 V for the digital part. These voltages are controlled via programmable

regulators and need to be set on every ROC individually. The chip's parameters are programmed through an I^2C [1] interface, running at 40 MHz. All other input and output signals, such as trigger or reset commands, are transmitted using a single LVDS signal line. Two output signals are available, both transmitted over LVDS. The first signal carries the pixel hit information. The pixel address is encoded in six discrete levels, while the signal charge is transmitted as an analogue pulse height. The second signal is generally called the 'Fast-OR'. It is a pixel cluster multiplicity counter running at the ROC internal clock of 40 MHz. The height of the produced signal is proportional to the number of non adjacent double column clusters found on the ROC.

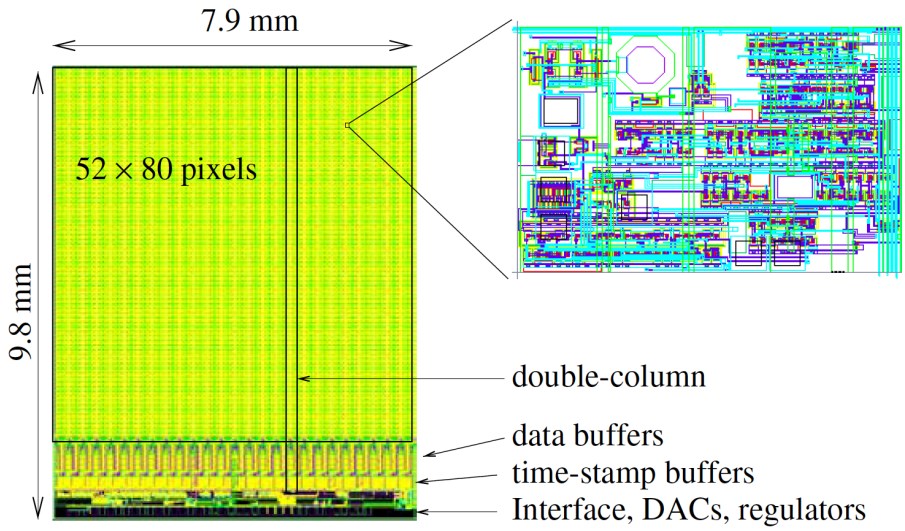

Figure 4.1: **Floor plan of PSI46v2 readout chip[Erd10]**
The active area of the PSI46v2 readout chip is the matrix of 52×80 pixels organised in a double-column readout structure. Data buffers, time stamp buffers and the control and supply circuits of the ROC are moved to the side of the chip. Also shown is a single pixel unit cell from the left half of a double-column. The pixels of the right column are mirrored. All pixels of a double-column share a common vertical bus line.

Pixel Unit Cell

The second building block of the PSI46v2 is an array of 52×80 pixel unit cells (PUCs). They are arranged in 26 double columns of 160 pixels each. The schematics of a single cell are given in figure 4.2. The analogue part of the PUC contains the two-stage preamplifier and shaper circuit, a voltage comparator and a sample and hold circuit. Charges collected from the sensor or injected via an internal calibration charge mechanism pass the preamplifier and shaper stage before passing a comparator that is used to suppress signals smaller than a programmed threshold (zero-suppression). This pixel threshold can be set by changing a global threshold voltage. Variations in the manufactured transistors can be compensated by a 4-bit digital-to-analogue converter (DAC) to trim the threshold of each pixel individually.

Double Column Periphery

[1] I^2C: short for **I**nter-**I**ntegrated **C**ircuit, a multi-slave, single-ended, serial bus, used to communicate with integrated circuits such as ASICS or micro-controllers.

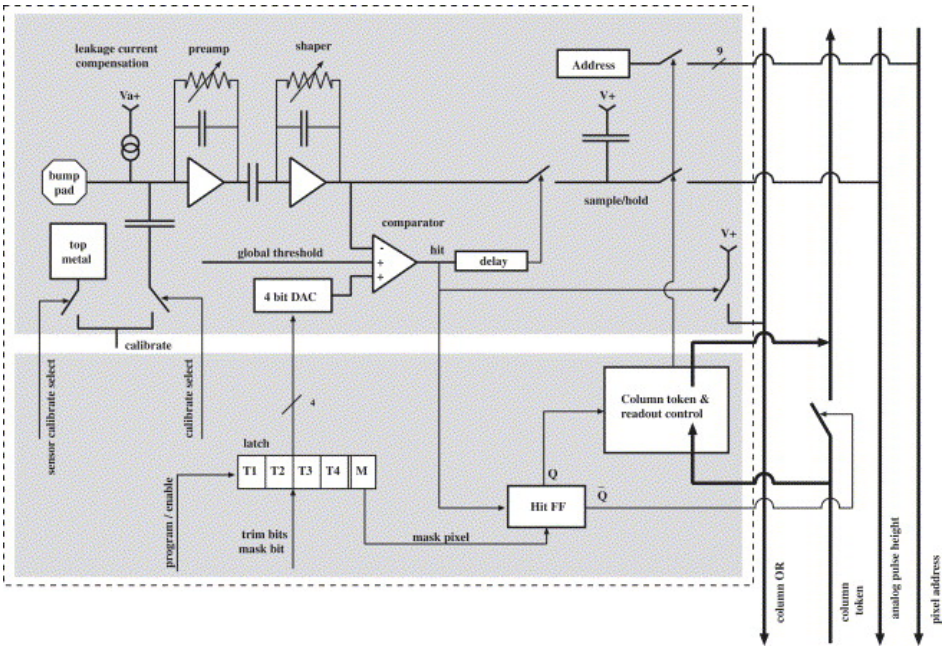

Figure 4.2: **Schematics of the pixel unit cell of the PSI46v2 readout chip[K$^+$06]**
The pixel unit cell is separated into two parts: the digital (lower) and the analogue (upper) part. The amplifier and comparator circuit to detect signals in the silicon sensor connected to the ROC are housed in the analogue part, while the logic to communicate detected hits to the double-column periphery is in the digital part.

The double column periphery schematics are pictured in figure 4.3. The double column periphery is responsible for the transfer of hit data from the PUCs to the data buffer and trigger validation of stored data. It contains a buffer for up to 12 time stamps and a buffer for 32 pixel hits for every double column.

4.1.1 Double Column Readout

To fully understand the hit detection performance of the PSI46v2 readout chip the mechanism of the double-column readout is essential. In this paragraph the readout of the full pixel data and the potential readout inefficiencies are described.

When a PUC detects a charge, either deposited in the sensor material by an ionising particle or injected through the ROC internal charge injection pulse, higher than the previously programmed threshold, the shaper output signal is stored in a sample-and-hold circuit. At the same time the PUC informs the double column periphery via a fast column-OR signal about the hit. The pixel now waits for a readout token from the periphery. In the periphery the arrival of the column-OR signal latches the creation of a time stamp. Simultaneously the column drain control logic, see figure 4.3, will associate all pixels hit in this bunch crossing with the column OR signal received. Hits in later bunch crossings will be linked to another column drain. At the same time only one active column drain and two pending column drains are allowed. If a double column sees three hits in three consecutive bunch crossings, the third hit will be assigned to the same pending double column as the first hit. This is a source of inefficiency because the third hit is marked with an incorrect time stamp. An activated

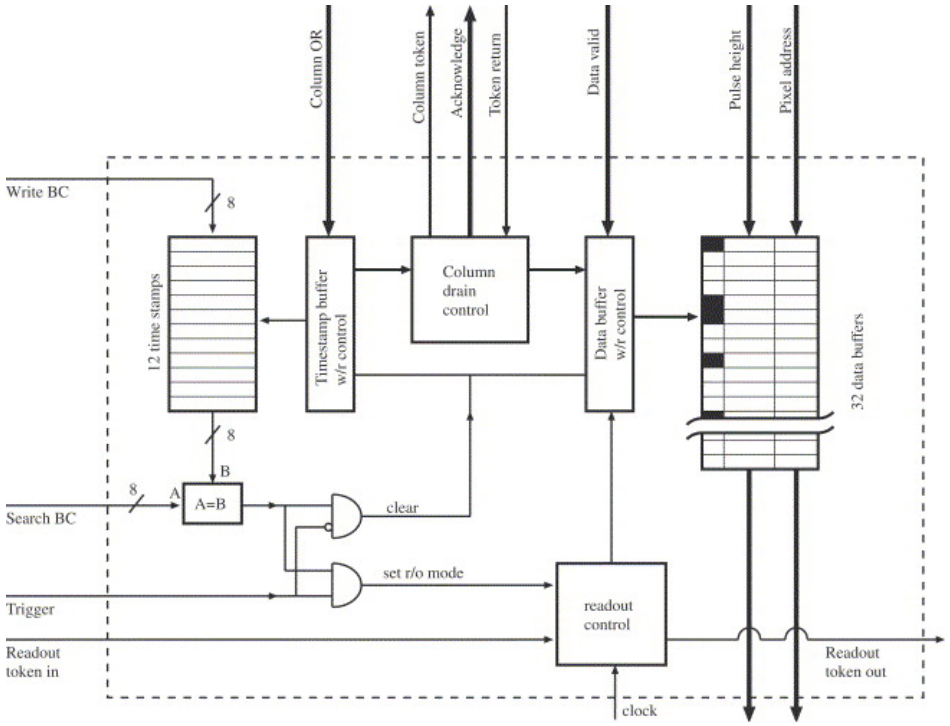

Figure 4.3: **Schematics of the double column periphery of the PSI46v2 readout chip[K$^+$06]**
The 160 pixels of a double-column share the same buffer and readout control logic in the periphery. Every double-column has a 32 cell wide data buffer and a time stamp buffer of 12 cells. After a pixel has been detected the column drain control logic transfers the hit data from the PUC to the data buffer. When a hit is validated by an external trigger signal the double-column waits for a readout token to pass before accepting new pixel hits.

column drain creates a token in the double column that passes by pixels without hits, but drains the hit information of hit pixels into the data buffer of its double column. The transfer of the hit information takes two bunch crossings per hit pixel. Between acknowledging a hit in the PUC and the arrival of the token, the pixel is unresponsive to additional hits, creating an additional source of inefficiency.
In the double column periphery the bunch crossing counter SBC is constantly compared to the first time stamp stored. SBC is delayed with respect to the written time stamps by the trigger latency. If a match is found, the double column stops data taking and waits for an external readout token. After this token has passed and all data is transferred, the double column resets itself, potentially losing valid data already stored in the data buffer and creating another source of random data loss in the ROC. Other sources of dynamic inefficiencies in the readout chip are created by the overflow mechanisms of time stamp and data buffer. When the data buffer of 32 cells overflows, the entire buffer is erase. All stored hit information is lost. When the time stamp buffer overflows, the buffer is not erased. Instead no new time stamps are created. Every hit arriving while the timestamp buffer is at its maximal capacity will be assigned the same time stamp, the one added last to the buffer. Hits with incorrect time stamps also contribute to the random data loss in the readout chip.

4.1.2 ROC Readout Encoding

The pixel hit data validated by an external trigger is read out when a readout token, sent by the Token Bit Manager (TBM, see section 5.2.1), arrives at the ROC. Typically ROCs are daisy chained and used in groups. The TBM chip is responsible to coordinate the ROCs of such a readout group. All control and trigger signals arrive separately on each ROC, but they share a common data output line and a line for the readout token. In the Barrel and Forward Pixel Detector of CMS a single TBM is used to control a group of up to 24 ROCs [K+06], while in the PLT a TBM controls only the three ROCs of a telescope.

To be able to separate the data from different ROCs of the same readout group on a single data line, the ROC adds a header signal pattern to the data before transmitting its payload. The ROC header is a unique three clock cycles long signal pattern. It starts with a large negative signal height, the Ultrablack, followed by a zero and a pulse height inversely proportional to the last DAC set. The pixel address is encoded in two levels describing the double column and three levels encoding the hit row in the respective double column. The pixel address encoded in discrete pulse heights (see figure 5.7) is followed by the analogue pulse height for the measured charge. Transmitting one pixel hit thus takes six clock cycles.

4.2 Evolution from analogue to digital ROC

Since the start of the LHC in 2009 the instantaneous luminosity delivered to the experiments has been increased continuously, surpassing the expectations made when CMS or ATLAS were conceived. The original readout chip PSI46v2 was expected to see particle rates of up to $40\,\mathrm{MHz\,cm^{-2}}$ at a design luminosity of $10^{34}\,\mathrm{cm^{-2}\,s^{-1}}$ with a random data loss of 4% in layer one of the pixel detector. With the higher than expected average number of collisions per bunch crossing and all layers of the new pixel detector moving closer towards the interaction point (see chapter 2.4) the predicted rates would exceed the capabilities of the current readout chip to efficiently record data. The new PSI46digV2.1respin was developed to address these challenges.

4.2.1 The CMS PSI46digV2.1respin

The new digital version of the CMS Pixel readout chip is based on the PSI46v2 chip. The architecture and processing technology were not changed, but improvements were made to the readout scheme and data storage capabilities.

The PSI46dig[2] readout chip was developed and produced with a radiation hard 250 nm design. Compared to its predecessor, the PSI46v2, the number of metal layers in the readout chip is increased by one, to six layers in total. This new layer will make the readout chip less prone to cross talk between the comparators of the analogue part of the pixel unit cell and the digital voltage line, by decoupling the two. A new routing of the calibration charge signal is supposed to reduce cross talk between pixels when using internal calibration charges.
Several of the DACs from the old ROC were removed and replaced by fixed voltage levels. The remaining DACs were equipped with a fixed 'power-on' setting, so that after supplying the new ROC with its supply voltages it would be in a defined, low power state. A full list of all DACs for the old and the new readout chip can be found in table 4.1.

The most important changes made to improve the performance of the new readout chip are in the hit storage and the readout transmission. The pixel unit cell of the readout chip and

[2]In the following text PSI46dig will refer to the PSI46digV2.1respin

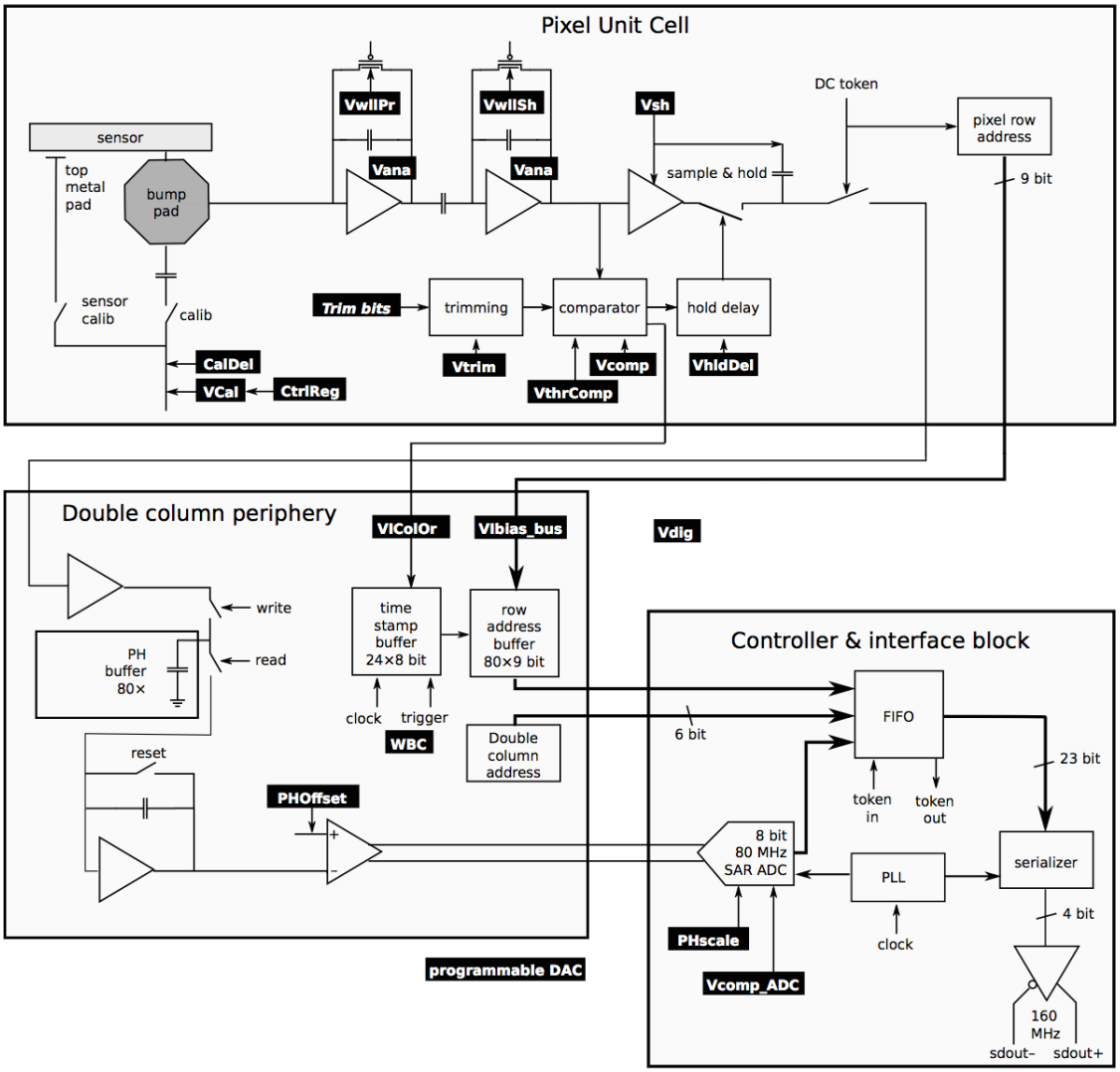

Figure 4.4: **ROC DAC schematic**

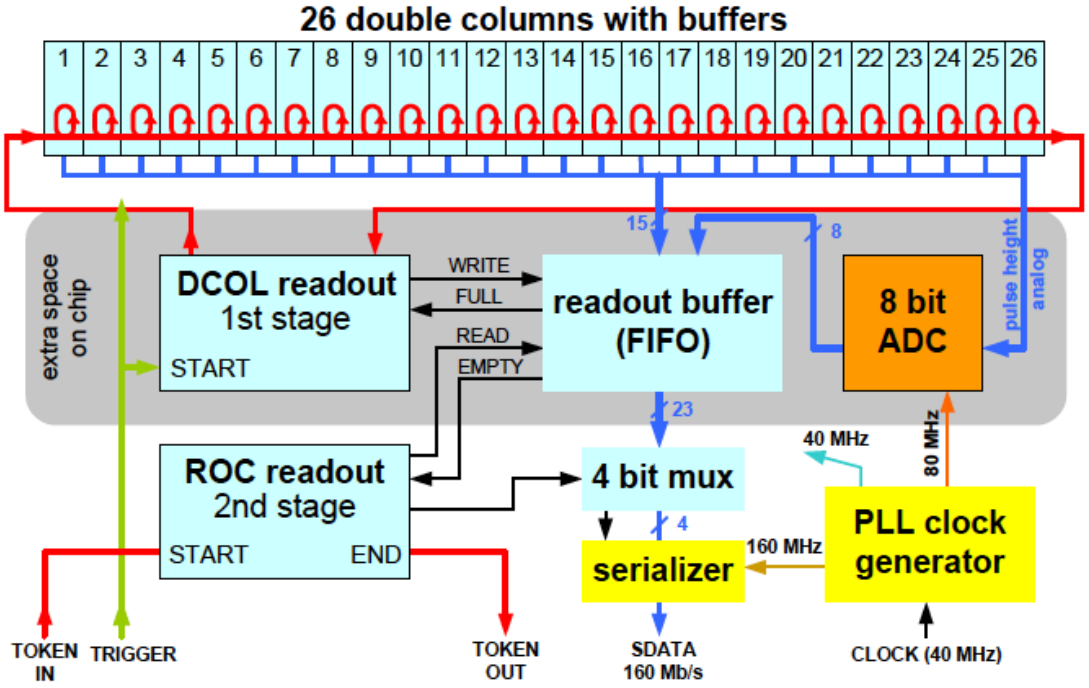

Figure 4.5: **PSI46dig readout logic**

the double column readout structure have remained unchanged between the PSI46v2 and the PSI46dig. In the chip's periphery the buffer sizes of time stamp and data buffer have been increased, making it possible for the ROC to store more data. The time stamp buffer size was doubled from 12 to 24 cells and the data buffer increased from 32 to 80 cells.

By introducing a second readout stage, see figure 4.5 in the chip the dead time from waiting for a readout token was greatly reduced. In the PSI46dig, after the readout chip received a trigger signal validating stored pixel hits in the periphery of a double column, an internal token signal is sent to collect the hit information and store it in a readout buffer FIFO [3]. In the 64 cells deep readout FIFO the pixel hit addresses and the analogue pulse height, converted to a digital value by an eight bit ADC, are stored until an external readout token arrives at the chip. The readout token will trigger the serialised 160 Mbit s^{-1} binary data stream from the readout chip. To be able to handle the different clock domains, 40 MHz for the pixel unit cells and the pixel periphery, 80 MHz for the eight bit ADC and 160 MHz for the data stream output, the readout chip is equipped with a 160 MHz phase locked loop (PLL) that is locked to the external 40 MHz LHC clock. To fit the additional buffer cells in the double column periphery and the readout FIFO and the PLL onto the PSI46dig chip, the size of the ROC had to be increased by 4 mm. The active area with the array of pixel unit cells was not affected by this changes. The *Fast-Or* signal, described in section 5.4.4, has been removed from the new PSI46dig readout chip. With this also the two DACs *Vnpix* and *VsumCol* became obsolete and were removed from the ROC.

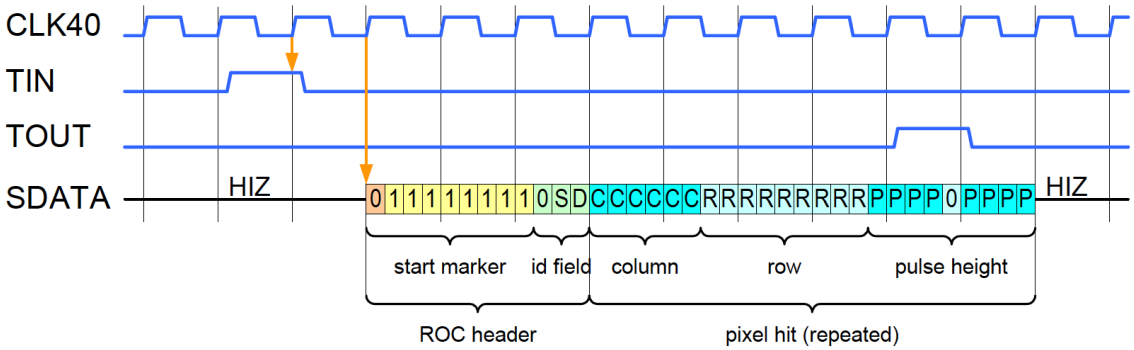

Figure 4.6: **PSI46dig data format**
The plot demonstrates the token mechanism of the readout chain for the PSI46dig chip. The `CLK40` trace represents the 40 MHz clock the ROC is running on. `TIN` and `TOUT` are the token-in and token-out lines. The token-in line is sampled on the rising edge of the clock, after the ROC sees the signal it takes one clock cycle until it starts transmitting its data. Even before the ROC finishes transmitting data it passes the readout token to the next chip.
The digital data format is also presented in the plot. The digital data is transmitted on a 160 MHz clock on the `SDATA` line. The ROC readout starts with a header followed by the data payload of column, row and pulse height information for each pixel hit in the triggered event.

4.2.2 The Digital Readout Format

As already stated in the previous section, the data output of the PSI46dig chip is a serial 160 MHz binary data stream. Instead of the analogue level encoding for pixel address and pulse height of the hit information, the data is encoded in a binary format of zeros and ones. The information is encoded in the data format shown in figure 4.6. Every hit data readout of the ROC is preceded by a header. The header contains a unique pattern of eight consecutive ones with a leading and trailing zero. This specific pattern can never appear in the data payload. The ROC header also has two status bits that are used to read back settings and voltage measurements from the readout chip. The S bit marks the start of a read back, while the D bit transmits the data over 16 consecutive ROC readouts. The header is followed by the pixel data payload. One pixel hit is transmitted in six bits for the double column value, nine bits for the row value and eight bits from the digitised analogue readout. The pulse height value is separated by an extra zero bit to prevent the appearance of eight consecutive ones in the pixel data conflicting with the unique pattern of the ROC header.

4.2.3 Data encoding

The pixel address information coming from the PSI46dig chip is encoded in Gray code [Gra53]. Gray code is a binary numeral system where two successive values only differ by one bit. The reflected binary code is commonly used to facilitate error correction in digital data transmissions.

Like the PSI46v2, the pixels on the PSI46dig are grouped in 26 double columns. The six

[3] **FIFO** acronym for: First In, First Out

bits transmitting the column information can be separated into the three Most Significant Bits C_{MSB} and the three Least Significant Bits C_{LSB}. The double column value between 0 and 25 can then be calculated by the formula

$$\text{double column} = C_{\mathrm{MSB}} \cdot 6 + C_{\mathrm{LSB}}. \tag{4.1}$$

To generate the row information of a pixel hit, the nine bits need to be split into three groups of three bits each: the three Most Significant Bits R_{MSB}, the three Least Significant Bits R_{LSB} and the three bits in between R_{mid}. The pixel id in the double column between 0 and 159 is calculated by

$$\text{pixel id} = R_{\mathrm{MSB}} \cdot 36 + R_{\mathrm{mid}} \cdot 6 + R_{\mathrm{LSB}}. \tag{4.2}$$

Both values, double column and pixel id, are needed to generate the actual pixel address within the array of 52 columns by 80 rows of a readout chip. The pixel id describes the row of the pixel unit cell that was hit, but also to what side of a double column the pixel belongs too. All pixels with an even pixel id belong to the left column and all pixels with an odd pixel id belong to the right column of the double column structure. The row information can be retrieved from the pixel id only. The numbering convention starts with row zero being the closest to the double column periphery. Counting in steps of two the 80 pixels in the left column are numbered from 0 to 158. The pixels in the right column are equally numbered from 1 to 159. So the pixel address can be calculated by the two equations

$$\text{column} = \text{double column} \cdot 2 + \text{pixel id} \,(\mathrm{mod}\ 2) \tag{4.3}$$

$$\text{row} = \lfloor \text{pixel id}/2 \rfloor, \tag{4.4}$$

where mod is the modulo operator that finds the reminder in the devision of two integer numbers and $\lfloor x \rfloor$ is the floor function that maps any real number to its next smaller integer value. The Gray code conversion tables can be found in [Gab05].

4.3 The Silicon Sensor

CMS uses pixelated silicon sensors produced for Barrel Pixel detector with a pixel pitch of 100 µm in the direction of the rows and 150 µm in the column direction. The same sensors were used for the PLT and the High Rate Beam Test described later in the thesis at hand. The sensors are made from high resistivity n-doped silicon as bulk material that is implanted with a high dose of donors (n-in-n type). To create the pn-junction which the detector principle is based on, the back side of the detector is p-doped. To insulate the pixels from each other a p-spray implantation was applied to the entire wafer. A guard ring structure on the backside of the sensors prevents high-voltage discharges between the sensor edges and the readout chip the sensor is bump bonded to.

The n-in-n concept has the advantage that even after high doses of radiation and space charge sign inversion the number of collected charge carriers is still high even when operated under-depleted. This is due to the fact that the region of high electric field strength moves to the readout side. This kind of sensor has been studied extensively. After a fluence of $1.2 \times 10^{15}\, n_{eq}/\mathrm{cm}^2$ a hit detection efficiency above 95% was observed for a detection threshold of 3000 electrons [R$^+$04].

A photograph of the CMS Pixel sensor can be seen in figure 4.7. It shows the side of the sensor that will be bump bonded to the readout chip. Each pixel is connected to the bias grid through a small punch-through resistor.

Table 4.1: **List of DAC for PSI46v2 and PSI46dig**

	PSI46v2		PSI46dig	
DAC address	DAC name	Description	DAC name	Description
1	Vdd	Regulator for digital voltage	Vdd	Regulator for digital voltage
2	Vana	Regulator for digital voltage	Vana	Regulator for digital voltage
3	Vsf	Voltage for sample and hold circuit	Vsf	Voltage for sample and hold circuit
4	Vcomp	Threshold comparator voltage	Vcomp	Threshold comparator voltage
5	Vleak	Sensor leakage compensation	DAC removed	
6	VrgPr	Preamplifier feedback	DAC removed	
7	VwllPr	Preamplifier feedback	FBPre	Preamplifier feedback
8	VrgSh	Shaper feedback	DAC removed	
9	VwllSh	Shaper feedback	FBSh	Preamplifier feedback
10	VHldDel	Hold delay	VHldDel	Hold delay
11	Vtrim	Global trim voltage	Vtrim	Global trim voltage
12	VcThr	Global threshold voltage	VcThr	Global threshold voltage
13	VIbias_bus	DCol bus driver voltage	VIbias_bus	DCol bus driver voltage
14	VIbias_sf	Source follower	DAC removed	
15	VOffsetOp	DCol readout	DAC removed	
16	VbiasOp	DCol readout	DAC removed	
17	VOffsetRO	DCol readout offset	PHOffset	Voltage amplifier offset
18	VIon	DCol readout	DAC removed	
19	VIbias_PH	Output pulse height	ADCpower	ADC comparator voltage
20	VIbias_DAC	Pixel address range	PHscale	ADC reference
21	VIbias_roc	Adjust single ended output level	DAC removed	
22	VIColOr	ColOR current limiter	VIColOr	ColOR current limiter
23	Vnpix	FastOR pixel threshold	DAC removed	
24	VsumCol	FastOR trigger threshold	DAC removed	
25	Vcal	Calibrate pulse height	Vcal	Calibrate pulse height
26	CalDel	Calibration delay	CalDel	Calibration delay
253	Chip Control Register		Chip Control Register	
254	WBC	Trigger latency	WBC	Trigger latency

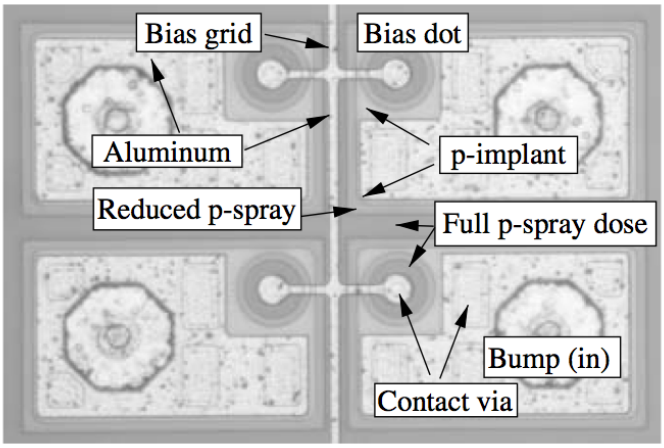

Figure 4.7: **Four pixel cells of the CMS Barrel Pixel sensor**
The CMS pixel sensor is a n-in-n type sensor. A pixel has a size of 150 µm by 100 µm and an active thickness of 285 µm.

Chapter 5

The Pixel Luminosity Telescope

The Pixel Luminosity Telescope (PLT) is a new subsystem of the CMS detector built for the second data taking period of the LHC, commonly referred to as *Run II*. Eight three-layer particle tracking telescopes based on silicon pixel detectors have been placed around the beam pipe on each end of CMS viewing the interaction point at a small angle. A bunch-by-bunch luminosity measurement will be provided by counting threefold coincidences in the pixel planes of the telescopes. Track reconstruction will enable the detector to distinguish between beam background and collision products coming from the interaction point. Additionally an alignment of the detector planes can be obtained from the reconstructed particle trajectories. Continuous monitoring of pixel efficiencies will be needed to correct for possible performance losses in the detector. The PLT, as the only independent single-purpose luminometer in CMS, is essential to enhancing the robustness of the measurement of the delivered luminosity by the LHC and to reduce its systematic uncertainties. With this the CMS experiment will be able to determine production cross sections, and hence couplings, with higher precision.
This chapter will first provide a general overview over the luminosity measurements performed for the CMS experiment, the method applied by the PLT and other luminometers, called 'zero counting', will be explained before going into details of the PLT detector itself. The design of the PLT and the individual parts it is built from are showcased, then the procedure to bring the detector into a working state will be described before the first measurements of the PLT inside CMS will be shown and discussed.

5.1 Luminosity measurement at CMS

The luminosity provided by the LHC is one of the key parameters to the measurements performed by the CMS experiment. The luminosity and respectively the integrated luminosity are essential to determine the production cross section of rare events observes by CMS. This relation was already shown in equation 2.1 for the instantaneous luminosity and in equation 2.2 for the integrated luminosity respectively. From the integrated luminosity provided to CMS, and thus from the total number of proton-proton collisions created by the LHC, the radiation damage created in the detector can be estimated. This is important to predict the live span and future performance of the detector.

Within the CMS experiment four detectors exist that are used to measure the luminosity: the PLT, discussed in this chapter, the Hadron Forward Calorimeter (HF), the Beam Conditions Monitors (BCM) and the CMS Pixel detector.

Three of the four luminometers of CMS are operational at any time during operations. The PLT, HF and the BCM detectors are operational independent of the beam status of the LHC. They are used for the 'online' luminosity measurement. The three online luminometers continuously measure the luminosity measured by the LHC and provide these numbers in real-time to a live display. The online luminosity provides valuable insights about the losses

in the beam and delivers quick feedback for beam optimisations.

All online luminometers apply method called 'zero counting' to measure luminosity, which will be described in section 5.1.1.

The Pixel detector is used as the fourth luminometer in CMS. Since the pixel detector is only operational after the LHC has declared the two circulating beams to be stable and the data can not be processed and analysed during runtime, this luminosity measurement is called 'offline luminosity'. For the luminosity measurement the number of clusters produced in the second and third layer of the Pixel detector is used. Only minimum bias events, events for which the only trigger condition is that both colliding bunches need to contain protons, are used for the measurement. The first layer of the Pixel detector is excluded from the measurement because dynamic inefficiencies and random data loss, see chapter 4, influence the cluster counting.

During the first running period of the LHC, the Hadron Forward Calorimeter and the Pixel detector were the two luminometers available to CMS. At the end of this running period the absolute luminosity was re-measured in a Van der Meer scan, see below, performed during LHC fill 3316. As described in [Col13] the uncertainties on the calibration and the integrated luminosity was estimated to be 2.5%.

5.1.1 Zero counting method and absolute luminosity calibration

All three online luminometers rely on the same measurement method for the luminosity. Contrary to the offline measurement in the CMS Pixel detector, the online luminometers, HF, PLT and BCM, calculate the delivered luminosity from the number of empty channels in each 25 ns bunch crossing that do not measure traversing particles coming from the interaction point. This method is called 'zero counting' and will be explained in this section.

The luminosity $\mathcal{L}$ in a collider experiment is the proportionality factor between the number of collision events per second $\frac{dN_p}{dt}$ and the cross section σ_p of the process under study:

$$\frac{dN_p}{dt} = \mathcal{L} \cdot \sigma_p. \tag{5.1}$$

The unit of luminosity is $\mathrm{cm}^{-2}\mathrm{s}^{-1}$ [HM06].

For a collider with two equal beams with a Gaussian spatial distribution of particles in all dimensions one can calculate the luminosity from beam parameters to be

$$\mathcal{L} = \frac{N_1 N_2 f n_b}{4\pi\sigma_x\sigma_y}, \tag{5.2}$$

with N_1 and N_2 being the number of particles per bunch in beam 1 and beam 2, f the revolution frequency and n_b the number of bunches. σ_x and σ_y describe the geometrical width of both beams in x and y direction.

As the detectors are sensitive to the products of inelastic scattering in proton-proton collisions, one can also define the luminosity to be

$$\mathcal{L} = \frac{R_{\mathrm{inel}}}{\sigma_{\mathrm{inel}}}. \tag{5.3}$$

By rewriting the rate of inelastic collisions R_{inel} one gets:

$$\mathcal{L} = \frac{\mu \cdot n_\mathrm{b} \cdot f_\mathrm{orbit}}{\sigma_\mathrm{inel}}. \tag{5.4}$$

Here μ is the average number of inelastic collisions, n_b the number of bunches per orbit, f_orbit the orbit frequency and σ_inel the inelastic proton-proton cross-section.

So to determine the relative luminosity the average number of inelastic collisions μ needs to be measured. This is a random variable following a Poisson distribution with n being the number of observed interactions [Bel13].

$$p\left(n;\mu\right) = \frac{\mu^n}{n!} e^{-\mu} \tag{5.5}$$

By counting the number of interactions without observed events in the luminometer ($n = 0$) and calculating the probability $p(0)$ for this to happen, μ can be determined by

$$\Rightarrow \mu = -\log\left[p(0)\right], \tag{5.6}$$

thus making the observed luminosity proportional to the probability of finding zero interactions in a bunch crossing

$$\mathcal{L} \sim -\log\left[p(0)\right]. \tag{5.7}$$

To find the absolute value of the luminosity measurement a Van der Meer scan (VdM scan) [vdM68] by the LHC is needed. During the VdM scan the two beams are displaced with respect to each other to measure the beam size. The measured luminosity depends on the displacement d and for two equal beams is given by [HM06]

$$\mathcal{L}(d) = \mathcal{L}_0 e^{\frac{-d^2}{4\sigma^2}}. \tag{5.8}$$

Such a VdM scan is performed several times per year for all experiments of the LHC to calibrate luminosity measurement devices.

What one ultimately wants to find is the relation between the observed rate R_vis and the delivered luminosity $\mathcal{L}$

$$\mathcal{L} = k \cdot R_\mathrm{vis} = \frac{R_\mathrm{vis}}{\sigma_\mathrm{vis}} \tag{5.9}$$

During the displacement of the VdM scan the measured rate in the detector will reach a maximum value R_peak that is connected to the peak instantaneous luminosity $\mathcal{L}_0$ by

$$\mathcal{L}_0 = k \cdot R_\mathrm{peak}. \tag{5.10}$$

By using the geometric parametrisation of the luminosity in a collider from equation 5.2 one arrives at

$$\sigma_\mathrm{vis} = \frac{R_\mathrm{peak} 4\pi\sigma_x\sigma_y}{N_1 N_2 f n_b} \tag{5.11}$$

The beam intensities of the two beams N_1 and N_2 are known values measured by Fast Beam Current Transformers (FBCT) for every 25 ns bunch [CMS10]. The revolution frequency of the LHC accelerator is 11.22 kHz and the number of filled bunches n_b is also known. To measure the standard deviation of the Gaussian shaped beam, σ_x and σ_y, the VdM scan is needed. The normalised measured rate, dependent on the beam displacement, is fitted with

a Gaussian. From the fit the standard deviation can be extracted according to equation 5.8. The peak rate R_{peak} is achieved when the colliding beams are not displaced.

With all these quantities available it is possible to calculate σ_{vis} as the proprotionality constant between the observed rate in the detector, determined by zero counting, and the absolute value of the delivered instantaneous luminosity.

5.2 The Pixel Luminosity Telescope Detector

The PLT is a new subdetector in the CMS experiment whose sole purpose it is to measure the luminosity delivered by the LHC. It does so by tracking the collision products created in the Interaction Point through 16 small angle beam telescopes made from three planes of pixelated silicon sensors. The text will describe the PLT setup, the calibration procedure to bring the PLT in a good working condition and will show show the first measurements from particle collisions.

The PLT is built using the same hybrid sensor and readout technology that is used in the current pixel detector installed in CMS[K$^+$06]. The PLT detector itself is divided into quarters where each quarter, or 'cassette', is a separate mechanical and electrical structure that houses four small angle telescopes, uniformly distributed in azimuthal angle Φ around the beam pipe. Two cassettes are placed on each end of CMS at a distance of 1.75 m from the interaction point. This exact distance ensures maximum separation between collision products and the incoming beam. A telescope is 7.5 cm long and 5 cm away from the beam line, which corresponds to $|\eta| \approx 4$ [Dab14]. The angle under which the telescopes view the IP is $\alpha = 1.55°$. Each telescope consists of three hybrid detectors, see chapter 4, equipped with a pixelated silicon sensor covering a surface of 62.4 μm^2. The silicon pixel sensor is an array of 4160 pixels, arranged in 80 rows and 52 columns. The pixels have a pitch of 100 µm in the row direction and a pitch of 150 µm in direction of the columns. The sensors used for the production of the PLT are left over pieces from the R&D and production qualification phase of the construction of the CMS pixel detector and have been introduced in section 4.3. The sensors have a depletion depth of 285 µm[Ves13]. Every sensor is bump bonded to a single PSI46v2 CMS pixel readout chip[A$^+$08].

After a brief description of the building blocks which the Pixel Luminosity Telescope is made of, the following sections will highlight the separate elements in greater detail while following the readout chain of the PLT from front-end to back-end.

5.2.1 Single Telescope

As already mentioned a single PLT telescope is made from three planes of CMS analogue pixel detectors. Each telescope plane consists of a PSI46v2 readout chip, described in section 4.1, and a standard n-in-n type CMS silicon pixel sensor, see section 4.3. The pixel detectors are glued to a polyimide flexible circuit board (Kapton flex) called 'Hybrid Board'. This board is a purely passive element. It is used to place all the wire bonds that are needed for the low voltage supplies and control and readout signals for the ROC and for the connection of the high voltage line to the silicon sensor. The small flex cable tail of the Hybrid Board goes to a connector on the 'High Density Interconnect Board', or HDI. The HDI houses an important component to form a functioning telescope unit, the Token Bit Manager (TBM)[Bar05].

The TBM is responsible for coordination of the readout of all ROCs in the telescope. All external trigger signals pass through the TBM and it makes sure that for each trigger only a single readout token is sent to the daisy chained ROCs to collect the data of an event.

The TBM can withhold triggers to accommodate for readouts that are unusually long or during times when many triggers are sent within a short period of time. When the TBM has initiated the readout of an event, it will add a header and a trailer to the data stream as shown in figure 5.1. The header contains an event number and the trailer transmits status and error information.

Additionally the TBM is also responsible for the distribution of clock and control signals. While the clock is sent in parallel to all ROCs in a telescope, the control signals for setting chip parameters go through a central distribution logic, called a HUB, with 4 ports, three of which are used in the PLT. This makes it possible to address specific ROCs when sending control signals to set ROC registers.

The four single telescopes of a PLT quarter are connected through the 'Portcard' to the Opto-Hybrid Motherboard. The Portcard serves as a fanout between three flat Kapton flex cables from Opto-Hybrid Motherboard to the four telescopes.

5.2.2 The Analogue and Digital Optohybrid

All signals from and to the PLT telescopes are electrical but the signal drivers are not strong enough to transmit the data further than $\sim 1\,\mathrm{m}$, posing a problem at a distance of more than 50 m between detector and readout electronics. This problem is solved by converting the electrical signals to optical signals that are transmitted via optical fibre to the Front End Drivers (FEDs). A custom-made level translator, the Analogue Optical Hybrid (AOH), receives the data signals, pixel data and Fast-OR signals, and shifts and amplifies them so that they are correctly received by the optical drivers in the FED. The FED then digitises and decodes the data.

For control signals coming from the Front End Controller (FEC) a similar device is used. The Digital Optical Hybrid (DOH) receives optical signals and translates them to electrical signals for the TBM and the ROCs.

All these hybrids are placed together on a single board, the Opto-Hybrid Motherboard. A simple schematic of the readout structure can be found in figure 5.2.

5.3 Mechanics and Installation

The PLT, just like the two Beam Condition Monitors BCM1L and BCM1F, is positioned at a distance of $\approx$1.75 m from the interaction point on either end within CMS. This distance is the point with the maximum time separation between the particles and beam halo from the incoming beam and the collision products from the interaction point[Dab14]. However, the position within the CMS pixel detector volume, just behind the two Forward Pixel disks, also brings many constraints. The space for the detectors is limited and was one of the driving factors for the mechanical design of the PLT and its mounting structure, the material budget had to be kept as low as possible and additional constraints were given by an easy insertion and removal process to access the pixel detector if needed, but at the same time having a fixed detector position and constant alignment for the PLT.

A design drawing of the structure that was ultimately built can be seen in figure 5.3. The basis for the detector mechanics is the carriage made from carbon-fibre-reinforced plastic (CFRP). It consists of a half-circular head and an arm extending back, away from the IP. The light-weight material, made from a polymer matrix reinforced with carbon fibres, gives the mechanical structure high strength and rigidity. On the arm of the carriage the Opto-Hybrid Motherboard and the fibre box for the PLT are mounted. The OHM is inside a

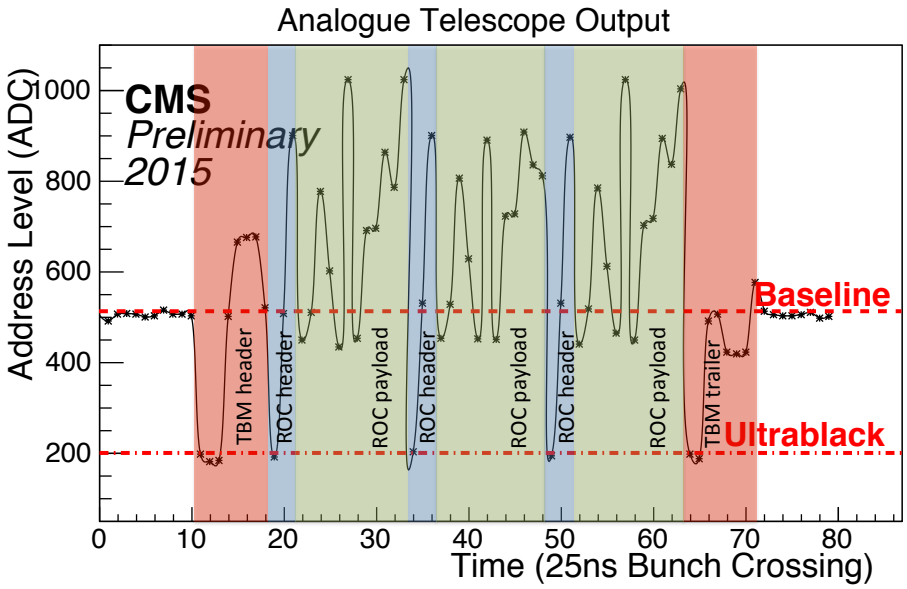

Figure 5.1: **PSI46v2 analogue readout of a single PLT telescope**
The shown 'wave form' plot pictures how the signal coming from a single PLT telescope, consisting of three ROCs and one TBM (see chapter 5.2.1), is sampled in the Pixel Front End Driver (FED). The wave form plot is used to check the correct timing of the sampling points as well as the correct settings for the Baseline calibration. The correct timing of the sampling can be checked by correctly decoding the header and trailer of the Token Bit Manager TBM (red areas) and the three headers from the ROCs (blue areas). After the header of a ROC follows the data payload (green areas), the pixel address encoded in column and row, succeeded by the analogue pulse height. A correct timing is essential to read out all pixel addresses without decoding errors. The Baseline is the value that is being sampled while the system does not transmit any payload. It is calibrated to be at an ADC value of 512 to give a maximum amount of range for the transmission of the address levels in which the pixel data is encoded. The Ultrablack level has a special status. This level is uniquely reserved for headers and trailers. The difference between the Ultrablack to the next higher address level is especially large to make identification easier.

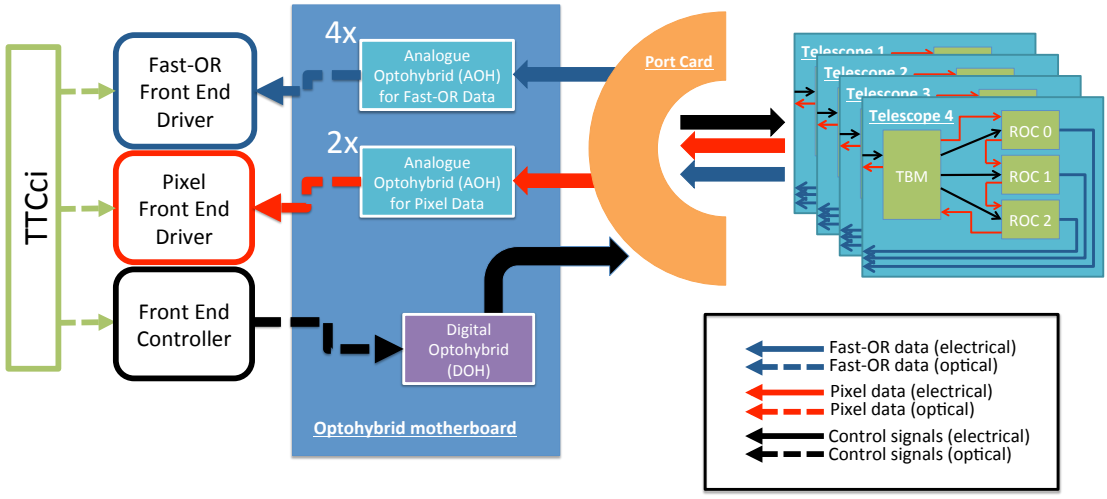

Figure 5.2: **Readout scheme for a single PLT quarter**
Every PLT quarter is made from four small angle telescopes. The three ROCs on each telescope are controlled and read out by the Token Bit Manager (TBM). All electrical signals from and to the detector are routed through the Portcard. On the Opto-Hybrid Motherboard the optical control signals from the FEC are converted to electrical signals. Similarly, the electrical signals from the telescopes are converted and transmitted through optical links on the Opto-Hybrid Motherboard. The data is received by the Front End Drivers (FEDs).

double layered metal box to shield it form external noise sources. The cooling lines, passing along the arm towards the PLT cassette, are thermally connected to this box to dissipate the power consumed by the electronics. Also connected to the arm are auxiliary electronics for the beam condition monitors.

The semi-circular head of the carriage holds the PLT cassette and also the C-Shape electronics for BCM1L and BCM1F. Alignment holes (see figure 5.4) are carefully placed to enable a position survey of the PLT after installation to find the detector's exact location within the coordinate system of the CMS experiment. Two small spring loaded wheels on the front of the carriage and one at the back are used to insert the detectors to their final location on a rail system already in place for the insertion of the Pixel Detector.

The drawings of the mechanical structure of the PLT are shown in figure 5.4. The mounting structure is made from a glass-fibre reinforced plastic (GFRP) frame and the 3D-printed titanium cooling loops (see figure 5.5). The frame connects and aligns the PLT structure with the carriage. Alignment holes are placed on the front of the PLT mounting structure. After installation into the pixel volume of CMS they can be seen from the outside and through the alignment holes in the carriage. The Portcard is placed between the mechanical mounting structure for the PLT and the carriage the PLT is attached to.

The cooling lines of the PLT have been a late addition to the setup, when the decision was made to use silicon instead of the originally intended diamond as sensor material[Bar09]. The titanium alloy pipes of 2.8 mm have been 3D-printed in a process called Selective Laser Melting. This process allows one to create metal structures with complex geometries, thin walls and hidden voids or channels and is perfectly suited for small production batches, like in the PLT detector project. The cooling lines are rated and tested for a pressure of > 15 bar.

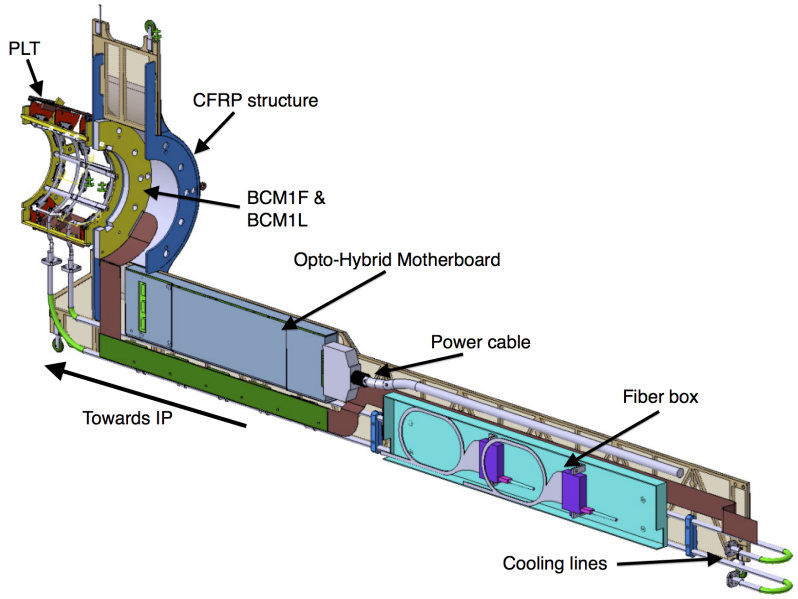

Figure 5.3: **Drawing of the full PLT and BCM carriage**[Loo15]
The drawing shows the CFRP carriage on which the PLT and the BCM are mounted on. On the front of the carriage, towards the interaction point, the PLT is mounted and connected to the cooling lines running C_6F_{14} at a temperature of $-20\,°C$. Behind the PLT the BCM C-shape is mounted on the carriage head. On the arm of the carriage, extending away from the interaction point the Opto-Hybrid Motherboard and the fibre box are placed.

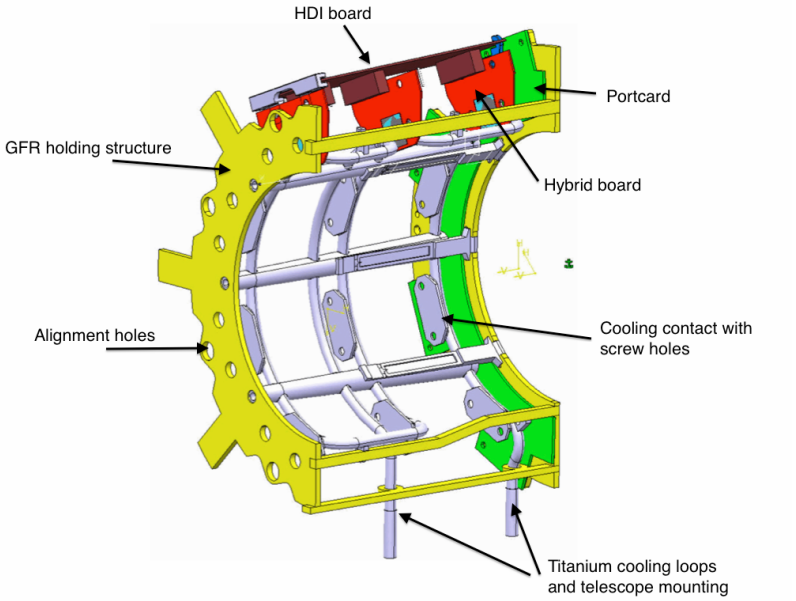

Figure 5.4: **Drawing of the PLT mounting structure and a single PLT telescope** [Loo15]
The PLT cassette consists of a GFRP skeleton fixed to the cooling loops for additional mechanical support. In this frame four PLT telescopes are mounted, only one is shown here. Each plane of the telescope is fixed with two screws and thermally conductive paste for better contact to the cooling structure. Alignment holes have been applied to the front of the GFRP frame. They can be seen after installation of the detector from the outside and are used to measure the PLT's position in the CMS coordinate system.

The four carriages on which the PLT is mounted are fully placed within the insulated volume of the CMS Pixel detector. The sealed volume is constantly flushed with dry air to keep the dew point below the temperature of the cooling lines to prevent the condensation of water.

5.4 Readout and Calibrations

Compared to the CMS Pixel detector the Pixel Luminosity Telescope is a rather small detector, it has only a small fraction of the pixel detector's number of channels. Nevertheless the same strict requirements on a proper configuration and calibration of all ∼200k readout channels applies. During the construction phase of the Pixel detector a database with different sets of calibrations for different operating temperatures and different single pixel thresholds was created. During operations only few parameters are being monitored and consistently adjusted to compensate for radiation damage in the ROCs and the sensors without re-calibrating the entire detector. For the PLT it is important that all calibrations can be done in-situ after the detector was installed. This decision was made due to the fact that the PLT operation temperature is dependent on the temperature of the CMS Strip Tracker since the PLT is only connected parasitically to the Tracker's cooling plant. Also it is of outmost importance for the PLT to measure and understand its own efficiency. For this the

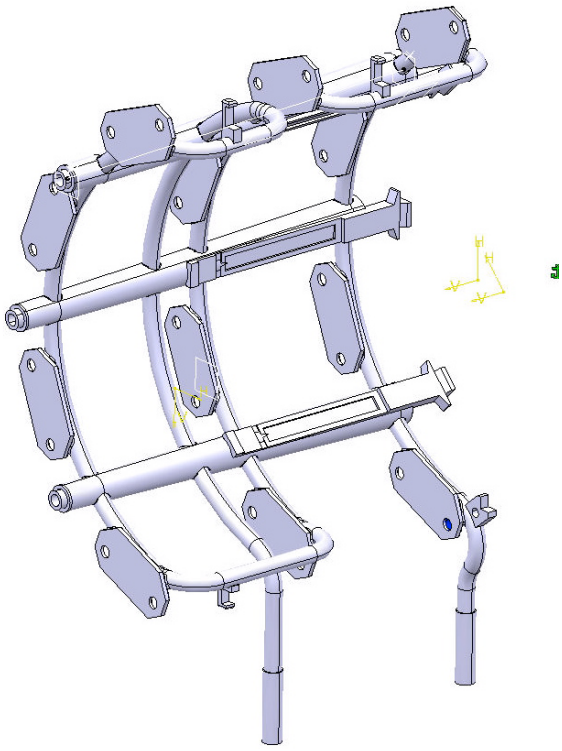

Figure 5.5: **PLT cooling and mounting structure fabricated using the Selective Laser Melting (SLM) process** [Loo15]
The entire PLT cooling loop structure is made from a single piece of titanium alloy fabricated in the Selective Laser Melting process.

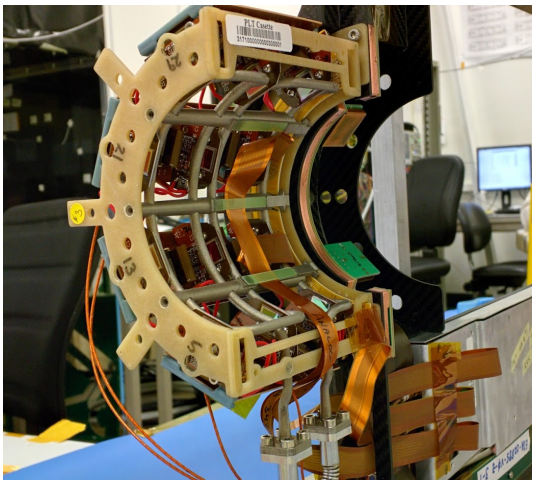

(a) **Picture of a single PLT quarter fully equipped with 4 PLT telescopes**

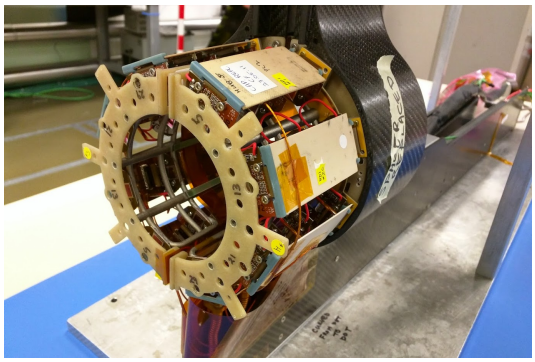

(b) **One full end of the PLT detector assambled**

Figure 5.6: **The PLT detector assembled in the clean room**

currently applied pixel threshold is a vital measurement. After irradiation, thus collecting a reduced signal charge from the damaged silicon sensor, it might be required to adjust the pixel thresholds.

In the framework of this thesis, code was written for the PLT to measure and unify the single pixel threshold on all ROCs of the detector. The following part of this chapter will describe how the calibration for the PLT is obtained and also discusses why a good calibration is essential for the successful operation of this particular detector.

5.4.1 Readout Configuration

The pixel data from the PSI46v2 readout chip is zero-suppressed, i.e. only the information about successfully detected hits is transmitted during a readout. This also means that for every hit the pixel address needs to be transmitted in addition to the pulse height. An important part of the calibration of the PLT detector is to make sure that all pixel addresses and the header and trailer information from the TBM are decoded correctly and that every hit is associated to the correct ROC. An example of the data stream measured in the FED is given in figure 5.1.

Baseline Calibration

In the Front End Driver the incoming optical signal from the Opto-Hybrid Motherboard (OHM) is sampled at a constant rate by a 10-bit ADC. When no information is transmitted the Baseline value is supposed to be relayed by the AOH. To ensure a maximum possible amplitude for the output signal this Baseline value is calibrated to be at 512 ADC units, exactly the middle of the ADC range.

Due to temperature changes in the AOH, after turning on the detector or fluctuations in the cooling liquid temperature, the baseline can drift since the laser output drivers are temperature dependent. This Baseline drift is constantly monitored and adjusted for during the operation of the PLT.

Ultrablack Calibration

To correctly separate the transmitted data payload from a sequence of ROCs read out in series, the end of a ROC's readout and the start of the next ROC's readout need to be unambiguous. Also the FED needs to be able to recognise when a new event is being sent. For both of these tasks a special signal level, called Ultrablack (UB), is used. The UB signal level simply marks the lower boundary of the output signal range of the ROC and the TBM.

Every TBM header starts with three UB levels, followed by a black level. The black level defines the zero value of the differential analogue output. It is equivalent with the transmitted 'Baseline'. The next four clock cycles of the readout encode an 8-bit event number [TLP08] that is used to synchronise readouts from different telescopes in the PLT or different modules in the CMS Pixel detector. Equivalently the TBM trailer, which marks the end of a certain event readout, starts with two UB levels and two black levels. The following four clock cycles carry status information of the event.

Like the TBM header, the ROC header has a fixed pattern. The ROC header is three clock cycles long and starts with an UB level that is followed by a black level. The last transmitted level, the 'last DAC', either displays the last value to which the last Digital to Analogue Converter (DAC) was set or the ROC temperature.

TBM and ROC Levels Calibration

The information transmitted in the TBM header and the ROC payload is encoded in analogue levels (see figure 5.7). These levels need to be well separated to ensure as few as possible readout errors. The ROC and the TBM have DACs that allow one to change the signal output offset (VIbias_roc for the readout chip) and to change the range over which the levels are spread (VIbias_DAC of the readout chip) [Gab05]. A list of all DACs of the PSI46v2 readout chip can be found in table 4.1. After these DACs are set to minimise chip-by-chip variations the levels for every ROC and every TBM are measured and used as constants in the address decoding in the back end electronics.

To measure the levels, every pixel of a ROC is addressed, a calibration readout is triggered (see section 5.4.2) and the measured address levels for every ROC and TBM are histogrammed. To measure the address levels every pixel of a ROC is activated separately and a calibration trigger is sent to it. If the calibration signal is high enough to cross the set pixel threshold, the ROC will respond by sending the address of the activated pixel and the measured pulse height. In the FED the different address levels are sampled by an ADC. The measured ADC values of all occurring pixel address levels are then histogrammed as shown in figure 5.7. A simple peak finder algorithm looks for the four levels in the TBM data and the six levels in the pixel address data. Level boundaries (red lines in figure 5.7) are placed and mark how the FED will distinguish the different levels after this calibration. The levels are decoded on a per chip level to decrease the number of potential readout errors even further.

5.4.2 Pixel Threshold Measurement

A hit pixel on the PSI46v2 readout chip is only detected when the collected charge from the attached sensor exceeds a predefined comparator threshold. This threshold is measured using a ROC internal calibration pulse, the schematics of which are shown in figure 4.2. Each pixel of the ROC has the option of being connected to a circuit that, when triggered externally, releases a fixed amount of charge. The height of this charge pulse is determined by the *Vcal* DAC. Two possibilities for the connection are available, either the charge is directly injected into the pixel unit cell or to a pad on the outside of the pixel next to the bump bond connection to the sensor. The latter option is used to test for missing or bad bump bonds[S$^+$05]. In the following only the direct injection into the preamplifier-shaper circuit will be discussed.

Two different methods of measuring a pixel threshold are possible: a fixed calibration charge against a varying comparator threshold or a fixed comparator threshold and a varying calibration charge. In both cases the threshold is always defined as in-time threshold, that means only the pixel responses in one fixed bunch crossing are considered valid. Small signals with slow rise time and thus crossing the comparator threshold in a later bunch crossing are not counted.

The pixel threshold is determined by a measurement of the response efficiency, the so called S-Curve, of a pixel as a function of the applied calibration signal amplitude or the applied comparator threshold. For an ideal readout circuit and ideal sensor with zero efficiency below and full efficiency above threshold a step function would be expected. Due to noise, the step function is smeared out in a real detector, as seen in figure 5.8. Under the assumption that the noise follows a Gaussian distribution, the resulting S-Curve will have the shape of an error function. The width of the measured error function is proportional to the noise of the pixel. The pixel threshold is defined as the point where the error function fitted to the data

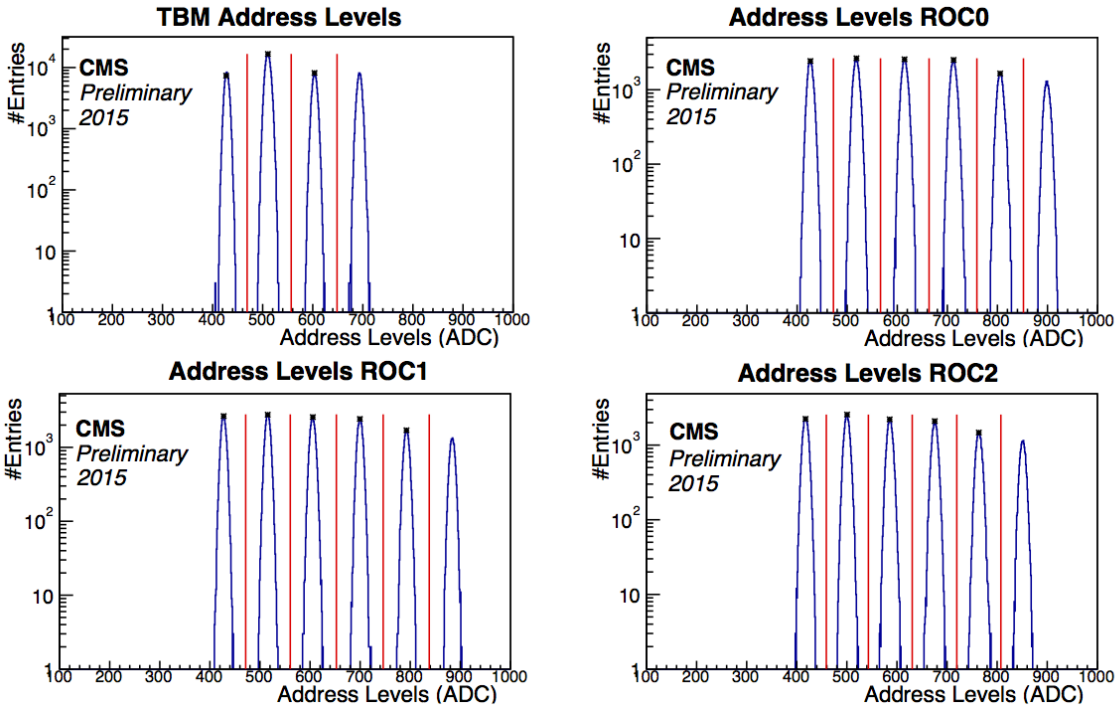

Figure 5.7: **Analogue readout levels measured for an entire PLT telescope**
Shown are the pulse height calibrations for an entire PLT telescope consisting out of three ROCs and one TBM. Four different levels are distinguished for the TBM. The ROC data is encoded in six different levels. All levels should be well separated to read back data without any error. The address level calibration addresses every pixel on each ROC, sends a calibrate signal to this pixel and histograms the address levels of the returned pixel hit. The program finds the peaks in the distribution and decides which pulse height in ADC corresponds to level boundaries, marked as red vertical lines.

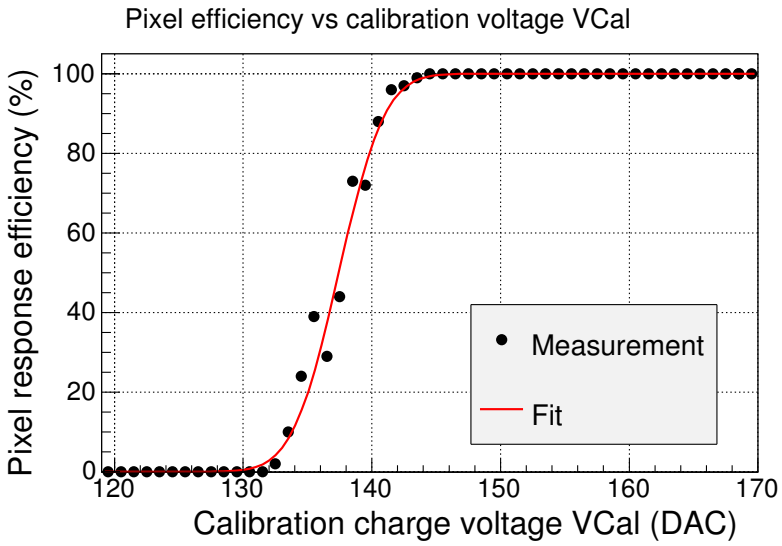

Figure 5.8: **S-Curve measurement**
The threshold of a pixel is determined by measuring its response efficiency with respect to a varying comparator threshold or calibration charge. In the measurement shown here the comparator threshold was kept constant and the calibration charge was increased. Each measurement point shows how often the pixel responded to the injected charge. An error function can be fitted to the measurement of the response efficiency and describes the measurement very well. The noise of the pixel is proportional to the width of the error function.

points crosses the 50% mark.

5.4.3 Threshold Unification

The PLT is designed to measure the luminosity delivered to the CMS experiment by counting the number of trajectories going through 16 small-angle telescopes placed on each end of CMS. For this task it is essential that all three hybrid pixel assemblies in a telescope respond equally to the charge deposited by a passing particle, thus it is important to have a uniform single pixel threshold on all telescopes.

Calibration Signal Timing

After the readout of all telescopes has been configured correctly as described in section 5.4.1 the readout chip has to be configured to respond correctly to its own calibration pulse. The rise time of a signal is commonly defined as the time required to transition from 10% to 90% of its maximum amplitude and in the case of the charge injection pulse the rise time is independent of the signal height. This leads to the 'timewalk' effect: Signals with smaller amplitude cross the pixel comparator threshold at a later time than signals with large amplitude (see figures 5.9a and 5.9b).

The calibration signal circuit in the PSI46v2 ROC is equipped with a delay circuit. It can be set externally by addressing the *CalDel* DAC of the readout chip[Gab05]. Before any other calibration step can be performed efficiently, this *CalDel* value has to be set correctly to ensure good response of the pixel unit cell to the calibration signal. To do so a

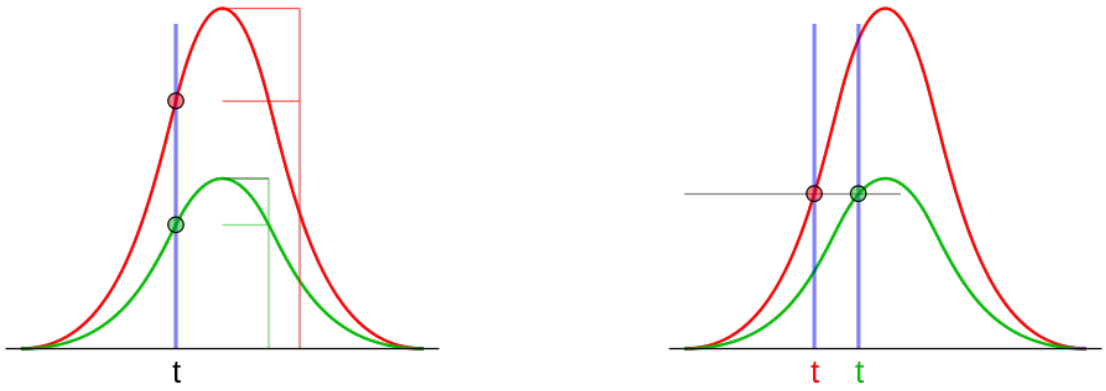

(a) (b)

Figure 5.9: **Timewalk effect**
(a) Although both signals, green and red, have different amplitudes they have the same rise time, the time the signal takes to rise from 10% to 90% of the maximum amplitude. In figure (b) the time it takes both signals to surpass a fixed threshold is compared. The signal with the larger amplitude reaches this threshold earlier than the small amplitude signal. Signals with small amplitude are registered later by a simple comparator threshold and in some cases can be assigned to the wrong bunch crossing. This is called the timewalk effect.

map of the pixel response efficiency with respect to the calibration delay *CalDel* and the pixel threshold comparator voltage DAC *VThrComp* is measured for a constant calibration charge. A measurement in which five calibration signals were sent to a single pixel at every combination of *CalDel* and *VThrComp* and the number of correctly registered pixel hits was histogrammed can be seen in figure 5.10. In the measured phase space of *CalDel* and *VThrComp* the optimal working point for further calibrations is chosen by finding the center of the fully responsive area. With this setting all pixels respond with high efficiency to the ROC's internal calibration pulse.

Global Threshold Voltage Setting

An important parameter defining the individual pixel threshold is the global threshold comparator voltage *VThrComp*. This is again a ROC internal voltage controlled by the 8-bit DAC of the same name. The threshold is inversely proportional to this DAC setting, i.e. with a higher *VThrComp* the pixel readout is triggered by a signal of smaller amplitude.

When unifying the thresholds of all 4160 pixels on a single readout chip a *VThrComp* value as high as possible is chosen. As shown in figure 4.2 every pixel unit cell has 4 bits, called *Trim Bits*, that also influence the comparator threshold by regulating how strongly the trimming voltage *VTrim* changes the threshold of every single pixel. For a single pixel the threshold dependence can be expressed as in the following equation:

$$Threshold \sim VThrComp - (TrimBit \cdot VTrim) \tag{5.12}$$

Since by adjusting *VTrim* the pixel threshold of a pixel can only be lowered, a high *VThrComp* value needs to be chosen, so that all pixels can be brought down to the same

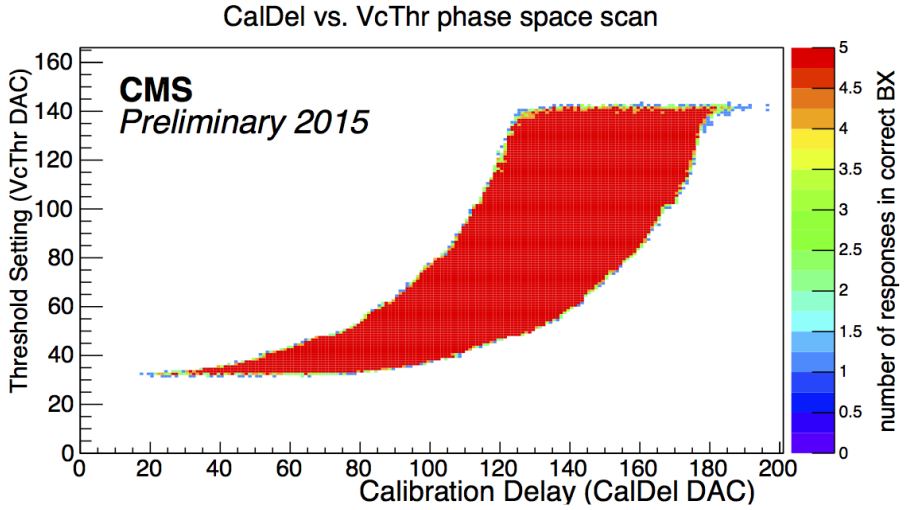

Figure 5.10: **Scan of calibration charge delay vs. pixel comparator threshold**
For different combinations of *CalDel* and *VThrComp* five calibrations pulses are sent to a single pixel and the number of registered correctly timed responses is counted. A working point in the center of the found fully responsive area is chosen for further calibrations.

threshold value. To find this highest *VThrComp* value, an S-Curve measurement with a fixed calibration charge value versus a changing comparator threshold, as described in section 5.4.2, is performed. During these calibrations all *Trim Bits* are off and *VTrim* is set so that the threshold in the global threshold comparator voltage is measured. The lowest *VThrComp* found will give the value for all other calibrations. The only restriction applied is that the value should be less than $5\,\sigma$ from the mean of the distribution found on a ROC. An example of the result of such a measurement can be found in figure 5.11.

Global Trim Voltage Setting

The next parameter that has to be set on the PSI46v2 readout chip is the global trim voltage *VTrim*. It needs to be set high enough so that all pixels can be trimmed down to the desired threshold by adjusting the *Trim Bits*. To find the correct *VTrim* setting, the one pixel with the highest threshold in *VCal* needs to be found. Then, with all trim bits enabled, the threshold of this pixel is repeatedly measured while *VTrim* is being increased until the measured threshold reaches the target value. Using the pixel with the highest initially measured threshold ensures that by adjusting the *Trim Bits* of the other pixels on the readout chip the target value can be reached.

Trim Bit Adjustment

The last step in unifying the response behaviour of all pixels on a single ROC is to set the *Trim Bits* on all pixels such that their measured threshold in *Vcal* is as close as possible to the target value. An iterative approach to finding the optimal *Trim Bit* settings was chosen, since measuring all 16 possible setting for every pixel would have been too time consuming with the PLT framework installed in CMS. The binary search algorithm starts with $TrimBit = 7$

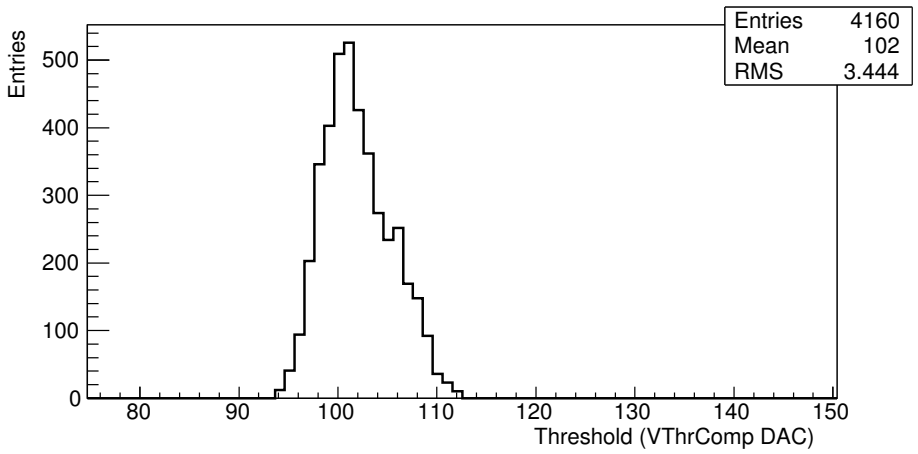

Figure 5.11: **Distribution of measured pixel thresholds in *VThrComp* of a single PLT ROC before threshold unification**
To find the correct *VThrComp* setting for a ROC, the threshold is measured for all pixels. The lowest value of *VThrComp*, which corresponds to the highest threshold, within a 5 σ window around the mean of the distribution is used as global setting for the ROC.

for all pixels, measures their threshold and then decides if the optimal value was found or if a higher or lower *Trim Bit* value is needed. The maximum number of iterations needed to find the best matching value for the 16 possible values is

$$\log_2(16) = 4. \tag{5.13}$$

Thus the binary search is four times faster than measuring the pixel threshold for all possible *Trim Bit* settings and deciding afterwards which the best setting is.

In figure 5.12 the results of the procedure described above are shown. The comparison of the measured thresholds in *VCal* on a ROC before and after trimming is seen in figure 5.12a. The previously wide distribution of thresholds narrows down a lot, more than 75 % of thresholds are at the target value of 60 *VCal*. Also when looking at all the measured thresholds from 41 ROCs after successfully passing the threshold unification calibration the measured distribution is very narrow with only small tails to larger or lower values than the target that was aimed for, as seen in figure 5.12b.

After this calibration of the readout chip has been executed, the pixels on a single ROC all have nearly the same threshold. This threshold is set well below the most probable value of charge deposited by a minimum ionising particle and well above the expected noise level of the sensors.

5.4.4 Fast-OR Calibration

An integral part for the design of the PLT detector and the proposed luminosity measurement method is the PSI46v2 fast cluster counting signal, or *Fast-OR* signal[Bar03]. This feature of the readout chip was originally thought to be used as additional input for the CMS Level-1 trigger system. Yet, neither in the CMS Barrel Pixel, nor in the CMS Forward Pixel the *Fast-OR* was ever used.

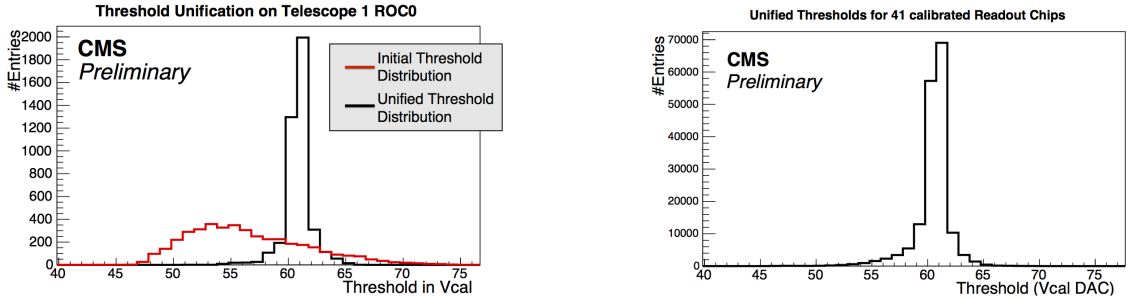

(a) (b)

Figure 5.12: **Threshold Unification**
Panel (a) compares the initial distribution of measured thresholds of a single ROC with the distribution of measured thresholds after the unification calibration has been performed. A target value of *Vcal* 60 was chosen. This threshold value corresponds to ≈3000 electrons. Although a quite narrow distribution can be achieved, not all pixels of a ROC can reach exactly the desired threshold value. The 16 settings of the trim bits have a limited precision that depends on the trim voltage *Vtrim*.
Panel (b) shows the measured threshold distribution for 41 calibrated chips (170560 pixels). A value of *Vcal* 60 has been chosen as target for the threshold of all pixels. Over all ROCs good threshold uniformity could be achieved. All edge pixels, which tend to be noisier then central pixels, will be disabled in the final running configuration.

The *Fast-OR* works in the following way: when in one bunch crossing a double column detects one or more hits above threshold a flag in the double column periphery is set. Sweeping over all 26 double columns of a ROC, an internal signal counts the number of transitions between "hit double column" and "un-hit double column" for each clock cycle. Every transition counts as a cluster, so for the *Fast-OR* mechanism the ROC works like a short silicon strip sensor, with a pitch of 300 µm and a strip length of 8.1 mm and clusters are formed by neighbouring double columns being hit, not a grouping of single pixels. The *Fast-OR* signal coming from the ROC itself is an analogue pulse height encoding the number of clusters found in a particular clock cycle or a differential trigger signal of fixed amplitude depending on how many clusters are found. This signal is available for every 25 ns bunch crossing.

When setting up the readout chip to use this cluster counting signal, there are two ROC internal DACs influencing the behaviour [Bar03] [Gab05]. The first is called *Vnpix*. It controls the number of single pixel hits in a double column needed to flag the double column itself as hit for the *Fast-OR* signal. In the PLT the *Vnpix* DAC is always set in a way that a single pixel hit is enough to create a trigger. The second DAC is called *VsumCol*. It makes it possible to set a maximum on the number of clusters in a bunch crossing. If this threshold is passed, the ROC will output the differential trigger signal, otherwise the Differential Trigger Output Driver will send the analogue pulse height proportional to the number of clusters found. During PLT operations the cluster threshold of each ROC is set so that up to three clusters are counted before the binary signal is transmitted.

Baseline Calibration

Like the full pixel readout data, the *Fast-OR* signal from the ROC has to be transmitted via an optical link to the Front-End Driver. The same AOHs which are used for the pixel readout data stream and are described in section 5.2.2, are used for the *Fast-OR* data. The only difference is that while the pixel data of the three ROCs of a single telescope can be congregated in a single data stream, each ROC needs its own *Fast-OR* data line. Since one AOH only has 3 optical connections, four AOHs on the Opto-Hybrid Motherboard are dedicated to transmitting all *Fast-OR* signals of a PLT quarter.

As already described, for the full pixel data the baseline for the optical link needs be calibrated. The *Fast-OR* signal is either an analogue pulse or a fully differential trigger signal. Thus the baseline is not set in the center of the 10-bit ADC range of the FED input but in the low range at 200 ADC counts. The baseline for the *Fast-OR* signal is kept at a stable value during operations by repetitively adjusting the baseline offset in the FED, mostly to compensate small temperature changes in the AOH electronics.

Timing Calibration

The way the PLT will measure the luminosity delivered to CMS is by counting the number of three-fold coincidences of the *Fast-OR* signals in all telescopes. That is why the correct timing of the *Fast-OR* signals is of foremost importance for a precise measurement. The optical fibre connections were designed and chosen to have as little difference as possible in travel time for the different signals. In contrast to the pixel data the *Fast-OR* signals do not have an event counter that would make it possible to combine them to a single event in the FED. All signals arriving in the same 25 ns bunch crossing in the Front-End Driver are assumed to have happened simultaneously in the telescope. The only possibility of influencing this is to adjust the input delays for the incoming data streams. Using the ROC internal calibration pulse makes it possible to tune the three *Fast-OR* signals of a single telescope to be sampled at the same time in the FED. It also makes it possible to tune the timing of all telescopes to ensure to see the same bunch crossing in all channels simultaneously.

Fast-Or Level Calibration

The analogue output mode of the *Fast-OR* not only delivers information about whether or not a ROC was hit in a bunch crossing, but also delivers information about the number of clusters found on a ROC. When creating a coincidence of the three *Fast-OR* signals of a single telescope, additional information about the delivered luminosity can be gained by comparing the number of clusters seen on each ROC.

To calibrate the cluster counting mechanism pixels on separate double columns are activated and calibration pulses are sent to them. The amplitude of the analogue output signal is measured for the different number of clusters found, and level boarders are set to be able to distinguish between them. To be able to distinguish the cluster count in the best possible way, the ROCs in the PLT are calibrated to only count up to three clusters, before sending the binary differential signal.

5.5 First Measurements

The installation of the PLT into CMS was performed on 22$^{\text{nd}}$ January 2015. After both halves had been mechanically inserted the first tests checked if all electrical and optical connections

were routed correctly and the cooling lines were pressure tested. The PLT passed all test – the installation was successful.

During the following weeks the PLT team brought the detector into an operational state. All calibrations described in the previous section 5.4 were performed after the PLT had reached its operation temperature of −20 °C. In the framework of this thesis the threshold unification was performed. When the first collisions of LHC RUN II happened in CMS on 5^{th} May 2015 the PLT detector was fully calibrated and ready to take its first data. Over the course of several weeks while the LHC ramped up the collision energy from initially 900 GeV to the nominal 6.5 TeV for providing physics data, the luminosity measurement of the PLT was continuously refined and improved.

Luminosity measurement with the PLT

The PLT uses the zero counting method to measure the luminosity in CMS, see section 5.1.1. The luminosity is derived from the number of three-fold coincidences of the *Fast-OR* signal found in every 25 ns bunch crossing of the LHC. The *Fast-OR* FED creates a histogram for each of the PLT telescopes with each of the histograms' bins corresponding to one of the 3564 RF buckets in an LHC orbit. After integration of the counts for every telescope and every bunch crossing over 4096 LHC orbits, or one 'lumi nibble', the numbers are released to the PLT PC for processing. The probability of having no interactions measured in the PLT in a bunch crossing $p(0)$ can be obtained by counting the number of empty bins in all histograms divided by the total number of bins

$$p(0) = \frac{\#\text{bins without any three-fold coincidences}}{\#\text{bins in all histograms}}, \tag{5.14}$$

thus providing a value proportional to the instantaneous luminosity delivered to CMS.

Should the instantaneous luminosity ever increase to a value for which all histogram bins are filled (zero starvation), the acceptance window of the readout chip for pixel hits can be decreased. This is already done in the current detector configuration as seen in figure 5.14b. The geometric acceptance window for hits on the central plane of the shown telescope is reduced to a 4 mm × 4 mm square. Effects from background particles can be corrected for by using additional information from particle tracking obtained from the pixel data. Tracks coming from the IP can be distinguished from tracks created by background particles by their slope through the small angle telescopes.

From the time the LHC started providing particle collisions again in 2015[O'L15] the PLT has been operational and running. It performs well compared to the luminometers established in the previous LHC RUN: the Hadron Forward Calorimeter (HF lumi) and the Beam Conditions Monitor (BCM). A comparison of the measured rates during a mini VdM scan can be seen in figure 5.13. At all times the device with the smallest uncertainties of the three luminometers publishes the CMS luminosity value to the LHC.

Full Pixel Data

Not only does the PLT count the *Fast-OR* conincidences, but it also provides the full pixel data from the readout chips, making it possible to reconstruct tracks (see figure 5.14) to measure the detector performance and also the location of the collision point centroid (see figure 5.15). The PLT pixel data is entirely self-triggered by the triple coincidences found in the *Fast-OR* signals. This makes the readout independent from the Level 1 trigger signal globally distributed to the CMS experiment.

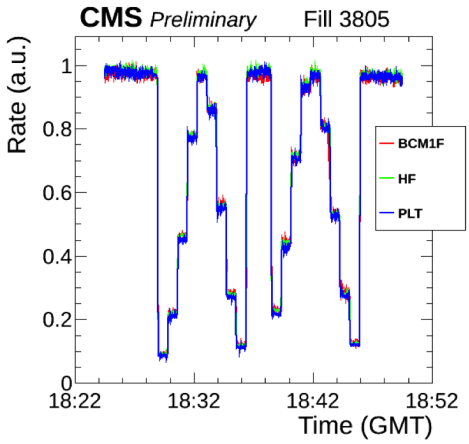

Figure 5.13: **Comparison of the luminosity measured by PLT, HF lumi and BCM**
The measured luminosities of the PLT, the Hadron Forward Calorimeter and the Beam Conditions Monitor are compared. All values are normalised to one at the maximum value, independently for each detector. The data was taken during a short Van der Meer scan in which the beam separation was changed over a short time scale. All three detectors track the change in the measured luminosity over an order of magnitude.

In figure 5.14a one can see the effect of a small misalignment of the telescope planes with respect to each other: Areas with a reduced number of reconstructed tracks form. During PLT operations the active region of the center plane is limited to a 4mm × 4mm active region, reducing the number of tree-fold coincidences and tracks as seen in figure 5.14b.

Figure 5.15 shows the beam spot reconstructed from the first data taken with the PLT. The measurement finds tracks through the telescopes of the PLT and extrapolates them back to the interaction point within the CMS experiment. The measurement is most sensitive in the xy-plane. In the yz- and xz-plane the small angle under which the PLT is facing the IP and the large distance between IP and PLT make the measurement less sensitive.

So far all pixel data from the PLT are stored and analysed offline after a run has finished. Work to integrate PLT full pixel information, such as track occupancy plots for all telescopes and the beam spot measurement, into the central data quality monitoring of CMS is ongoing.

5.6 Summary and Outlook

The Pixel Luminosity Telescope was successfully installed into the CMS experiment in early 2015. It passed all necessary commissioning and qualification steps before the LHC started to produce proton-proton collisions during its second run period. The LHC took several weeks of commissioning to increase the beam energy from 450 GeV to the 6.5 TeV. This time was well used to test and commission the PLT detector. The PLT is able to measure the instantaneous luminosity and its measurements agree well with the already established luminometers in CMS. A full Van der Meer scan has not yet been performed to obtain an absolute calibration of the luminosity delivered to CMS. The PLT measurement is scaled to the luminosity measured by the Hadron Forward Calorimeter.

In the future the PLT sensors and readout electronics in CMS will collect high doses of

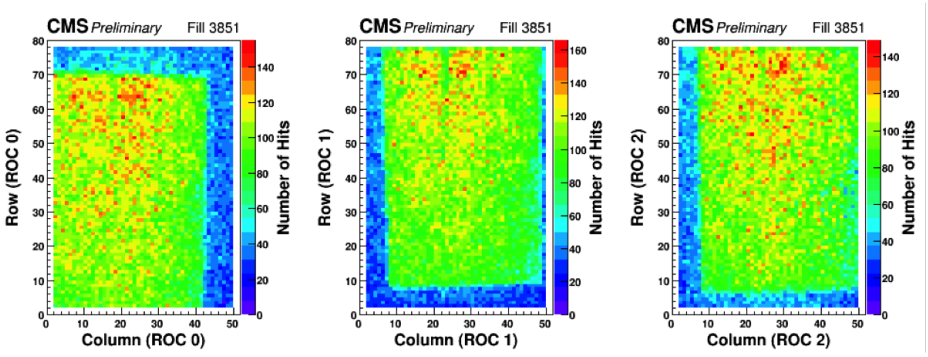

(a)

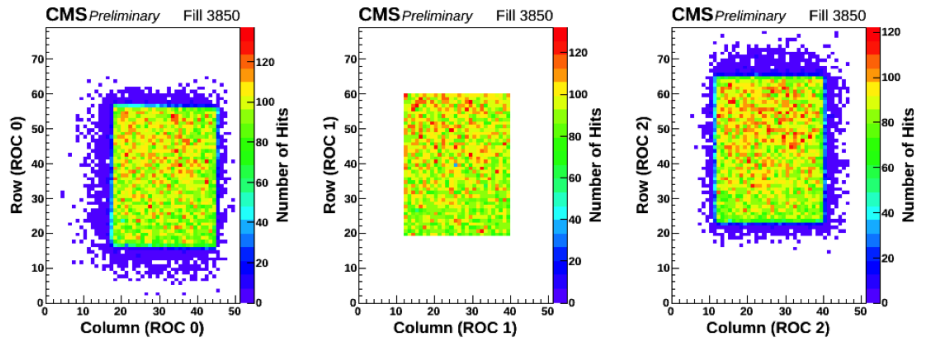

(b)

Figure 5.14: **Track occupancy for a single small angle telescope of the PLT**
Panel (a) shows shows the occupancies in the three planes of a single telescope in the Pixel Luminosity Telescope over the course of a single LHC fill. Events are triggered by requiring a three-fold coincidence in any of the telescopes in the PLT. The effect of misalignment in the PLT can be clearly seen, and the occupancies are relatively uniform in the active region.
Panel (b) shows the occupancies in a single telescope of the PLT with a mask applied to reduce the active area of the central plane to 4 mm × 4 mm. This plot shows only events in which a three-fold coincidence occurred in this specific telescope, allowing to measure the effects of alignment and background particles.

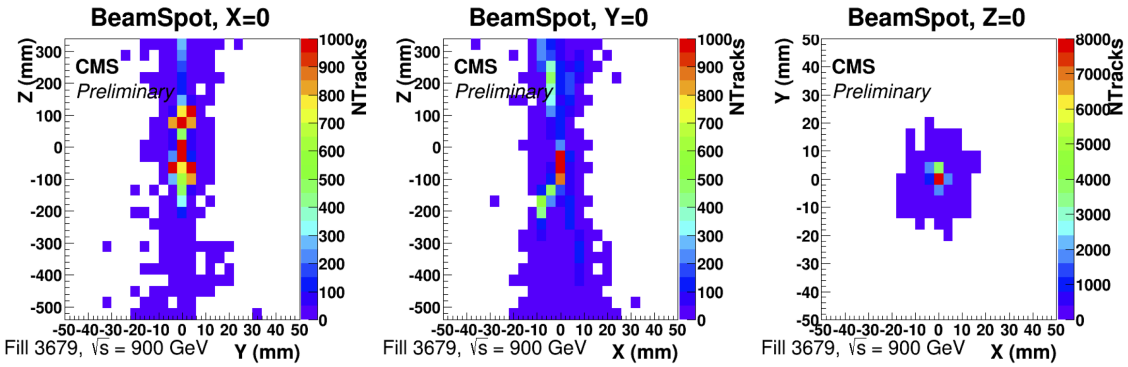

Figure 5.15: **The collision point centroid within CMS as measured by the PLT**
From the tracks measured in the Pixel Luminosity Telescope (PLT) a beam spot is reconstructed as an offline measurement. Shown are the cuts in three different planes through the interaction point. The measurement is most sensitive in xy-plane due to the small angle under which the PLT is 'looking' at the IP.

radiation. Over time the collected charge in the sensors will decrease and the applied high-voltage needs to be increased or the threshold might need to be adjusted to lower values. The expected lifetime of both, sensors and readout chips, is long enough to operate until the next long shutdown (LS2) in 2019. During an extended technical stop end of 2016 the PLT will have to be de-installed to replace the CMS pixel detector. This will be an opportunity for major maintenance work on the PLT if needed.

Chapter 6

A High Rate Beam Test

Measuring the performance of a detector is essential to understand its behaviour in the experiment it is, or will be, used in. Beam tests in precisely defined environmental conditions are generally used to study new detector prototypes during research and development phases and final detector assemblies before going into the production phase for high energy particle physics experiments. The detector to be studied, is placed and operated in a particle beam of known energy and known rate, that mimics the real experimental environment.

Beam telescopes, several consecutive planes of particle tracking devices, are used in beam tests to reconstruct the tracks of particles. From the reconstructed tracks the performance of the detector under study can be determined. When studying a tracking detector itself two different kinds of beam telescopes exist. The first type consists of several layers of the same detector whose performance needs to be studied. The second type is made from planes of well-understood detectors between which the detector to be studied, the Device Under Test (DUT), is placed.

To be able to cope with the higher instantaneous luminosity and the higher hit occupancy on the CMS Pixel detector, a new readout chip, the PSI46dig, was designed. The readout chip 'evolved' from its predecessor by keeping the changes made to the chip's readout mechanism and outer appearance as little as possible, while at the same time fulfilling the higher requirements posed at the ROC. To ensure that the PSI46dig ROC works as expected and to test for potential design errors the High Rate Test Beam campaign was started.

To study the PSI46dig readout chips performance in a high rate environment a series of test beams were performed. Early prototype versions of the readout chip were used in two high rate test beams at the *H4IRRAD* beamline at CERN. The final version of the telescope described later was first tested in the *piE1* beam line at PSI. The final test beam with the last prototype version of the PSI46dig chip was tested at the newly commissioned *High Rate Tracking Area* of the Fermilab Test Beam Facility in Batavia, Illinois.

This chapter will give a detailed overview of the telescope and data acquisition system used for the test beam. The device used to measure the beam intensity will be shown and the beam structure found at Fermilab will be discussed. In the scope of this work, only the last test beam performed in February and March 2014 is relevant.

6.1 The High Rate Pixel Telescope

The beam telescope is the central part of every test beam experiment. Many devices well established in the scientific community, like the EUDET telescopes [Rub12], already exist. Yet, the harsh environmental requirements of the High Rate Test Beam, with particle rates of up to $500\,\mathrm{MHz\,cm^{-2}}$, and the demand for a fast readout made it impossible to use one of these telescopes for this purpose. The MIMOSA26 readout chip, that constitutes the tracking planes of the EUDET telescope, was especially designed for the use in a tracking telescope.

Its advantages are its large area of 13.7 mm by 21.5 mm and its very small thickness thanks to the monolithic design concept of combining sensor and readout chip in a single piece of silicon. The small pixels with a pitch of 18.4 µm create an excellent spatial resolution of $\sigma < 5\,\mu m$. However, the MIMOSA26 chip also has its disadvantages. The 'rolling shutter' readout mode with a readout time of $\approx 100\,\mu s$ is much too slow to handle the high track rate in an LHC-like environment. Also the radiation hardness of the readout chip is very limited. The charge collection efficiency of the thin epitaxial layer of 14 µm on the MIMOSA chip is greatly reduced after irradiation and for this reason also the track detection efficiency of the EUDET telescope.

A new telescope, the High Rate Pixel Telescope (HRPT), was developed to address these issues. The HRPT seen in figure 6.1 is made from eight planes of PSI46dig readout chips, the same readout chip it aims to study, equipped with single chip pixel silicon sensors (see section 4.3 in the PLT chapter). One of the planes is used as the DUT, while the others are used for particle tracking. The stack of readout chip and sensor has been glued to a single sided circuit board, the carrier board. This 4 cm by 4 cm circuit board only contains a fan-out circuit from the pitch of the *SAMTEC - MB1* connector to the pitch of the wire bond pads for external voltages on the readout chip and a small noise filter circuit for the high voltage connection going to the sensor. The carrier boards are widely used in the CMS pixel collaboration to test single ROC prototypes. Sticking to the same standard made it easy to test and qualify sensors on the lab bench and then use them in the test beam.

In this section the design of the electrical components of the High Rate Pixel Telescope are described and pictured.

6.1.1 Back Plane and Telescope Cards

To make the eight separate sensor planes work as a telescope they have to be operated synchronously. Signals like the 40 MHz clock and the trigger signals need to arrive at all ROCs at the same time. Also the high and low voltages need to be distributed to all detector planes in parallel. Signals like the control signals of voltage regulators in the ROC periphery are addressed to a specific readout chip. The Back Plane and the Telescope Cards have been designed to handle all these tasks.

Back Plane

The Back Plane (BP) is a multi-layered printed circuit board (PCB) with a larger 40-pin connector on the side and eight 26-pin connectors lined up in the center. The BP is powered by a 3.3 V DC power supply. The 40-pin connector connects the telescope with the readout and control electronics. In the eight 26-pin connectors the Telescope Cards (TCs) are plugged in. Several signals that need to arrive synchronously to the ROCs are split in the telescope plane and fanned out to the eight ROCs of a telescope. As an example the line transmitting Calibration, Trigger and Reset (CTR) signals to the ROCs is given. The signals arrive from the DAQ system through a twisted pair flat band cable to the BP on the 40-pin connector. The CTR signal is a low voltage differential signal (LVDS) with an amplitude of 2.5 V. The signal is fed to a LVDS signal repeater with eight output ports, the *Texas Instruments SN65LVDS108* chip [Ins15a]. The separate output ports are connected by meandering signal lines to the TC connectors. During the design of the BP special emphasis was put on all signal lines having the exact same length for all ROCs. By this it was guaranteed that the signal would arrive at the same time at all ROCs, with a spread smaller than 200 ps. This

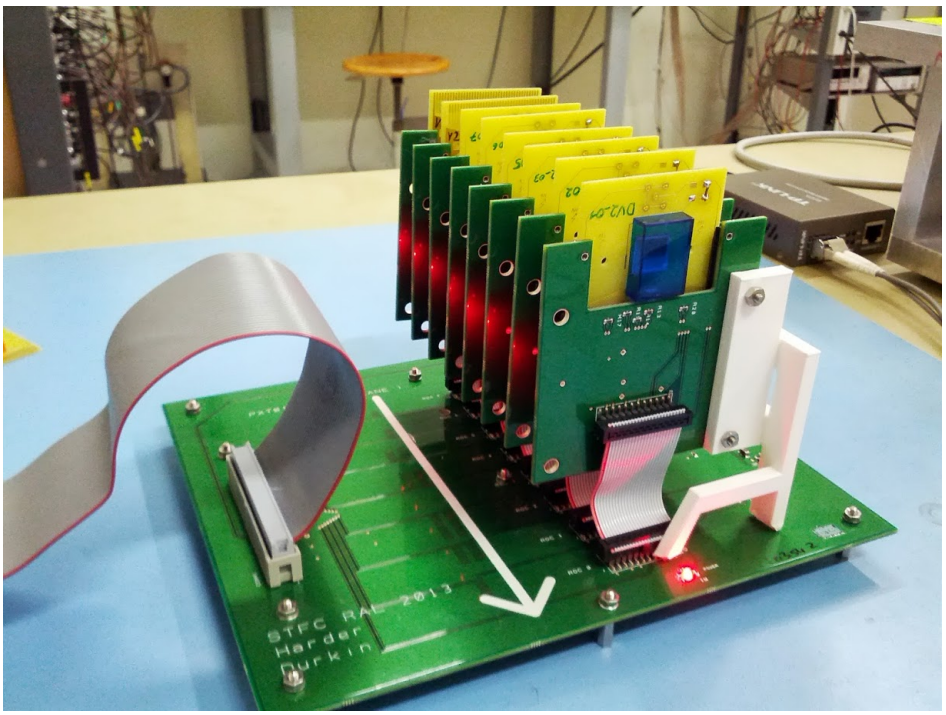

Figure 6.1: **The High Rate Pixel Telescope**
The High Rate Pixel Telescope (HRPT) is made from eight layers of pixelated silicon sensors that are read out by the PSI46dig readout chip. The HRPT is small compared to other setups, with a distance of 1.6 cm between the separate layers. Each layer consists of a sensor assembly placed on a Carrier Board (see figure 6.2) that is placed inside a Telescope Card (see figure 6.3). The eight layers are connected to the readout electronics via the Back Plane printed circuit board.

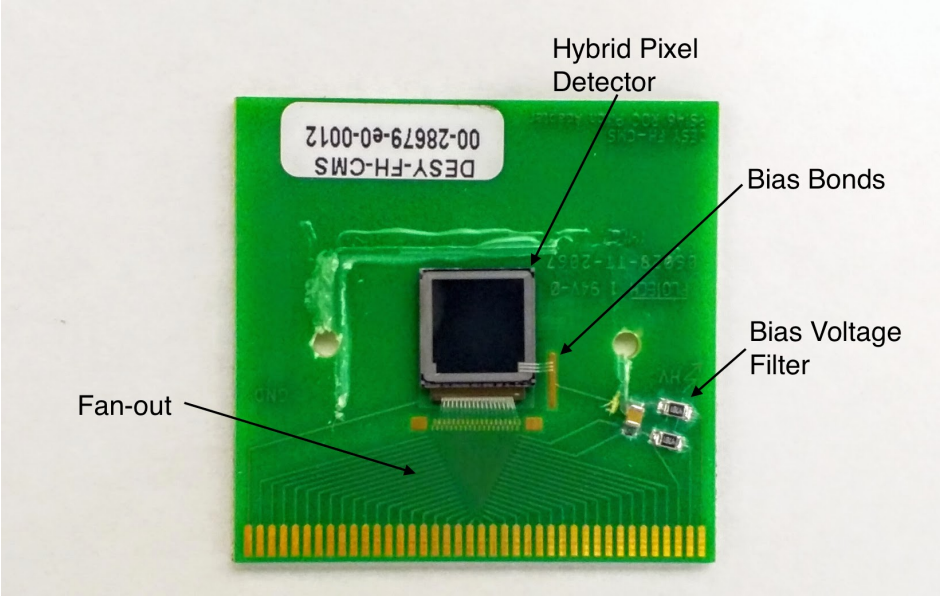

Figure 6.2: **ROC carrier board**
To connect the hybrid pixel detectors to the readout electronics they are glued to the Carrier Boards. The Carrier Boards are small printed circuit boards with a fan-out circuit and a noise filter for the bias voltage line of the silicon sensor. The Carrier Board plugs into the Telescope Card.

was done for all LVDS signals that need to arrive synchronously at the ROCs: clock signal, I^2C [1] control signal and the described CTR signal.

The analogue supply voltage AVDD and the digital supply voltage DVDD to power the readout chips also arrive from the twisted pair cable. They are simply connected in parallel to the different planes of the detector. The high voltage coming through the same cable is also split up and applied in parallel to all sensors.

The only other signal coming from the DAQ system is the readout token. Again a differential LVDS signal, this signal triggers the readout of data from the readout chip as explained in section 4.2. The eight planes are numbered from 0 to 7. Every 26-pin connector has a Token-In and a Token-Out line. The Token-In of plane 0 is connected to the line coming from the DAQ system. After a ROC has finished its readout it will pass the token through the Token-Out line. All eight planes are daisy chained, with the Token-Out line of one plane connected to the Token-In line of the next plane. These lines are kept as short as possible to keep the delay between ROC readouts as small as possible. The Token-Out line of plane seven is equipped by a LVDS signal driver, the *Texas Instruments DS90LV001* chip [Ins15b], to be able to cover the full length of the return path to the DAQ system without a significant decrease in signal quality.

The purpose of the BP is not only the distribution of signals to the telescope planes, but also the merging of the data streams from all eight planes to a single data stream. The LVDS data streams from the telescope planes are in the low-voltage state when the ROC is idle and also when it transmits a zero. Only ones are translated to the high-voltage state, with a voltage swing of 5 V between both states. To merge the data from all ROCs to a single

[1] I^2C: short for **I**nter-**I**ntegrated **C**ircuit, a multi-slave, single-ended, serial bus, used to communicate with integrated circuits such as ASICs or microcontrollers.

(a) **Front** (b) **Back**

Figure 6.3: **Telescope Card**
The Telescope Card holds the Carrier Board on which the pixel sensor is placed on, thus all electrical connections of the sensor to the Back Plane are made through the Telescope Card. Each Telescope Card in a telescope has its unique I^2C address, which identifies the ROC to the control signals coming from the data acquisition system. On the Telescope Card the data output transmitted in an LCDS signal of the PSI46dig readout is translated to an LVDS signal, that is better suited for the long transmission path back to the DAQ system.

stream a series of OR gates are placed on the BP. In the first step the data from a pair of ROCs (ROC 0 and ROC 1, ROC 2 and ROC 3, and so on...) are merged. In a second stage the four remaining data lines are merged to two lines and then the last level of OR-gates brings all data streams to a single line. The *ON Semiconductor NB7L86M* chip [Sem15] was used because of its high data input/output rate of up to 8 Gbit/s. The data is then sent to the DAQ system through the connected flat band cable.

The Telescope Card

The Telescope Cards (TCs) contain the ROC carrier boards and electrically connect the ROCs to the Back Plane where all signals and control voltages are coming from. The I^2C control signals coming from the DAQ system to all ROCs in parallel but are only meant for a single readout chip. Every ROC needs an unique I^2C address. With every control signal this address needs to be sent as well so the correct ROC can respond to it. The I^2C addresses, ranging from 0 to 15, are set by four solder connections on the TC.

The second important feature of the telescope card is the translation of the readout chips data output from LCDS to LVDS. The data output of the PSI46dig is a three-state low current differential signal (LCDS). When the ROC output is in an idle state both lines of the differential signal path carry the same current $I_{DC}/2$. Zeros and Ones are transmitted by sending a current I_{DC} through either of the two lines forming the differential signal line while the other line does not see any current. The sum of currents in both lines at any time is I_{DC}. This method works well for short distance transmission of signals and makes it easy to merge several data streams by connecting several ROCs to the same data transmission line that then can be received by and the readout electronics. For the telescope this way of transmitting data is not suitable since the distances between the ROCs and from the telescope to the readout electronics are much larger than on a pixel module. An asymmetric LCDS to

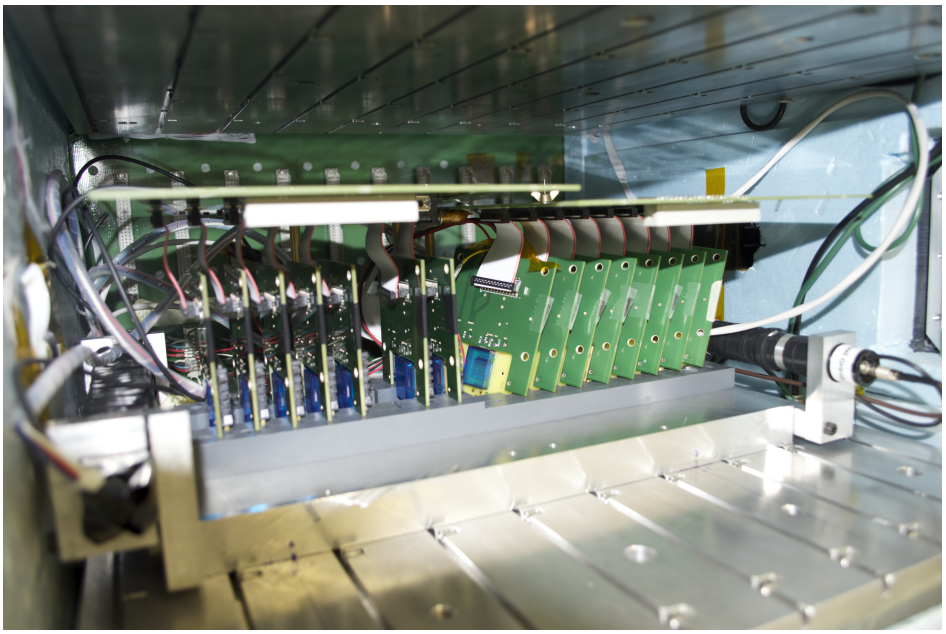

Figure 6.4: **The mechanical setup of the HRBT**
For the High Rate Beam Test (HRBT) two telescope are simultaneously operated. Both telescopes are placed inside of a cooling box with large Peltier cooling blocks on top and bottom to passively cool the sensor and readout chips and keep leakage currents low after irradiation. The telescope seen on the left side is oriented with its detector planes orthogonal to the particle beam. The second telescope on the right has its planes tilted to increase charge sharing in the pixels.

LVDS translator is placed on the TC, using the *Analog Devices ADCMP604* chip [Dev15]. It will translate a current bigger than a threshold value on the first line to a LVDS high-voltage state and all other current situations on the LCDS data line to a LVDS low-voltage state. The LVDS signals have a longer range than LCDS signals and commercial solutions exist for them to be translated and digitised.

All other components on the TC terminate signals arriving at the U-shaped *SAMTEC - MB1* connector in which the readout chip of the telescope plane is placed. The eight connectors for all TCs on the Back Plane are placed with 1.6 cm spacing. To connect the TC with the Back Plane a short flat band cable of ~ 5 cm is used. The cables must not be too long since this would create gaps in the readout due to long token passing times, but at the same time need to be long and flexible enough to be tilted into the final telescope configuration.

The HRPT can only work when all eight planes are equipped with Telescope Cards and a functioning ROC on a carrier board. Since for some tests during the commissioning of the telescope it is not convenient to use eight fully equipped planes, a small Dummy Card was created. It is placed on the 26-pin connector and terminates all arriving signals without creating reflections and passes the token coming from the previous plane of the daisy chain.

Telescope Mechanics and Cooling

In previous high rate test beams it was seen that the current drawn by the sensors increases after being subjected to the direct beam current and the resulting radiation damage [Spa].

The only way to reduce the current is to keep the sensors temperature low. This means the heat produced by the sensors and the readout chips needs to be dissipated. The compact design of the telescope and the need for a minimum of material in the path of the beam made a direct cooling of the sensors impossible. Instead the entire telescope was put into a closed box, the '*Vienna Box*', with a powerful Peltier cooling element [Fri01]. While the cold side of the Peltier element is connected to a massive aluminium block inside the box, the warm side is cooled by a flow of 10 °C water. Although the detectors do not touch the cold mass of the aluminium block, they are sufficiently cooled to prevent thermal run-away of the irradiated sensors, see section 3.4. By constantly flushing the inside of the almost air-tight box with dry nitrogen gas condensation of water from the air and potentially destructive short circuits on the electronics are prevented. In figure 6.4 one can see two High Rate Pixel Telescopes in the Vienna Box.

The mechanical setup placed inside the Vienna Box was designed to hold two telescopes with eight planes each at the same time. The only difference between the two telescopes is the orientation of the sensor planes with respect to the beam direction. The first telescope is perpendicularly oriented to the beam, the angle between the normal vector of incident particles and the sensor plane is $\approx 90°$. The second telescope is tilted in two axes: The sensor planes are tilted by 30 ° in the direction of the columns of the readout chip to simulate the angle in which most of the planes in the CMS Pixel detector are hit. The tilt of 20 ° in the direction of the rows simulates the additional charge sharing by the magnetic field in the CMS detector. The small incident angle of particles on the sensor planes increases charge sharing, see section 3.3.4.

6.2 The HRPT Data Acquisition System

Together with the new High Rate Test Beam a new data acquisition (DAQ) system was conceived. A high particle flux on the detector planes, a possible trigger rate of up to 100 kHz and a data throughput requirement of several tens of megabytes per second presented the biggest challenges for the system. The final system shown in figure 6.5 was designed by the group around *Kristian Harder et al.* from Rutherford Appleton Laboratory in Ditcot, UK.

In this part of the chapter the DAQ system and its functionalities as a combined Front-End Controller/Front-End Driver will be shown.

6.2.1 The SP605 FED/FEC Hybrid

The DAQ system for the High Rate Pixel Telescope is made from a combination of commercially available hardware and a custom designed electronics board. Together with a standard PC this small and low-cost system is sufficient to control the beam telescope hardware explained before and also to collect and save the data from the the High Rate Pixel Telescope. The DAQ system works as a FED/FEC hybrid. This means the general tasks of the Front End Controller (FEC), of programming the detector readout electronics and the supply electronics, and of the Front End Driver (FED), of receiving and decoding the data stream of the detector front end, are combined in a single unit. The FED/FEC hybrid is able to do both of these tasks at the same time.

The commercial *Xilinx SP605* evaluation board [Xil15] equipped with a *Spartan® 6* Field Programmable Gate Array (FPGA) fulfilled most requirements posed on the DAQ system. The FPGA was fast enough to be run at the 320 MHz needed to sample the serial data stream coming from the readout chips. At the same time enough clock resources on the FPGA are

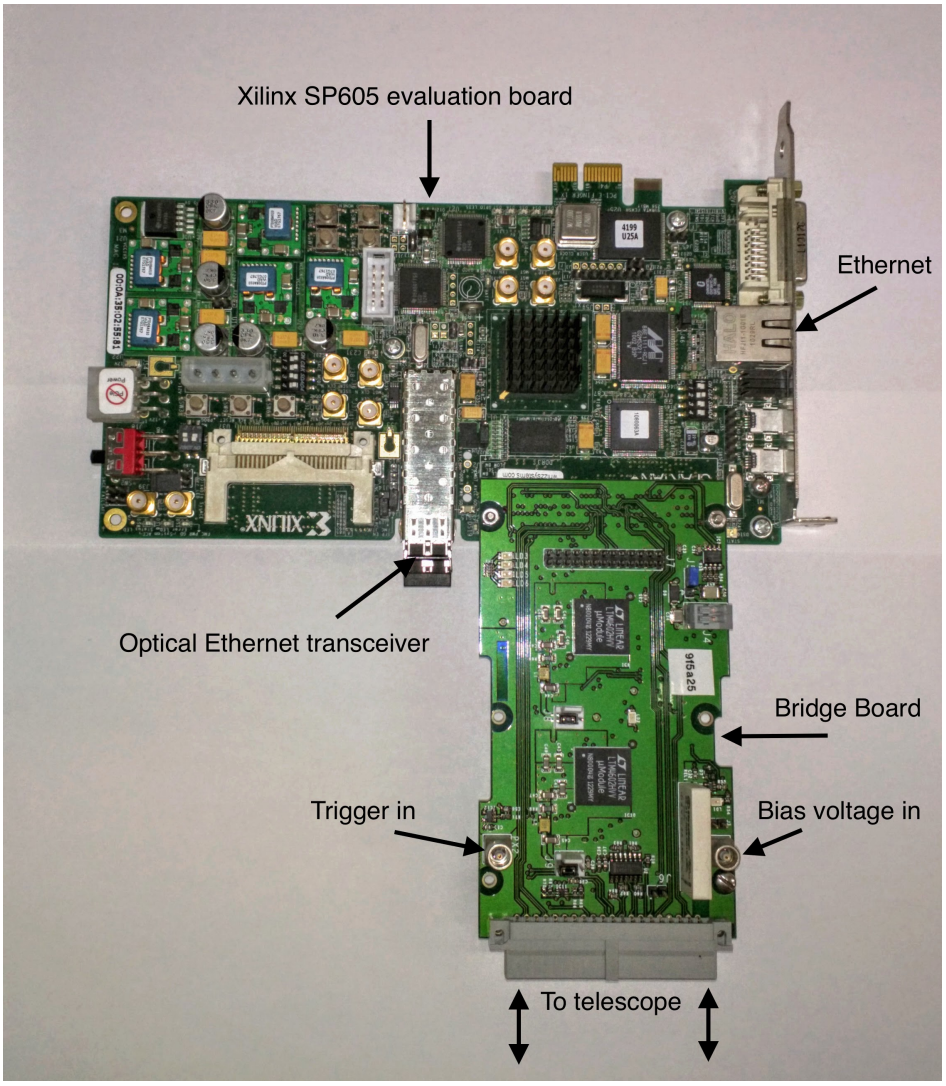

Figure 6.5: **The HRPT Data Acquisition System**
The data acquisition system (DAQ) for the High Rate Pixel Telescope is built from two parts: the commercially available Xilinx SP605 evaluation board and the custom made Bridge Board (see figure 6.6). The Xilinx SP605 runs a Spartan® 6 FPGA that holds the DAQ firmware, sends commands to the ROCs in the telescope and decodes the event data coming from the telescope. The connection to the DAQ PC can me made through optical or conventional Ethernet. All connections to the telescope are made through the Bridge Board.

available to operate most processes at the 40 MHz LHC clock. A quartz oscillator on the SP605 board was used as internal clock source.
The board also had several high speed network connections to either transfer data to disk or to receive commands from. One could choose to either use 10Gbits^{-1} Ethernet over optical fibre or a regular cable. Depending on the use case and a potentially long distance between control PC and the DAQ electronics the option of optical fibre communication was very useful. The transfer rates of both operation modes are high enough for the HRPT.

To connect the SP605 board to the telescope a custom board was designed, the *Bridge Board* (BB). The BB acts as an interface card between the FED/FEC hybrid and the telescope and controls the power supplied to the telescope. The main components of the BB are the FMC (FPGA Mezzanine Card) connector to the SP605 board and the 40-pin SEMTEC connector for the connection to the telescope. Two low voltage power supplies are mounted on the board and provide the analogue and digital supply voltage for the readout chip in the HRPT. The power supplies are controlled from the SP605 board. A LEMO connector is used to connect the DAQ system to the trigger logic. The incoming TTL trigger signal is routed from the BB to the FPGA on the SP605 board, where it is processed.

The high voltage for the sensors is also connected through the Bridge Board. With a controllable relay the HV can be turned on and off remotely.

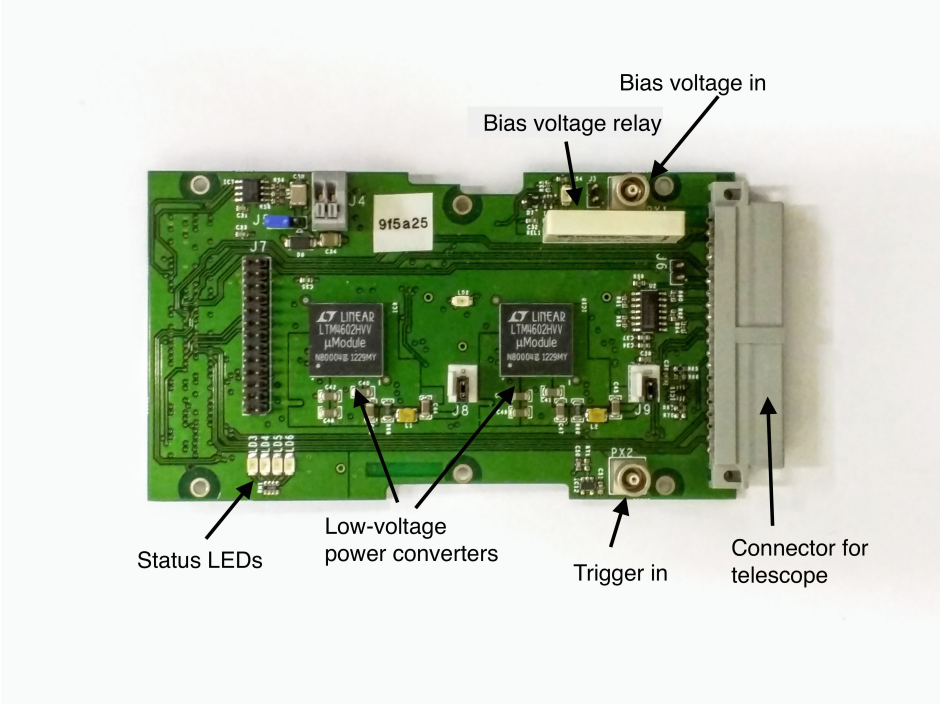

Figure 6.6: **The Bridge Board**
The Bridge Board is a custom made PCB that interfaces the Xilinx SP605 board with the telescope. Two low-voltage power converters are placed on the Bridge Board to provide two different voltages to the readout chips. The Bridge Board hold the input connector for trigger signals and the bias voltage for the silicon sensors.

6.2.2 Testboard Capabilities

The DAQ system, consisting of the SP605 board and the Bridge Board, is generally referred to as the 'Testboard'. The Testboard is controlled by using the IPBus software and firmware package [L+15]. IPBus is an IP-based hardware control protocol developed for the CMS Trigger upgrade by a collaboration of the University of Bristol and Imperial College London. The IPBus protocol describes the basic read and write interactions to control a piece of hardware. All commands, sent to the Testboard via Ethernet, are collected in a C++ based Hardware Access Library (HAL) *μHAL*. On top of the μHAL layer a calibration and data acquisition software package was written.

By using configuration files that control all possible variables loaded into the Testboard it is ensured the DAQ system is in a functional stage after powering it on. Depending on the operation mode, either calibrations or data taking, different settings were chosen. In calibration mode the Testboard ignores external triggers from the trigger signal input on the Bridge Board. All trigger signals are created and fully controlled from the Testboard. The most important configuration parameters are described here:

External Clock `ctrl.externalClk`
: The Testboard can run either on an external clock or on the 25 ns clock provided by the test board. This boolean switch decides upon loading of the calibration file which clock is being used.

External Triggers `trig_ctrl.enableTriggers`
: This boolean switch determines if external triggers from the input LEMO connector on the Bridge Board are received by the Testboard and then relayed to the telescope. During calibration runs this switch was off, to prevent accidental external triggers affecting the measurements that heavily rely on counting triggers and responses from the sensor planes. When running the Testboard to take beam test data, this switch is on. Triggers from the QIE device are accepted and relayed.

Trigger stacking `trig_patt.max_stack`
: The new PSI46dig readout chip allows to stack up to 16 triggered events. Several triggered events can be kept in a buffer on the readout chip and then successively read out. This parameter defines how many triggers are stacked on the Testboard side.

Trigger pattern `patt_ctrl_0, patt_ctrl_1` **and** `trig_patt.patt_ratio`
: The correct trigger pattern is crucial for the operation of the High Rate Beam Telescope. It controls the sequence of signals that are sent to all readout chips in parallel via the CTR line. Three signals can be send: calibrate, trigger and reset. The trigger pattern is built from a eight digits long hexadecimal number, for example `0x903772d4`. Separated into groups of two numbers, four slots for different signals exist. The hexadecimal number in each slot defines the signal and a waiting time following the signal. With the first two most significant bits C_{MSB} defining the length of the signal the six least significant bits define the length of the delay in clock cycles measured from the beginning of the pulse. The different signals controlled by C_{MSB} are:

- No signal: $C_{\mathrm{MSB}} = 0$,
- Calibrate pulse: $C_{\mathrm{MSB}} = 1$,
- Trigger: $C_{\mathrm{MSB}} = 2$,
- Reset: $C_{\mathrm{MSB}} = 3$,

The delay time for each slot is up to 63 clock cycles. For longer delay times an additional slot without signal has to be used

Two different patterns can be programmed into the Testboard, `patt_ctrl_0` and `patt_ctrl_1`. This was done to be able to send periodic resets during data taking. When the register `trig_patt.patt_ratio` is set to a value of $N \neq 0$, every N^{th} trigger will be of the second pattern.

Data Phase `ctrl.dataPhase`
When the binary data stream from the eight ROCs in the telescope reaches the Testboard, it is deserialised and transmitted to the PC controlling the Testboard. With the dataPhase switch it is possible to choose between two possible phase settings of the arriving data. This phase has to set correctly to decode the data stream.

Data Headers `ro_hdr_a, ro_hdr_b` **and** `ram_hdr_b`
The deserialised data received from the telescope is sent back to the computer as single events. To be able to distinguish between them, each event starts with the event header `0xffffffff` followed by information about the event, like time stamp and event number. After the marker word `0xdeadbeef` the deserialised ROC hit information follows.

Analogue and Digital Voltage `AVDD&DVDD` **and Max. Output Currents** `MaxIAVDD` **&** `MaxIDVDD`
As described the Bridge Board houses the low voltage power converters that supply all eight ROCs of a telescope with analogue and digital voltage. The voltage settings are read from the configuration file when the Testboard is being programmed. The voltage value is given in units of mV. The maximal output currents are regulated as well and given in units of mA.

One of the most important tasks for the Testboard is the configuration of all PSI46dig readout chips that are connected to the telescope. Like for the Testboard itself a single configuration file exists for each of the telescope planes. The Testboard can program these the stored individual settings for every ROC by sending I^2C commands to the telescope. With every telescope plane having its unique I^2C address, only the addressed ROC receives the settings, while the other ROCs ignore them.

The Testboard designed by RAL is low in cost, since its logic part is make from a commercially available circuit board with only a small custom made extension PCB. The use of the already existing and well maintained μHAL framework reduced the workload on implementing our own hardware access layer and provides a large bandwidth for data transmission between Testboard and control PC during data taking. Yet the use of μHAL also has its disadvantages. The transmission of a single command from the controlling PC to the Testboard is always executed as a single interaction. When running calibrations on the ROCs, where every single trigger signal needs to be given separately the time to communicate the command to the Testboard via IPBus takes up most of the time.

6.3 Fermilab Test Beam Facility

Choosing the correct beam environment for testing high energy particle physics detectors is an important part of the experiment. The biggest problem for the High Rate Beam Test was to find a beam line that would supply a sufficiently high flux of high energy particles. With the LHC and all of its pre-accelerators at CERN performing maintenance work in 2013/14, the only beam line suitable was the newly commissioned High Rate Tracking Area

of the Fermilab Test Beam Facility (FTBF). The beam line is designed for small and compact experiments with little material in the particle beam. The High Rate Pixel Telescope was the first experiment ever installed in the new beam line at Fermilab, which entailed the problems of using an unknown and untested beam in a completely new beam area. Nevertheless, to make the experiment of measuring the high rate capabilities of the PSI46dig chip possible, an effort was made to measure and control the occurring beam conditions.

6.3.1 Test Beam Structure and Beam Parameters

The High Rate Tracking Area is part of the *MTest* beam line at Fermilab. The primary beam in the beam line is a direct extraction from the Main Injector and contains protons with energies of 120 GeV. On their way to the MTest beam line the protons travel through a series of pre-accelerators. In the Linac the protons are brought to an energy of 400 MeV and then injected to the Booster. The Booster captures the protons into batches of 84 bunches and accelerates them to 8 GeV [FNA15]. With a revolution time of 11.13 µs a maximum of seven batches fit into the Main Injector. Finally the Main Injector accelerates the protons to 120 GeV with a bunch time spacing of 18.3 ns. About every 60 seconds the Main Injector beam is partially extracted to the MTest beam line. One extraction corresponds to exactly 369000 turns of the Main Injector, so the beam 'spill' has a duration of 4.2 s. In figure 6.7 a profile of the beam intensity of every bucket in a spill is shown. In this spill only five of the seven Booster batches are filled with particles, two batches are empty. Between two filled batches the intensity drops as several bunches are not filled. The bunch-by-bunch beam intensity was measured using the QIE device explained later in this chapter, see section 6.3.2.

The MTest beam line can be operated in two different modes: The first is the direct unattenuated proton beam extraction from the Main Injector, the second is a low rate pion beam with an energy range of 8 - 66 GeV. A time profile of the primary proton beam mode with a beam energy of 120 GeV is shown in figure 6.7. This beam mode was also used during the beam test if not stated otherwise.

The 18.3 ns bunch spacing of the Main Injector extraction is actually a disadvantage for the High Rate Beam Test. As already explained the readout electronics of the High Rate Pixel Telescope runs on the nominal 25 ns clock of the LHC. This clock is also distributed to the PSI46dig readout chips used in the detector planes of the telescope. This results in a constantly changing phase between the clock of the readout chips and the Main Injector. It was not possible to lock the clock of the readout electronics to the clock of the Main Injector due to the change in clock frequency during the energy ramp.

6.3.2 Rate Measurement and External Telescope Trigger

Measuring the rate of particles delivered by the test beam is important for the beam test performed with the High Rate Pixel Telescope. Several devices to measure the absolute number of particles in the beam and to measure the shape of the beam are already installed in the beam line used for the experiment. To exactly quantify the number of particles traversing the telescope at any time during a 4 s beam extraction from the Fermilab Main Injector a measurement device with a much better time resolution is needed. For the High Rate Test Beam a combination of a small scintillator, connected to a photomultiplier tube (PMT) and a readout system called the Charge Integrator and Encoder (QIE) [Ye92] was conceived. This system is able to deliver a measurement of the charge deposited in the small scintillator cube during a 18.8 ns interval, the length of a bunch, or bucket, of the Fermilab

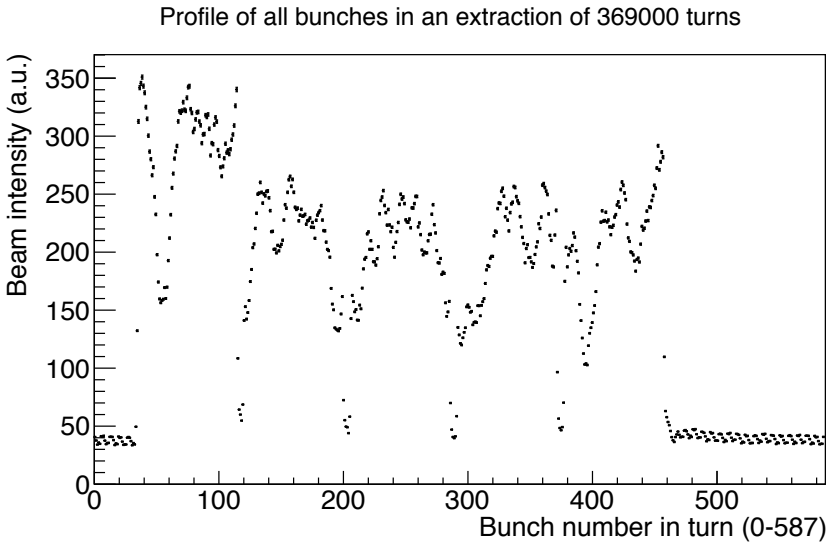

Figure 6.7: **Profile of the filled bunches in a Main Injector extraction measured by the QIE device**
Each recorded beam extraction from the Fermilab Main Injector, or spill, is made of 369,000 Main Injector turns. In each turn particles from the 588 bunches in the Main Injector are extracted to the beam line. The number of particles in each bunch was measured using the QIE device. The figure shows the profile of the turns for each bunch. Not all bunches are filled with particles. The plot shows the case with five filled batches. At any time no more than six filled batches were in the Main Injector during the High Rate Beam Test.

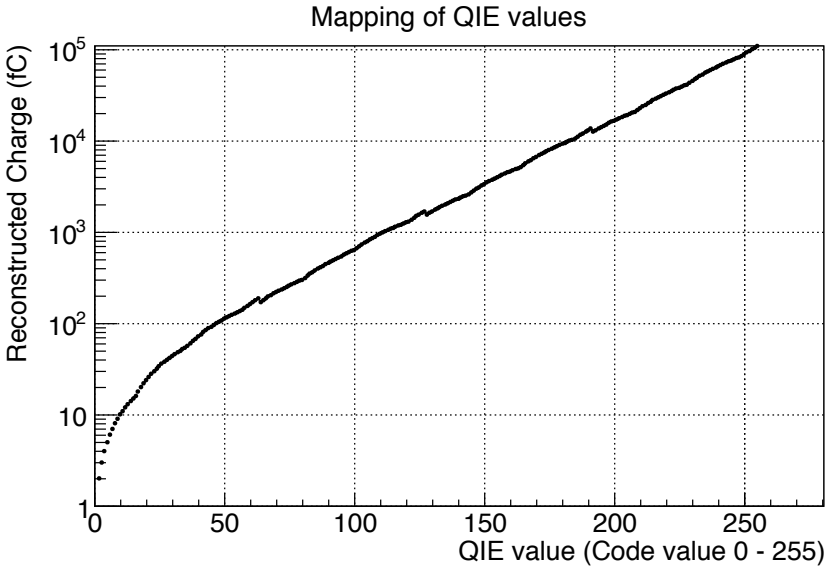

Figure 6.8: **Mapping of QIE values and reconstructed charge**
The Charge Integrator and Encoder (QIE) is used to measure the beam rate. The QIE integrates and measures the charge created by the output of a photomultiplier connected to a small scintillator crystal placed in the beam path. The saved ADC values from the QIE output can be translated again to a measured charge using the shown mapping. The QIE is characterised by its nonlinear response to charges and its high time resolution.

Main Injector at full energy of 120 GeV, in the small scintillator cube. The charge measured by the QIE can be converted to a measurement of particles passing though the scintillator.

QIE Beam Monitor

The Charge Integrator and Encoder (QIE) itself is an ADC with a high time resolution and a high dynamic range. It was developed to read out the signals created in the scintillator tiles of the CMS hadron calorimeter, but is also used in other experiments like SeaQuest at Fermilab. For the High Rate Test Beam the system of scintillator, photomultiplier and QIE readout was provided by Fermilab. The scintillator and photomultiplier tube are placed outside of the cooling box, yet the scintillator, with a front surface of 1 cm × 1 cm, is aligned with the telescope. The amount of light created in the scintillator is converted to an electrical signal and amplified by the photomultiplier tube running at −1000 V. The QIE integrates the charge collected from the signal over a time of 18.8 ns from the PMT and digitises the value. To achieve a large dynamic range in the charge measurement, the conversion is not linear but logarithmic, as can be seen in the plotted mapping between the QIE value and reconstructed charge in figure 6.8. Most notably in the conversion is that for certain values in the range of the QIE flash ADC the reconstructed charges overlap.

The QIE setup is read out via Ethernet and the collected data is saved as a single file for every 4 s beam extraction with a single measurement for every 18.8 ns bucket. Each bucket is associated with a QIE value between 0 and 255. By applying the QIE mapping shown in figure 6.8 the charge measured for every bucket is reconstructed.

Trigger Modes

The QIE is not only used as a means to survey the beam, but also as an external trigger signal for the High Rate Pixel Telescope. The QIE's capability to count every 18.3 ns long bunch of particles coming from the Main Injector makes it possible to trigger at exactly the same time during each Main Injector turn of an extraction. The QIE was configured to send a single trigger during a Main Injector turn. With this the HRPT receives a trigger rate of

$$\frac{1}{11.13\,\text{ns}} = 88.5\,\text{kHz}. \tag{6.1}$$

With a design maximum of 100 kHz for the readout of the pixel detector of the CMS experiment the beam telescope was running close to its limit.

The programmable trigger was set on different bunches during the measurement campaign to reflect different possibilities of filling and possibly overflowing the ROC's data or time stamp buffers. The readout was triggered early during a turn, bunch 50 was triggered on. With at least one empty Booster batch before, for this early trigger bucket the ROC buffers should be relatively empty and the measured inefficiencies all result from later hits. When triggering on bunch 270 of the turn, the measured inefficiencies are influenced by the particles passing the detector planes in a time window before and after the triggered on tracks occurred. Lastly, when triggering on bunch 520 the gap of 84 empty bunches occurs after the event triggered on occurred.

6.4 Fermilab Test Beam Measurement Programm

The 2014 Fermilab test beam was scheduled to be two week long with beam time from 7:00pm in the evening to 7:00 am in the morning. Although the parameter space of possible trigger points and WBC settings was large, the full measurement program was executed during two days of beam time. Beging able to operate two High Rate Pixel Telescope setups at the same time proved to be a big advantage. During data taking a minimal shift crew of two people was required at any given time to monitor the sensor bias voltages and bias currents, the cold box temperature and dry gas supply and to change data taking parameters.

The full measurement program looked as follows. For both telescopes, the orthogonal and the tilted one, data was taken at three different trigger positions within the 11 µs Main Injector turn. The three different bunches triggered on were bunch 50, bunch 270 and bunch 520. They are distributed early, centred and late in each turn with 588 bunches. Additionally the internal latency of the readout chips WBC was varied. The setting of WBC has a big influence on the ROC's readout efficiency. With the current setting of WBC in the CMS experiment at 159 **I need a reference** all values were chosen to be around this value. The values 140, 159,175 and 200 were always tested. Only in few runs the very small value of WBC 99 was used. A summary of the different settings of the measurement program can be see in table 6.1. In the table the first spill number and the last spill number with the same triggered on bucket are listed.

6.5 Conclusions

With the High Rate Pixel Telescope a novel beam telescope has been designed that is able to cope with the highest beam intensities at the current maximal trigger frequency of the CMS experiment. The telescope is portable and can even be used in very small beam enclosures.

Table 6.1: **Measurement Program Fermilab 2014 Test Beam**

		WBC settings	
Spill range	Trigger bucket	Orthogonal telescope	Tilted telescope
175252 to 175595	270	telescope was out	140, 159, 175, 200
176422 to 176656	270	140, 159, 175, 200	140, 159, 175, 200
176658 to 176998	520	99, 140, 159, 175	99, 140, 159, 175
179410 to 179620	50	140, 159, 175	140, 159, 175, 200

The readout and control electronics are combined in a single electronics board. Most parts are commercially available and low-cost compared to other telescope systems.

The High Rate Pixel Telescope is the first experiment to be installed and use the High Rate Tracking Area at the M3 beam line at Fermilab. This beam is the only particle beam world wide that makes it possible to test new detector systems under the extreme conditions they will be subjected to in a high energy particle physics experiment in the LHC era and beyond.

The QIE device makes it possible to measure the beam rate on a bunch-by-bunch basis. For each 18.3 ns bunch the number of protons passing through a small scintillator cube, positioned in front of the beam telescopes, are measured.

The following chapter will contain the measurements done at Fermilab and their interpretation using a full simulation of the beam test.

Chapter 7

Beam Test Data Analyis

7.1 EUTelescope and ILCsoft – The Analysis Framework

To reduce the workload in setting up a full analysis chain for the collected data from the High Rate Beam Test, it was decided to adapt the already existing *EUTelescope* framework for the needs of this experiment. The EUTelescope framework is a full-featured beam test analysis software package developed for the EUDET project, supported by the European Union in its sixth Framework Progamm for the European Research Area. EUTelescope was originally designed to process the data from the EUDET telescopes. They are a series of identical particle tracking telescopes, based on the Mimosa26 readout chip, with an intrinsic resolution of $\approx 4\,\mu m$ [Rub12]. The EUDET telescopes are designed to accommodate a large variety of detectors as the Device Under Test (DUT). The EUTelescope software is embedded into the ILCsoft framework that is being developed for the *International Linear Collider (ILC)* project, a possible future high energy particle physics experiment. The most distinctive features of the ILCsoft framework are the LCIO (Linear Collider I/O) event data format, the GEAR (Geometry API for Reconstruction) markup language to describe the telescope geometry and the event processor Marlin (Modular Analysis & Reconstruction for the LINear collider).

Marlin

Every step in the EUTelescope data analysis chain is implemented as an independent processor. This allows for a highly modular configuration of the analysis fit to the specific use case. Every processor is controlled by a 'steering file', written in XML format, that is loaded at runtime and exposes various parameters to the user. EUTelescope provides all the necessary processors for a full reconstruction of beam test data, like raw data conversion or cluster finding, that are executed in sequence by Marlin. The implementation of EUTelescope in the LHCsoft package makes it also possible to send larger analysis Marlin jobs to be executed on the Worldwide LHC Computing Grid (Grid).

In figure 7.1 the general layout of the EUTelescope analysis chain is sketched out. While some processors and input containers were not needed for the High Rate Beam Test analysis (greyed out elements), others have to be implemented by the user (elements with dashed outline).

The LCIO data format

The LCIO persistency data model was designed as a file format to be used by the different groups involved in the design and simulation of the ILC. A common persistency format, usable by Java, C++ and Fortran applications made it easier to share and compare results and algorithms between the different groups and avoids duplication of effort. The interface

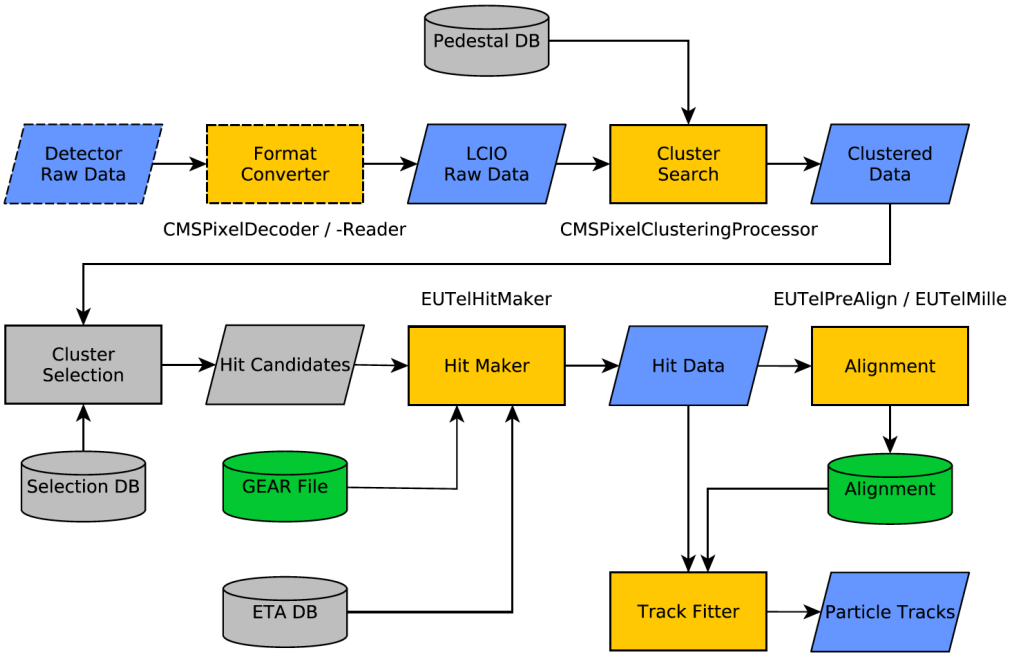

Figure 7.1: **Schematic of the EUTelescope Framework**[Spa]
The concept of the EUTelescope analysis framework is sketched here. The yellow rectangles represent the data processors. While some of them are provided by the EUTelescope software (solid border), others have to be implemented by the user (dashed border). The blue rhombs represent the persistent data containers. The green cylinders are external input parameters like the alignment constants and the telescope geometry. The greyed out functionalities are not used for the High Rate Beam Test analysis.

provided for the different programming languages is abstract and hides the implementation of the data storage mechanism from the user code. This allows the underlying data format can be changed without forcing the user to make non-trivial changes to his other code and it allows an easy integration into new projects without concerning about the data format.

The LCIO data format is event based. All information belonging to a single trigger, be it created in a simulation or a beam test experiment, is stored under the same event number. The following shows the printed overview information of a single event in the High Rate Pixel Telescope in the LCIO data file after the full data analysis chain has been executed on a set of simulated data for the High Rate Beam Test (see chapter 8).

```
////////////////////////////////////
EVENT: 3739
RUN: 1
DETECTOR: CMSPixelTelescope
COLLECTIONS: (see below)
////////////////////////////////////


--------------------------------------------------------------------------
COLLECTION NAME               COLLECTION TYPE          NUMBER OF ELEMENTS
==========================================================================
alignedhits                   TrackerHit                       16
cluster                       TrackerPulse                     16
corrfithits                   TrackerHit                       14
fithits                       TrackerHit                       16
fittracks                     Track                             2
hits                          TrackerHit                       16
original_zsdata               TrackerData                      16
prealignedhits                TrackerHit                       16
sparse                        TrackerData                       8
--------------------------------------------------------------------------
```

Each stored event begins with a header containing the run and event number. Also the name of the detector from which the data originates is saved. Not visible in this display is the time stamp that is also saved for every hit. Data is stored in different collections. During each step of the analysis chain a specific collection is analysed and a different one populated. By labelling every data entry in the collections with a unique hexadecimal ID, the different collection entries can be cross-referenced. This way it is possible to link all information connected to a reconstructed track, down to the original single pixel hits.

The Telescope Geometry

The Geometry API for Reconstruction (GEAR) markup language makes it possible to describe different telescope and detector geometries for the reconstruction algorithms of the EUTelescope framework. The GEAR file describes a simplified version of the detector geometry by restricting the system to only the parameters that are necessary for track reconstruction. The file contains information about the pixel pitches and the distances between telescope planes. All reconstruction algorithms take these information at runtime from the file, which makes it possible to quickly switch between different detector geometries by loading different files. The GEAR file itself is structured using XML markups. The hierarchical structure of the file begins with a general description of the detector with its name and the parameters for a possible magnetic field. Then each telescope plane, or `layer`, is described by its position, size, rotation and radiation length of the sensor material. Additionally the number of pixels and their pitches are defined. This makes it possible to mix different detector types in

the same telescope, which is interesting for all telescope applications for which the DUT is different from the telescope planes.

As an example an excerpt of the GEAR file of the straight telescope is given here.

```
<gear>
  <global detectorName="CMSPixelTelescope" />
  <BField type="ConstantBField" x="0.0" y="0.0" z=".0"/>
   <detectors>
    <detector name="SiPlanes" geartype="SiPlanesParameters">
      <siplanesID ID="0" />
      <siplanesType type="TelescopeWithoutDUT" />
      <siplanesNumber number="8" />
      <layers>
        <layer>
          <ladder ID="0" positionX="0." positionY="0." positionZ="16.0"
           sizeX="7.8" sizeY="8.0" rotationZY="0." rotationZX="0."
           rotationXY="0.0" thickness="0.285" radLength="93.660734" />
          <sensitive ID="0" positionX="0." positionY="0." positionZ="16.0"
           rotation1="1" rotation2="0" rotation3="0" rotation4="1"
           sizeX="7.8" sizeY="8.0" thickness="0.285" npixelX="52"
           npixelY="80" pitchX="0.15" pitchY="0.1" resolution="0.100"
           radLength="93.660734" />
        </layer>
      </layers>
    </detector>
  </detectors>
</gear>
```

7.2 The Data Analysis Chain

As already described in the previous section, the EUTelescope data analysis framework is a set of Marlin processors that are executed in sequence to create high level track objects from the raw data that was created in a beam test measurement or a simulation. The following part of this work is dedicated to describing the sequence and the functionality of each processor used for the data analysis of the 2014 Fermilab beam test. The general way this is done is as follows: The raw data saved as a binary file has to be decoded and saved to the LCIO data format so it can be used by the following processing steps. The `clustering` processor scans through all events of the converted data file and find groups of neighbouring hit pixels, a so called cluster. From the list of clusters the `hitmaker` creates a single particle hit point for each cluster. The `alignment` is used to correct for shifts and rotations in the separate telescope planes. After the correction of the alignment algorithm has been applied to the hits, the `tracking` processor find the tracks with hits in all tracking planes of the telescope. These tracks can then be used in the final analysis part to determine the efficiency of the DUT for a varying particle hit rate on the telescope.

7.2.1 Decoding

The first step of creating tracks from the beam test measurements is the decoding of the raw data files and the conversion into the aforementioned LCIO data format. The data format of the PSI46dig readout chip has already been discussed in section 4.2.2. To decode the collected data a standalone C++ library, the *CMSPixelDecoder* was written. A detailed description of the software is given in [Spa] and only the most important details are summarised here.

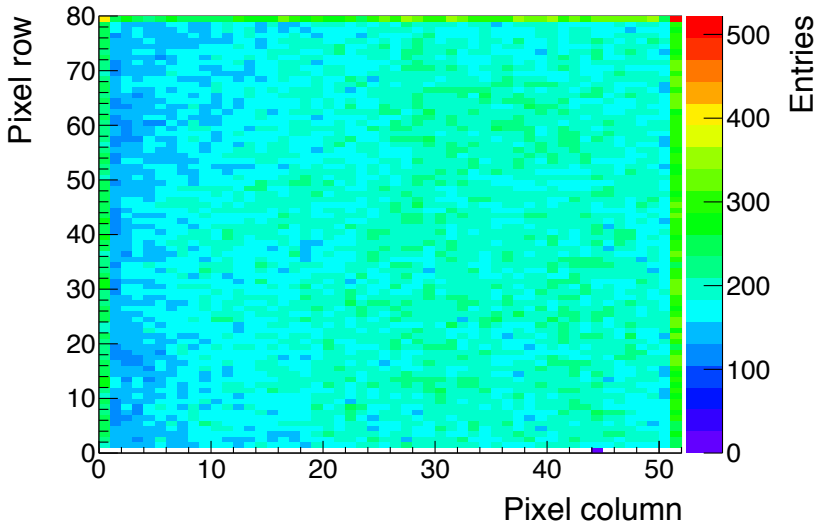

Figure 7.2: **Pixel Hit Distribution on all ROCs for RUN176424**
The pixel hit distribution is created in the decoding step of the data analysis. The distribution over the detector is not uniform since the beam was not defocused enough to cover the full ROC uniformly. The Gaussian beam shape can be seen. The border pixels show more pixels hits because they are double in size compared to the central pixels. The top left and top right corner pixels are four times larger than the central pixels, hence see four times the number of hits.

The CMSPixelDecoder is able to process different types of data. The received pixel information can either be from the former analogue readout chip PSI46v2 (see section 4.1) or from the new PSI46dig (see section 4.2). The decoder is also able to process the data collected either by the High Rate Pixel Telescope readout electronics or a different readout system designed by the group around Roland Horisberger from the Paul Scherrer Institut, Villigen, Switzerland. The decoder can handle any number of ROCs or full modules in the readout chain. After the data has been decoded from the binary data file, it is saved in a separate step in the LCIO persistent data format to be further processed.

7.2.2 Clustering

After the raw data has been decoded and prepared to be handled by the Marlin processors, the next step in the analysis is the clustering of single pixel hits. When a charged particle passes a tracking detector, be it a silicon sensor or any other tracking device, chances are that several readout channels respond to the same particle. By grouping the information from these channels together a *cluster* is formed. In many experiments the detector geometry is designed to create clusters of multiple channels to increase spatial resolution (see section 3.3.4) and hit detection efficiency.

Since the read out from the PSI46dig chip is zero-suppressed, a sparse clustering algorithm is used to define clusters. Sparse clustering means that all pixels activated in an event that are direct neighbours to each other belong to the same cluster. This can create clusters of many different shapes and sizes, what can again be used to study the behaviour of sensors in a magnetic field or tilted towards the incident particle beam. It has to be noted that this type

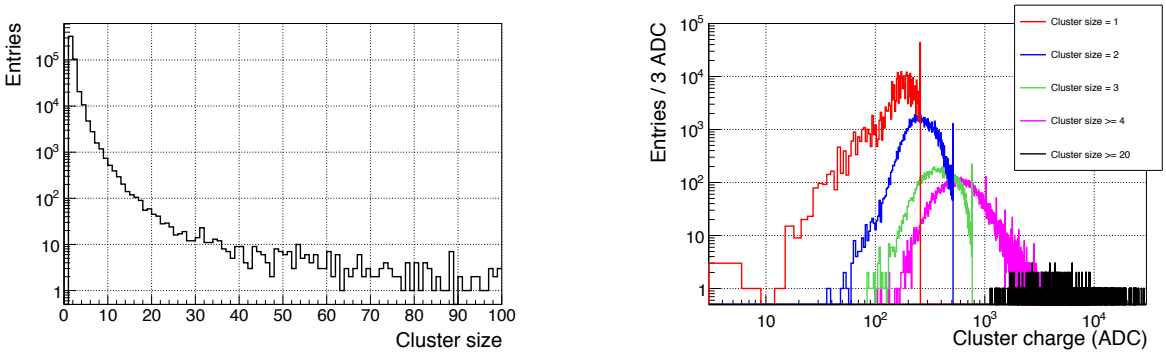

(a) **Cluster Size Distribution** (b) **Cluster Charge Distribution**

Figure 7.3: **Clustering Processor Step**
In the clustering step of the data analysis, neighbouring hit pixels in the same event are grouped into clusters. The cluster size distribution shown in (a) can be measured. Additionally the accumulated charge of the clusters shown in (b) can be studied.

of clustering algorithm also has a downside, which is cluster merging. When a detector is operated in a high occupancy environment, and many clusters are created in the same event on the detector, it can happen that two or more clusters are unwantedly merged. If this is the case the sensor design or channel threshold must be changed to regain the possibility to resolve all particle passages again.

In the data analysis framework used for the High Rate Beam Test the *CMSPixelClusteringProcessor* was used to form clusters from the separate pixel hits read out by the detector planes. This processor is based on the APIXClusteringProcessor developed by the ATLAS collaboration, augmented by some additional functionality like *hot pixel* handling and additional output histograms. A hot pixel is a pixel that is continuously firing signals, due to high noise or a low threshold, and needs to be excluded from the data processing. These hot pixels are identified automatically in the CMSPixelClusteringProcessor and consequently removed from the input pixel collection.

In the output collection every cluster has its own unique ID, with the separate pixel it is made from associated to it. With each cluster information such as the number of pixels it contains, the cluster size, the extension of the cluster in both axis of the pixel detector, and the accumulated cluster charge are saved. The cluster size distribution and cluster charge distribution of the events recorded in a run of the High Rate Beam Test are shown in figure 7.3.

7.2.3 Hit position

From each cluster found in the previous step the incident point of the charged particle on the pixel sensor, the *hit position* or simply *hit*, has to be determined. In order to do so the *CMSTelHitMaker* processor uses the centre-of-gravity method algorithm described in section 3.3.5. By using the pulse height information of each pixel in a cluster the hit position can be determined with higher precision. For single pixel clusters this method does not improve the detector resolution.

The input for this processor are the clusters with only the pixel addresses in row and column and the telescope plane on which they occurred. By applying the information stored

in the GEAR file about the geometry of the High Rate Pixel Telescope the output collection of the CMSTelHitMaker are three-dimensional coordinates in the global telescope frame of reference.

7.2.4 Alignment

The mechanical precision with which a detector can be built is limited by its design and manufacturing process. For a tracking detector with several layers this means that all planes are mechanically displaced with respect to each other and potentially not in the position one would expect them to be. The data gathered from the detector needs to be corrected for these manufacturing imperfections, it needs to be *aligned*, to obtain the highest spatial resolution possible.

The alignment in most detector system is based on tracks. In a first step track candidates, a series of hits on several telescope planes, are formed. This track candidate can be used to calculate the residual, the distance between the measured hit position and the fitted track position on the detector plane, for every hit. By translating and rotating the sensor planes the χ^2 value calculated from all residuals of a track is then minimised, e.g. the distances between measured hits and fitted hits are minimised. Track based alignment has a higher precision than other alignment methods.

In the EUTelescope framework the tracking is split into two steps. The pre-alignment step is performed together with the previously described hit maker. The pre-alignment processor *EUTelPreAlign* only takes care of translations in the x- and y-directions, while shifts of the planes in z-direction or rotations are omitted entirely. The rough pre-alignment is then applied to the hits created by the HitMaker. In a second step the full alignment is performed. It has to be assured that only good tracks are used for the alignment process. By applying cuts on the computed residuals of the track candidate's hits and by only using track candidates that show a high correlation between separate planes of the telescope the number of fake tracks from random hits is reduced. The track candidates that pass the requirements are collected by the *EUTelMille* processor and then fed to the Millepede II algorithm[Blo07]. While keeping the first and last plane of the telescope fixed to suppress weak modes[1] of the alignment algorithm, the other planes and the hits on them are shifted and rotated to minimise the χ^2. The alignment constants for all telescope planes are saved and can be applied to different measurements runs of the High Rate Pixel Telescope data, assuming the displacement between the planes did not change.

7.2.5 Tracking

The last step in the data processing using the EUTelescope framework, and for all particle beam telescope experiments in general, is the identification of particle trajectories in the measured data. The hit positions found in the previous steps are processed by a track finding algorithm and for each found track a set of parameters describing it is created. The parameters describing a track, assuming the z coordinate points along the telescope axis, are:

- the transverse coordinates x_0 and y_0 at the reference coordinate z_0,
- the track slopes $t_x = \tan\theta_x$ and $t_y = \tan\theta_y$ in the xz and yz plane,

[1] Weak modes in the alignment appear when degrees of freedom are weakly defined. They appear often in simple, symmetrical detector geometries like the beam telescope at hand. A typical weak mode is a constant shift of all sensor planes that does not affect the global χ^2 value.

- and the signed inverse particle momentum Q/p.

The method used to find tracks in the data collected by the High Rate Beam Telescope is a so called *Least Square Estimation*. This global track fitting algorithm calculates the sum of the squared differences between measured hit points and reconstructed track point, the χ^2 value. To fit the particle trajectory χ^2 is minimised [Man04]:

$$\chi^2 = \sum_i \frac{\left(m_i - f_{\vec{\lambda}}(l_i)\right)^2}{\sigma_i^2} \stackrel{!}{=} \min . \tag{7.1}$$

In this equation m_i describes a single measurement done by the telescope and track model $f_{\vec{\lambda}}(l_i)$, which analytically describes the path of the particle. Here $\vec{\lambda}$ is the set of parameters describing the track. In the case of a linear model, e.g.

$$\vec{f} = \frac{\partial f}{\partial \vec{\lambda}} \vec{\lambda} = \mathbf{F}\vec{\lambda}, \tag{7.2}$$

equation 7.1 can be solved analytically to obtain the estimated parameters from the measurements to

$$\vec{\lambda} = \left(\mathbf{F}^T \mathbf{V}^{-1} \mathbf{F}\right)^{-1} \mathbf{F}^T \mathbf{V}^{-1} \vec{m}, \tag{7.3}$$

where $\mathbf{V}$ is the diagonal covarriance matrix of the measurements $\mathbf{V} = \mathrm{diag}\{\sigma_i^2\}$, assuming the measurements are uncorrelated. To calculate the parameter pulls the covariance matrix of the parameters $\mathbf{C}_\lambda = \mathrm{cov}(\vec{\lambda})$ is needed

$$\mathbf{C}_\lambda = \left(\mathbf{F}^T \mathbf{V}^{-1} \mathbf{F}\right)^{-1} . \tag{7.4}$$

The least square approach to track fitting is optimally used in cases where the hit occupancy on the detector planes is low. With multiple combinations of possible tracks the tracking algorithm needs to minimise χ^2 for all possible hit combinations, what is computational expensive. Local track following algorithms should be preferred in those cases over global fitting algorithms.

In the EUTelescope framework an *Analytical Track Fitting* algorithm is used to identify particle trajectories. To take multiple scattering in the detector planes into account, the algorithm aims to determine the particle positions separately for all eight planes, the DUT included, of the telescope. The separate contributions to the total χ^2 value can be calculated by

$$\Delta\chi_i^2 = \left(\frac{m_i - f_\lambda(l_i)}{\sigma_i}\right)^2 \Bigg|_{i \neq i_{DUT}} + \left(\frac{\theta_i - \theta_{i-1}}{\Delta\theta_i}\right)^2 \Bigg|_{i \neq 1,N} , \tag{7.5}$$

where N is the number of telescope planes, and θ_i describes the angle between the direction perpendicular to the telescope planes and the direction of the track between the planes i and $i+1$. The mean scattering angle $\Delta\theta_i$ is calculated from the Molière distribution

$$\Delta\theta_i = \frac{13.6\,\mathrm{MeV}}{\beta c p} z \sqrt{\frac{d}{X_0}} \left[1 + 0.038 \ln\left(\frac{d}{X_0}\right)\right] \tag{7.6}$$

where z is the charge, p the momentum and βc the velocity of the particle and $\frac{d}{X_0}$ the thickness of the scattering medium in radiation lengths. For the proton beam with an energy of 120 GeV used for the Fermilab beam test, the scattering angles in the telescope planes are small ($< 10\,\mu\mathrm{rad}$), with the comparably short distance of 1.4 cm between the separate telescope layers, multiple scattering does not play a large role in the track fitting procedure.

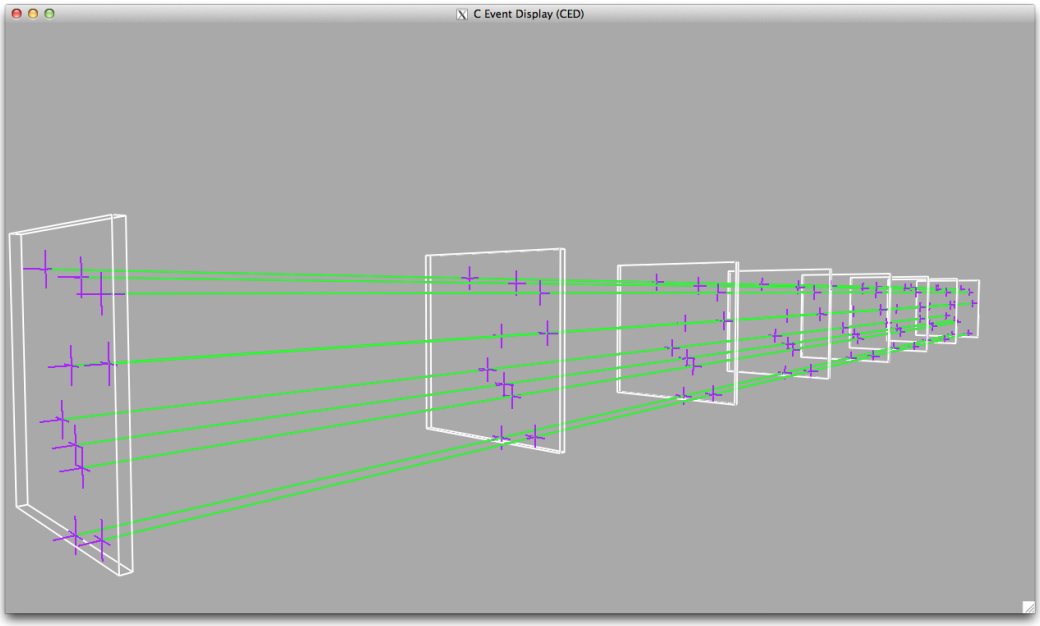

Figure 7.4: **Reconstructed tracks from simulated event**
The tracking algorithm tries to find particle trajectories from the hits on the aligned detector planes. The shown event display has been created with an simulated event with ten protons passing through the telescope simulataneously. The tracking algorithm is powerful enough to correctly identify all ten particle tracks.

7.2.6 Simplesub submission scripts

In order to execute all steps to find the tracks from the raw data Marlin provides simple submission scripts collected in the *simplesub* package. The scripts read parameters of a configuration file and insert them into the steering file for each processor. This simplifies execution of the full analysis chain and re-running of the analysis with varying input parameters.

7.2.7 Efficiency measurement

One of the main tasks of the High Rate Beam Test with the new PSI46dig readout chip was to test its high rate capabilities. The effects of data loss with respect to the track rate on the readout chip was studied. The detection efficiency ε for a given rate of tracks on the readout chip can be measured by counting the number of tracks that match to a hit on the DUT ($N_{\text{Tracks with hit on DUT}}$) with the total number of tracks found in the seven remaining telescope planes ($N_{\text{Total number of tracks}}$).

$$\varepsilon = \frac{N_{\text{Tracks with hit on DUT}}}{N_{\text{Total number of tracks}}} \tag{7.7}$$

To measure the efficiency from the reconstructed tracks a computer program was written. This code takes as an input the TTree object from the tracking algorithm output and also the rate measurement done with the QIE beam monitor device described in section 6.3.2. By associating the reconstructed events by their event number with the turn in which the trigger was sent to the telescope setup, a track rate can be assigned to them.

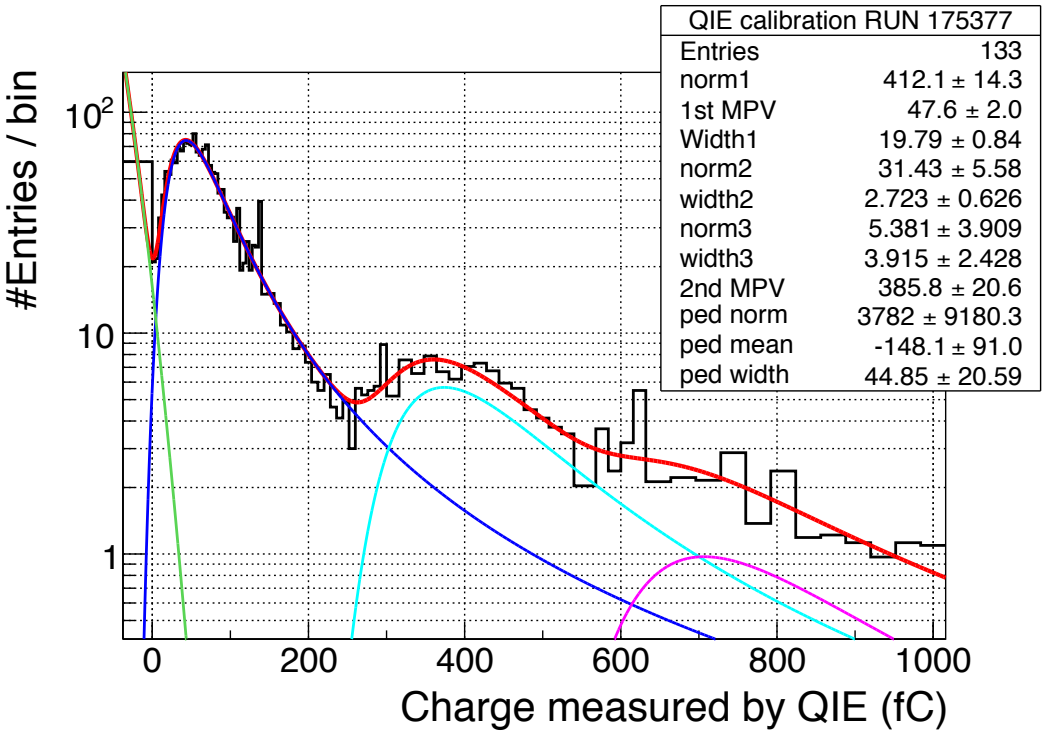

Figure 7.5: **QIE calibration**
The QIE device is calibrated by histograming the measured charge and fitting a multiple Landau distribution to the histogram. The fitted distribution is the sum of three Landau distributions with the distance between the first and second most probable value to be the same as the distance between the second and third.

7.2.8 Rate measurement

The rate of particles passing through both the tilted and the straight telescope has been measured with the QIE device, see section 6.3.2. In order to do this the measured raw data, the digitised pulse height of a photomultiplier output, has to be transformed to a number of particles in the beam.

The first step in doing this is to convert the digitized pulse height, coded in ADC values, from the raw QIE data into the actually measured charge. The mapping of QIE ADC values to charge is shown in figure 6.8. Next a conversion function is applied to the charge value measured for every 18 ns bunch.

$$\text{Number of Protons} = (\text{QIE charge} - \text{Pedestal}_{\text{turn}} + 260.0) \,/\, 320.0 \; . \tag{7.8}$$

The pedestal on the QIE measurement is evaluated for every turn of the Fermilab Main Injector separately by directly using the QIE value of bunch 32 out of the sequence of 588 bunches in the turn. The pedestal value is the QIE reading just before the first bunches filled with particles arrive, see figure 6.7.

The values for the slope and the offset of the conversion function have been found by the analysis shown in figure 7.5. The energy deposited in the scintillator by a single proton follows a Landau distribution. All measured charge values of a run have been histogrammed and a multiple Landau fit was done. Additionally to the charge from the measured particles a Gaussian distributed pedestal signal is measured by the QIE device. For the fit of the

multiple Landau distribution, the assumption was made that the difference in charge of all most probable values and their next neighbour is the same, thus reducing the degrees of freedom in the fit. The results shown for RUN175377 can be repeated for many runs to arrive at the final values for function 7.8. With this conversion the number of particles passing the $1\,\text{cm} \times 1\,\text{cm} \times 1\,\text{cm}$ scintillator crystal is known.

The next step is to normalise this value on the front surface of the beam telescope, and to correct for the misalignment between scintillator and telescope, and to correct for the Gaussian shape of the beam in the xy plane. For this purpose the two dimensional Gaussian distribution of hits on the first plane in the telescope was measured. The Gaussian beam does cover the full detector plane and the scintillator with hits, but the Gaussian is not centred on the middle of the detector nor on the scintillator. With the geometrical measurements of the alignment between the telescope and the QIE scintillator it was possible to determine the fraction of the beam incident on the telescopes relative to the QIE measurements.

Since the inefficiencies observed in the PSI46dig readout chip depend on the number of hits in a time window of the programmed ROC latency *WBC* before and after the triggered even and not the momentary hit rate, an average hit rate has to be computed from all measured values. The periodic trigger sent at a fixed time during each Main Injector turn makes it possible to know the beam intensity before and after each triggered event. The hit rate for a triggered event is then calculated by the average number of tracks in the time window before and after the event. For every triggered event also the maximum beam intensity within the relevant time window is saved, to be able to reject events with too large variations in the final analysis.

7.3 Problems Of The High Rate Beam Test

In chapter 6 the High Rate Pixel Telescope and the High Rate Tracking Area at Fermilab have been introduced. While this chapter focuses on the data analysis framework and the measurements obtained from the test beam at Fermilab 2014, it should also highlight several flaws and unexpected features of the test beam setup. These flaws need to be discussed as they will have an influence on the final measurement of the hit detection efficiency vs. track rate measurement.

7.3.1 Out-Of-Sync problem

The 'Out Of Sync', or OOS, problem was discovered early into the test beam. The problem is characterised by a reduction in the number of reconstructed tracks per time interval over the course of a single 4 s spill. It was found, that when operated with a periodic trigger of 90 kHz, single ROCs in the readout chain would lose the synchronisation with the other planes of the telescope. This effect lead to a decrease of the number of tracks found during the duration of a single 4 s spill. Since for the analysis a requirement was that tracks should have at least 6 hits in the 7 tracking planes of the telescope, this effect was highly unfavourable. To prevent the OOS effect from having a significant influence on the later data analysis, every 1000th trigger signal was replaced by reset signal to all readout chips. This reset signal synchronises the readout chips in the telescope at the cost of emptying all buffers and reseting all counters of the ROC.

7.3.2 Bit Error Rate

One of the most persistent problems with the High Rate Pixel Telescope during the Fermilab beam test was a high rate of bit errors in the raw data. Already in previous beam tests with earlier prototype versions of the PSI46dig readout chip and an early prototype of the telescope these problems were observed. A detailed report can be found in [Spa]. Although the design of the latest version of the telescope was focused on high signal quality and low noise pick-up the problem persisted. All attempts at improving the signal quality and excluding other potential noise sources by adding shielding and good grounding failed.

For the data analysis this means that a certain percentage of events have to be excluded. This is the case when one of the two following error conditions is found in the raw data stream:

Additional or missing ROC headers

Each ROC separately sends its data over a common data out line, as soon as the readout chip receives a readout token. The data transmission of each ROC starts with the ROC header. This ROC header has a fixed pattern that cannot occur in the data pay load.

When bit errors are introduced into the system, ROC headers are lost since the decoding algorithm interprets them as part of the data payload. It can also happen that an additional data pattern that has the form of a ROC header is created. During the data conversion step the number of ROC headers in each event are counted. The number of found ROC headers has to be equal to the number of ROCs present in the telescope. The entire event is discarded if the numbers of expected headers and found headers do not agree.

Incorrect pixel data

The bigger problem occurs when a bit error is created in the pixel data payload. While flipped bits in the headers can be found easily by simply counting them, the errors in the transmitted data is harder to identify. Only when the bit error creates a pixel address that lies outside the range of the readout chip addresses of 52 columns and 80 rows, the error can be found. Events in which this happens are discarded. However, bit errors in the data payload can change the data in a way that stays unnoticed during the conversion step. These unnoticed errors can lead to a misplacement of the reconstructed hit on the readout chip. The same problem applies to the transmitted pulse height of each pixel.

In the High Rate Beam Test the rate of events containing bit errors was of the order of $1 \cdot 10^{-3}$. This number is unusually high for any transmission of binary data. In the laboratory the conditions creating the bit errors could not be reproduced, which is why this effect was attributed to the high electromagnetic noise found in the High Rate Tracking Area.

7.3.3 Large Clusters

The expected occupancy of the pixel detector in CMS is below 2%. The PSI46dig readout chip was designed to cope with this particle density with little margins. When the High Rate Beam Test with its two telescopes was designed it was expected to find a small, close to $< CS >= 1$, average cluster size on the orthogonal telescope and a larger average cluster

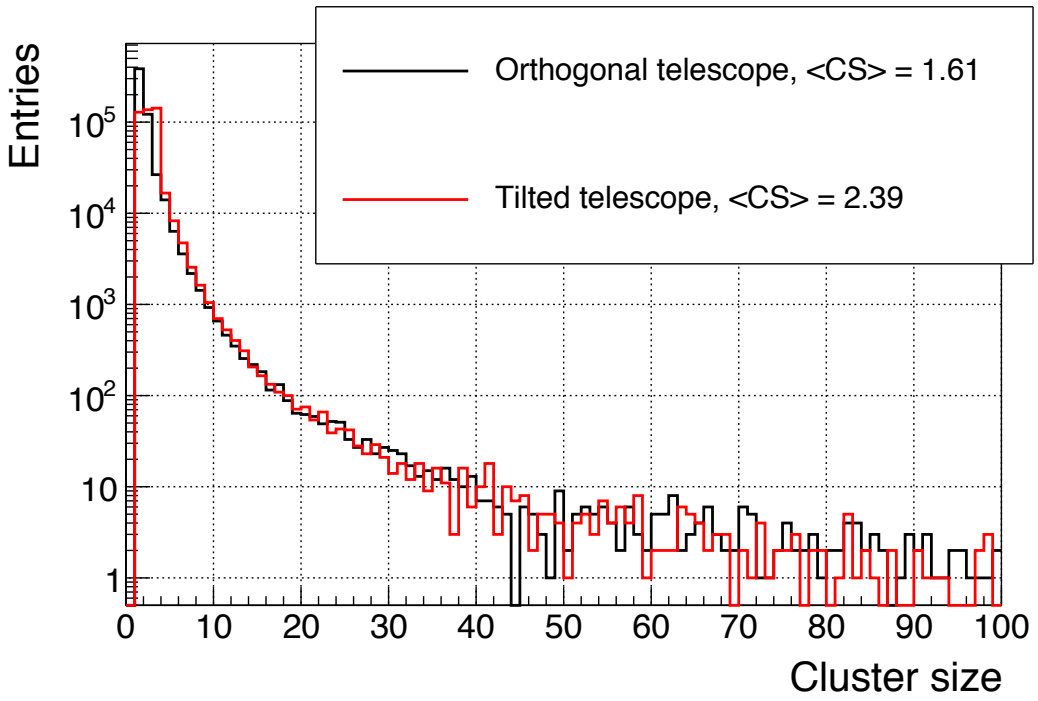

Figure 7.6: **Cluster size distribution for two different telescope geometries**
The cluster size distributions for an example run are shown. While the orthogonal telescope is mostly populated by single pixel hits, the tilted telescope sees a maximum at a cluster size of three. Both telescopes show an unexpected long tail in the distribution. Cluster with sizes of 20 and higher are not uncommon.

size, close to $< CS >= 1.6$, on the tilted telescope. However, the analysis of the measured data showed a different behaviour. The average cluster size found in the two telescopes was much larger than expected, mostly caused by a large tail of the cluster size distribution. The measured cluster size distributions for the orthogonal and the tilted telescope geometry, measured in RUN 176658, are shown in figure 7.6. Clusters formed by more than 10 pixels at a time occur on all telescope planes and at all times during the different runs.

Upon closer inspection it was found that most large cluster have either the shape of a filled circle or the shape of a ring. Example plots for both cases are presented in figure 7.7. Most of these 'monster' cluster events can be associated with a track through the telescopes, which supports the theory they are caused by a nuclear interaction of a proton with the sensor material, or with the non-sensitive surrounding material creating Cherenkov radiation.

Ultimately the source of large clusters could not be determined by closer analysis nor a simulation of the beam test. The large number of activated pixels in the events containing large clusters has a negative impact on the measured efficiency of the readout chip. The effect of large clusters on the measured efficiecny will be studied from simulation in chapter 8.

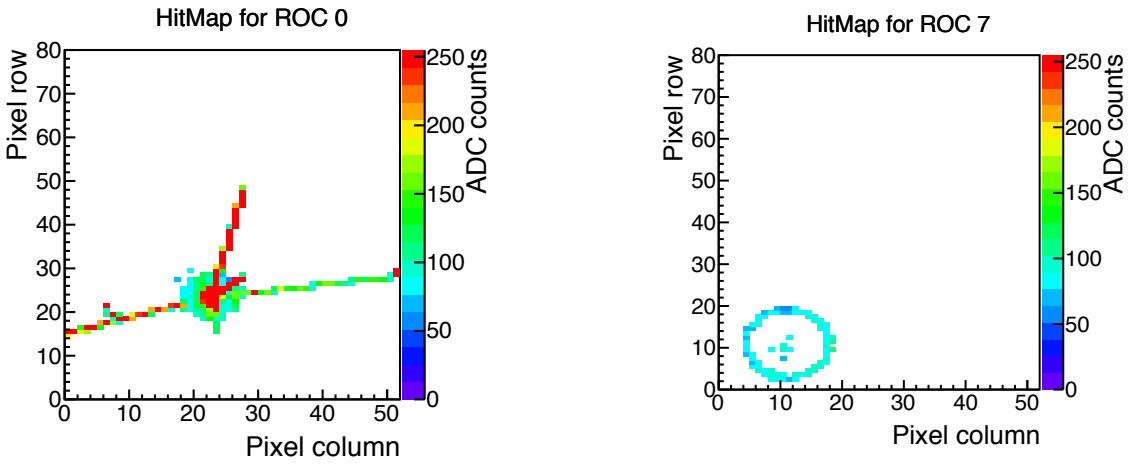

(a) **Monster Cluster Event: Circle** (b) **Monster Cluster Event: Ring**

Figure 7.7: **Monster Clusters**
Two examples for 'monster' clusters are shown. (a) has the shape of a filled circle. Several straight tracks originate from the center of the circle. It is assumed that a nuclear interaction in the detector is the cause of this shape. (b) shows a cluster with a ring-like shape. Cherenkov radiation is one possible source of this phenomenon.

7.4 High Rate Beam Test Measurements

After describing the telescope setup in chapter 6, showing the beam environment, explaining the data analysis chain and also detailing its problems, this section will focus on the results of the High Rate Beam Test (HRBT).

7.4.1 Resolution

The aim of the HRBT was to study the hit detection efficiency of the PSI46dig readout chip. At the same time additional measurements focusing on the performance of the detector units were done. The resolution of reconstructed tracks was measured on the DUT by comparing the fitted track position with the measured hit position. The difference of these two measurements is called the residual. As discussed in section 3.3.5 about the spatial resolution of tracking detectors, the expected resolution of the High Rate Pixel Telescope, applying the centre-of-gravity method for hit reconstruction, is expected to be better than the theoretical limit for a binary readout of the pixels. These theoretical limits are only dependent on the pitch between pixels, which in the case of the CMS pixel sensor are

$$\sigma_{\text{theo.lim. x}} = \frac{150\,\mu\text{m}}{\sqrt{12}} = 43.3\,\mu\text{m} \tag{7.9}$$

in the direction of the x-axis and

$$\sigma_{\text{theo.lim. y}} = \frac{100\,\mu\text{m}}{\sqrt{12}} = 28.9\,\mu\text{m} \tag{7.10}$$

in the direction of the y-axis.

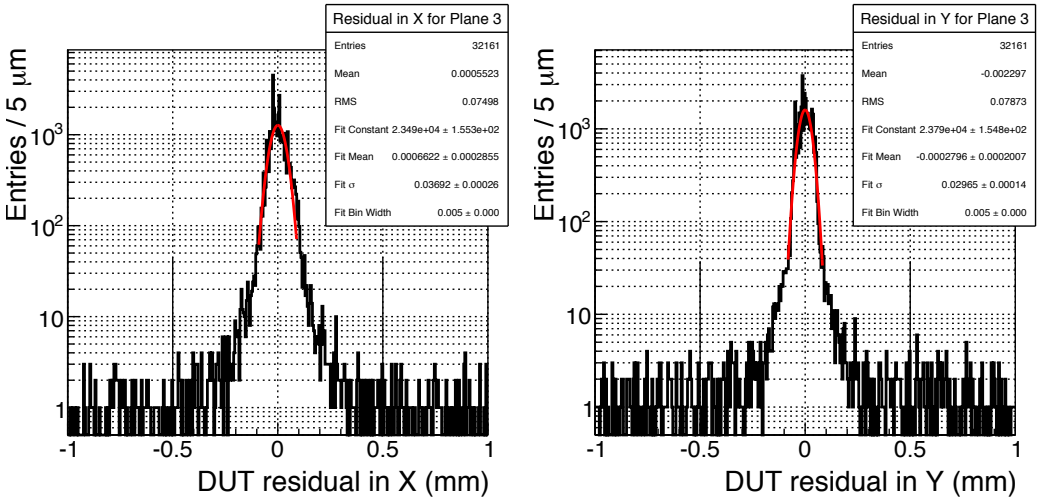

Figure 7.8: **Position resolution of the DUT for the orthogonal beam telescope**
For the orthogonal telescope the position resolution was measured in the DUT. The residuals in the x- and y-direction are of the order of what was expected from a telescope with binary readout. Most hits on the orthogonal telescope are single pixel clusters, hence the measured pulse height does not improve the position resolution because a centre-of-gravity algorithm can not be applied.

These values can be easily compared to the measurements performed on the Device Under Test by calculating the residuals in the x- and y-axis for all tracks of a single spill and histograming them. The results for the simple 'straight' or 'orthogonal' telescope with all planes, including the DUT, perpendicular to the incident beam can be seen in figure 7.8. In the straight telescope, where charge sharing between pixels is dominated by the diffusion of charge carriers, a position resolution of $\sigma_{\text{meas. x}} = 37\,\mu\text{m}$ and $\sigma_{\text{meas. y}} = 30\,\mu\text{m}$ is obtained. As expected the position resolution has not improved by much compared to the expected values for a binary readout. Most clusters created by particles are single pixel hit clusters. For those hits a large ambiguity on where on the pixel the hit occurred exists. Unless the charge sharing is being increased by a magnetic field (Lorentz angle) or by tilting the sensor, a telescope with a pixel pitch much smaller than the diffusion length σ_{diff} will always be close to the limits of binary readout. For the example of the CMS silicon sensor with a thickness of $\approx 300\,\mu\text{m}$ and an applied bias voltage of $U = 150\,\text{V}$, the diffusion length of charge carriers at room temperature $T \approx 300\,\text{K}$ can be approximated to be $\sigma_{\text{diff}} \approx 5.5\,\mu\text{m}$.

The way in which charge sharing was improved in the High Rate Beam Test was a simple tilt of the sensor planes by $30\,^\circ$ along the direction of the x-axis and by $20\,^\circ$ along the y-axis. In the tilted telescope most incident particles cross more than one sensor pixel volume on the way through a sensor plane. The results for the detector geometry with tilted sensor planes can be seen in figure 7.9. For the residuals the increased charge sharing results in a much better spatial resolution of $\sigma_{\text{meas. x}} = 27\,\mu\text{m}$ in the x-direction and $\sigma_{\text{meas. y}} = 16\,\mu\text{m}$ in the y-direction.

Compared to other beam telescopes, like the already mentioned EUDET telescope based on the MIMOSA readout chip, the resolution of the HRPT is relatively poor. The High Rate Pixel Telescope has several disadvantages in this comparison. The pixels of the HRPT are

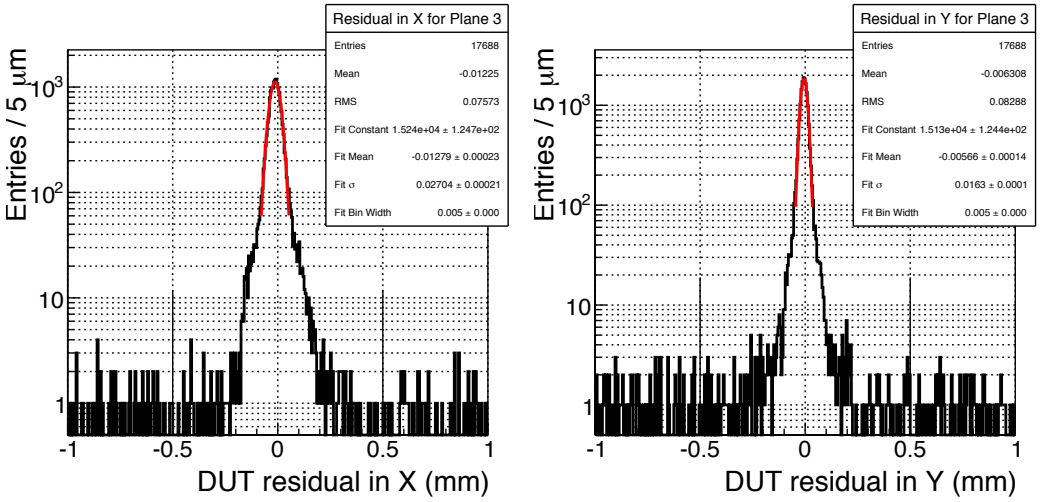

Figure 7.9: **Position resolution of the DUT for the tilted beam telescope** The position resolution for the tilted telescope is better than the resolution of the orthogonal telescope. The increased charge sharing by inclining the sensor planes is beneficial for the position resolution of the telescope.

46-times larger than the pixels of the EUDET telescope, hence charge sharing has to be introduced by a tilt of the sensor planes when an external magnetic field is absent. Additionally, in order to zero suppress the data a charge threshold is implemented in the PSI46dig chip. Very small charges are never measured distorting the hit position reconstruction via the used center of gravity method.

At the same time the resolution found with the High Rate Pixel Telescope can be compared to the resolution found in the CMS barrel region, since in both cases the pixel size and sensor thickness are the same, and the angles in the tilted telescope have been chosen to emulate the Lorentz angle in the real detector. With a resolution between 8.0 µm and 9.5 µm in all three layers [Bur14], the resolution of the current pixel detector is twice as good as what has been achieved with the HRPT.

7.4.2 Efficiency Measurement

The most important measurement done, and the actual reason for the High Rate Beam Test, was the hit detection efficiency of the PSI46dig chip. The entire test beam setup was designed to make this final measurement and to validate the final readout chip prototype before going into a large scale production of the Phase 1 Upgrade of the CMS detector. As described in 6.4 the goal was to measure the rate dependence of the hit detection efficiency for different latency settings of the readout chip and also for different trigger times during the 369,000 Main Injector turns of the beam extraction.

The efficiency is measured as explained earlier in the chapter, see section 7.2.7. For all measurements shown the fourth detector plane (ROC3) has been used as the device under test. The other seven planes of the telescope are used as tracking device to find good tracks. The conditions for a track is that there are matching hits on at least six of the seven tracking telescope planes and that the final χ^2 value of the track is smaller than 50. A hit on the DUT is considered efficient if it can be matched to the fitted incident point on the DUT of a track not further than 0.5 mm away.

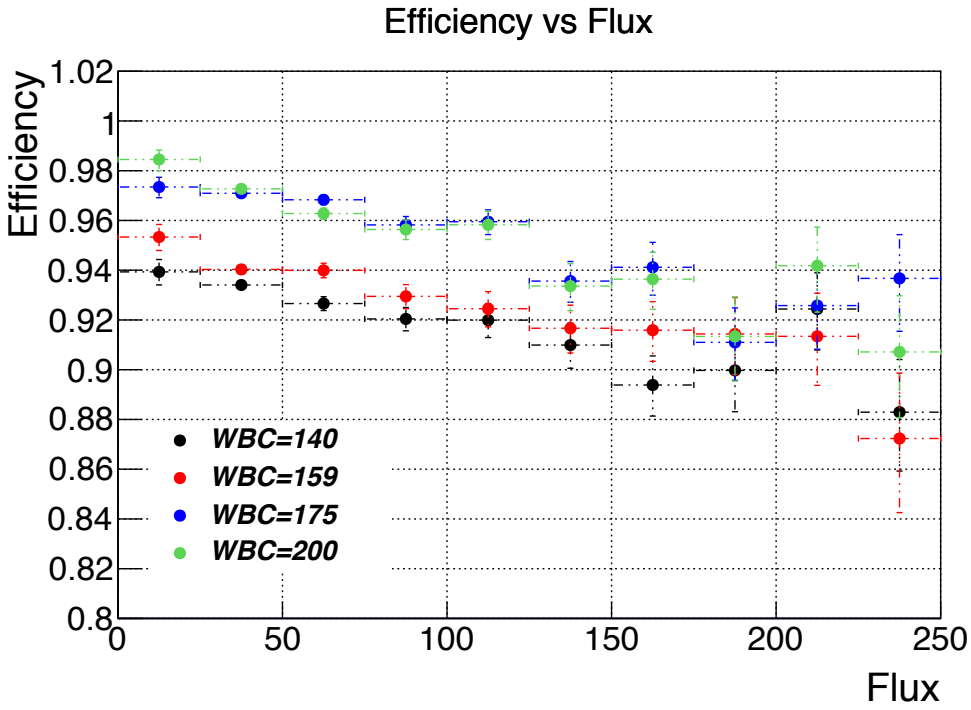

(a) **Efficiency measurement for the orthogonal telescope**

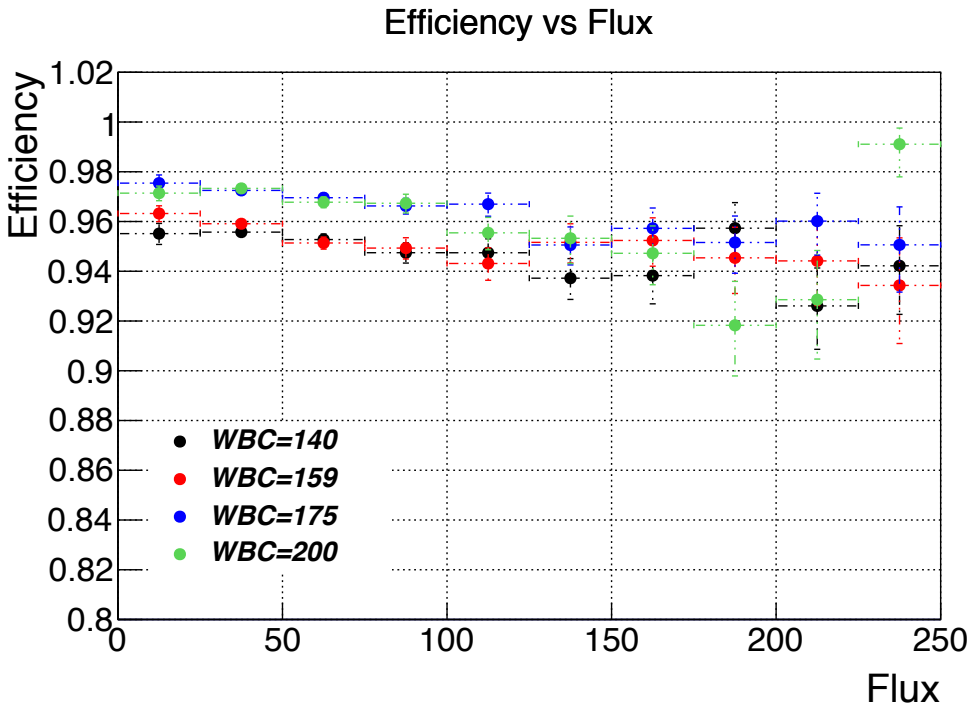

(b) **Efficiency measuremnet for the tilted telescope**

Figure 7.10: **Efficiency measurement**
From the gathered data of the 2014 Fermilab beam test the hit detection efficiency of the PSI46dig readout chip was measured. The measurement was done by trying to match hits on the DUT to tracks reconstructed in the seven tracking planes of the detector. The efficiency found never reaches a full 100% even for small beam rates and the hit detection efficiency does not drop was fast as one would have expected. The dependence of the measured efficiency behaves inverse to expectations. With a higher WBC setting the efficiency should be lower.

To assign a particle rate to each hit the QIE data is used. With the knowledge of the number of protons within the beam on a bucket-by-bucket basis it is possible to assign a hit rate to each trigger. The time window for which the hit rate is assigned varies by the programmed WBC settings in the readout chips.

For the data analysis events that were found to contain bit errors in the raw data stream have been excluded.

In figure 7.10a and figure 7.10b the results for the orthogonal and the tilted telescope respectively are shown. The intention of the two telescopes was to stress different inefficiency sources in the readout chips. While the orthogonal telescope would target the inefficiencies created by an overflowing time stamp buffer, the tilted telescope could target the inefficiencies in the data buffer of the ROC. It proved to be correct the majority of clusters formed on the orthogonal telescope were single pixel clusters, while the cluster size distribution on the tilted geometry showed larger clusters. However, both telescopes equally showed the feature of the 'monster' clusters described in section 7.3.3 that influence the measured efficiency.

The reconstructed efficiency for four different values of the ROC internal delay are plotted against the particle flux measured with the QIE device. As already described only a single trigger was sent during each turn of the Fermilab Main Injector. This periodic trigger was necessary since the QIE device was not able to receive an acknowledge signal from the test board controlling the telescopes, and with a random triggering scheme the correlation between hit and beam rate would have been lost.

The presented measurements for the orthogonal and the tilted telescope both show three remarkable and unexpected features:

- The efficiency does not reach 100% for low particle fluxes.
- The efficiency does not drop as much as expected for high fluxes
- The efficiency for the different WBC settings behaves inverse to expectations.

From first simulations that were made by the PSI46 chip's designer and published in the Technical Design Report for the CMS Phase 1 Upgrade [Col12] it was expected that the pixel hit detection efficiency would be close to 100% at very low rate of particles. With an increase in particle rate the efficiency was expected to drop significantly, especially for high values of WBC. What was found by analysing the test beam measurements was the opposite. Higher values of WBC showed a higher hit detection efficiency.

Similar results were obtained from the other measurements with different trigger conditions, but ultimately the telescope setup proved to be not sensitive enough to measure the real inefficiencies in the readout chips.

7.5 Conclusions and Next Steps

For the High Rate Beam Test of the CMS Phase 1 Pixel upgrade readout chip a full analysis software chain was implemented. Based on the EUTelescope framework this analysis chain reached from the conversion of raw data up to finding high level track objects in the hit collections measured by the telescope with eight planes.

During the test beam two flaws have been discovered. A small percentage of the raw data is filled with corrupt pixel readouts. Most can be easily identified since pixel hit coordinates outside of the 52×80 pixel array of a ROC should not exist in the data stream. Additionally unexpectedly large clusters were found in all the data samples. They seem to originate from

particles, as they are predominantly connected to tracks. But ultimately a source for these large clusters with up to many hundreds of hit pixels could not be determined.

The data taken with the High Rate Pixel Telescope proved not to be sensitive enough to measure the inefficiencies in the readout chips. Data taken with the orthogonal and the tilted detector geometry show a general decrease in hit detection efficiency. But the uncertainties on the measured rate and the uncertainty on the occupancy during the WBC long time window before and after the triggered hit, make the rate measurement of particles passing though the telescope highly inaccurate.

In order to find the reasons behind the low sensitivity of the High Rate Pixel Telescope setup to the inefficiencies of the readout chip, the entire beam test is to be simulated. The next chapter of this thesis details this endeavour from the track and hit creation in a *Geant4* simulation of the test beam setup, to a detailed simulation of the inner workings of the readout chip.

Chapter 8

Beam Test Simulation

Given the complex conditions during the Fermilab beam test (described in chapter 7), such as clock mismatch between beam and readout chip and the large clusters, the measurements of the PSI46dig readout chip's efficiency could not be directly interpreted without a comparison to a dedicated simualtion. The goal of the simulation is to simulate as closely as possible the beam conditions found in the Fermilab Test Beam Facility and to simulate the readout mechanism of the PSI46dig readout chip and its readout chain.

Generally the High Rate Test Beam Simulation is divided in two blocks. The first part is a simulation of the passive telescope mechanics material and the active sensor material realised in the *Geant4* framework. This simulation software is widely used in high energy particle physics. Here it is used to generate a collection of tracks with the same spatial distribution as found in the test beam analysis. The second part consists of the simulation of the High Rate Pixel Telescope readout on a 25 ns clock cycle basis. A detailed readout chip simulation, verified by laboratory measurements, processes every pixel hit like the physical PSI46dig ROC does. The output of the telescope simulation is in the same format as the converted raw data from the test beam and is run through the same analysis.

This chapter will start by focusing on the separate parts of the simulation. The *Geant4* part of the simulation is detailed first. Secondly the simulation of the PSI46dig readout mechanism is shown and the simulation code is validated against measurements done in the laboratory. Then both parts are combined in the High Rate Beam Test simulation. Several potential mechanisms are identified that influence the efficiency measurement. They are examined separately before all effects are combined to the full beam test simulation. At the end of the chapter a recommendation for future test beams is given.

8.1 Geant4 Telescope Simulation

The generation of simulated tracks was done by using version 10.0.3 of the *Geant4* simulation framework [Ago03]. *Geant4* is a C++ based framework, developed by an international collaboration, to accurately model and study particle detectors. The size of experiments simulated and detector geometries studied with *Geant4* varies greatly, from small test beam setups, like the example presented here, to full-scale detector simulations of experiments at the LHC.

Geant4 simulates the passage of particles through matter. The framework is able to simulate a large set of long-lived particles and the physics processes in which they interact with matter. The *Geant4* framework provides all key parts for the simulation:

- Detector geometry and material definitions
- Interaction of particles in matter

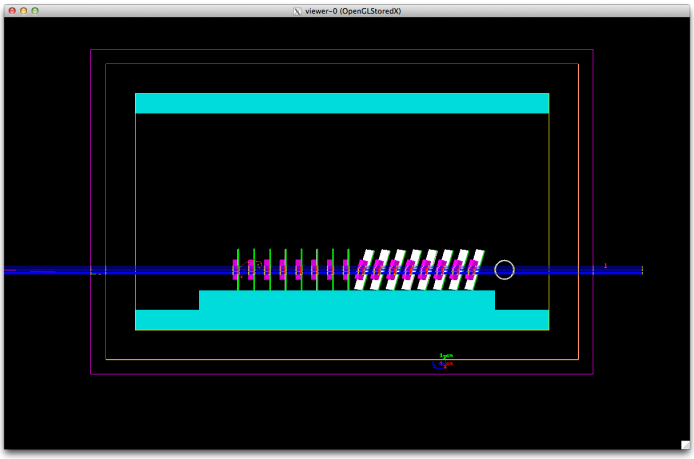

Figure 8.1: **Simulation Geometry**
Screen capture from the *Geant4* simulation of the High Rate Beam Test. The picture visualises the two telescopes with eight planes each. The telescopes are simulated simultaneously. Additionally to the telescopes the surrounding cooling box and the massive aluminium cooling blocks are simulated. The picture shows the trajectories of ten simulated protons passing through the telescopes.

- Tracking management
- Digitisation and hit management
- Event and track management
- Visualisation
- User interface

For every *Geant4* simulation there are three mandatory C++ classes that need to be defined by the user: `G4VUserDetectorConstruction`, `G4VUserPhysicsList` and `G4VUserPrimaryGenerator`. They describe the how the simulated device is geometrically built and from which materials it is made, which physics processes are supposed to be simulated and which primary particles should be generated in an event. In addition there are five optional user classes that can be used to modify the default behaviour of *Geant4*: `G4UserRunAction`, `G4UserEventAction`, `G4UserStackingAction`, `G4UserTrackingAction` and `G4UserSteppingAction`.

In the following the focus is on the implementation of the three mandatory classes in the simulation of the High Rate Pixel Telescope.

8.1.1 Detector Geometry

In the simulation of the test beam performed at Fermilab it was important to reproduce the telescope mechanics and geometry as closely as possible, while omitting unnecessary details like cables and electronic boards far away from the sensors. The resulting geometry simulates two telescopes inside a polyvinyl chloride (PVC) box with a wall thickness of 1.5 cm. The inside of the box is covered by a 3.0 cm thick polystyrene foam layer simulating the thermal insulation of the cooling box in the test beam. The composition and density of all

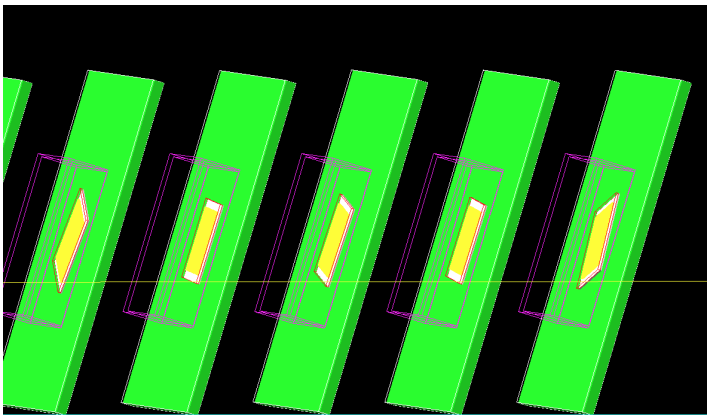

Figure 8.2: **Simulated Detector Alignment**
The telescope is simulated with misaligned detector planes. The misalignment is randomly created and lays between ±300 µm in the x- and in the y-axis. A random rotational misalignment of the detectors has also been introduced. The detector is rotated between ±0.8 ° around its center. For illustration purposes, here the misalignment is increased by a factor of 50.

simulated materials can be seen in table 8.1. The physical properties of materials in *Geant4* are described by the density and element composition from which characteristics such as radiation and interaction length are computed. Aluminium plates with a thickness of 2.0 cm simulate the Peltier cooling contacts at the top and bottom of the simulated cooling box. An additional 2.0 cm thick aluminium plate simulates the mounting plate of the telescopes' mechanical structure. In front of the telescopes, aligned with the simulated volumes for the readout chips, a mylar tube with a radius of 1.0 cm and a wall thickness of 1 mm representing the installed scintillator with air light guide is simulated.

A single telescope plane is defined as a logical volume that holds the physical volumes of the G10 carrier board, the silicon readout chip, the silicon sensor and a plastic cap covering the sensor. All 16 planes are constructed as translated and rotated copies of the first logical volume. The G10 carrier board is modelled to be 1.2 mm thick and to have a square surface with 4.2 cm edge length. Stacked on top of this carrier is a 1 cm × 1 cm × 0.2mm volume simulating the material of the readout chip in the telescope. The sensor is also simulated as a volume made from silicon. It is highly segmented to simulate the separate pixels of the real detector. Only the simulated silicon sensor is defined as a sensitive volume, that means only the charge deposited inside the silicon sensor is preserved in the digitised hit information of a passing particle as described in the next section. A misalignment between the sensor planes can be simulated. The translational misalignment in the direction of the x- and y-axis is between ±300 µm and has been randomly assigned. To simulate rotational misalignment between the detector planes, the simulated hybrid detectors are rotated randomly around their center by ±0.8 °. These values were chosen after examining the results from the alignment in the data collected in the real test beam and by estimating the potential maximal misalignment from placing the detectors by hand on the carrier board. In figure 8.2 the simulated rotational alignment is visualised by scaling the misalignment angle by a factor of 50.

Table 8.1: **Materials used in Geant4 simulation**

Material	Elements	Density
Silicon	Silicon (Si, 100%)	2.33 g/cm^3
Aluminium	Aluminium (Al, 100%)	2.70 g/cm^3
Air	Nitrogen (N, 70%) Oxygen (O, 30%)	1.29 mg/cm^3
G10	Silicon (Si, 11.1%) Oxygen (O, 22.2%) Carbon (C, 33.3%) Hydrogen (H, 33.3%)	1.70 g/cm^3
Polyvinyl chloride	Carbon (C, 33.3%) Hydrogen (H, 50.0%) Chloride (C, 16.7%)	1.40 g/cm^3
Polystyrene foam	Carbon (C, 50%) Hydrogen (H, 50%)	0.03 g/cm^3
Mylar	Carbon (C, 45.5%) Hydrogen (H, 36.4.0%) Oxygen (O, 18.2%)	1.38 g/cm^3

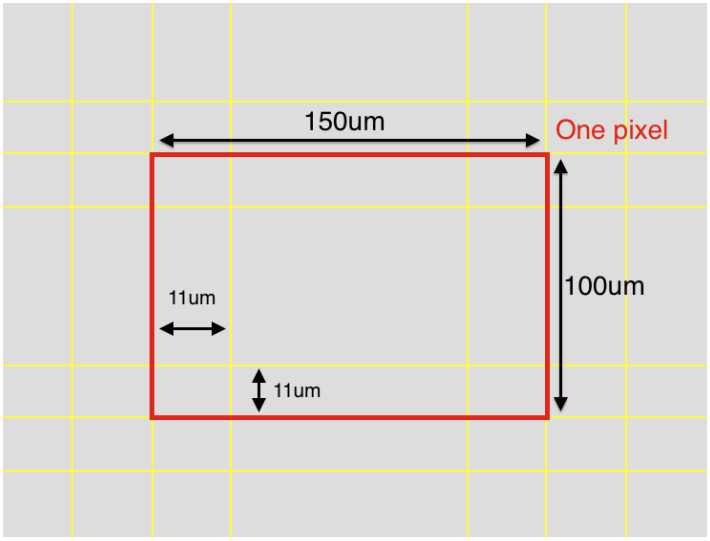

Figure 8.3: **A simple charge sharing model**
The simple charge sharing model for the telescope simulation is presented. Each pixel is subdivided into nine volumes of different sizes. Only charge deposited in the central volume stays completely there. Charge deposited in the edge volumes share a fraction of the charge with the adjacent neighbour. Sizes are not to scale.

A Simple Charge Sharing Model

To simulate charge sharing between pixels in the simulated silicon sensor a simple model was used. It reproduces the cluster size distribution found in a CMS pixel sensor under vertical particle incident well.

An important part of a detector simulation performed with the *Geant4* framework is the definition of sensitive material, the creation of hits and the digitisation of these hits. *Geant4* records the simulated physical interactions of a particle only for sensitive materials. Such a recording is called a *G4 hit*. For the High Rate Pixel Telescope simulation only the 285 µm thick silicon sensor is defined as sensitive volume. The entire sensor is sub-divided into smaller volumes, all numbered individually. Each volume represents a separate pixel with a size of 100 µm by 150 µm. When a particle passes through one of these sensitive volumes a G4 hit is created. The G4 hit stores the exact entry point of the particle and also the energy deposited in the volume is recorded.

To simulate the effect of charge sharing in the simulated silicon sensor the 4160 sensitive pixel volumes were divided even further. A single pixel is divided into nine smaller volumes of different size, as shown in figure 8.3. After the passage of a particle through the telescope is simulated, the G4 hits are reevaluated. G4 hits that happened in one of the eight outer volumes of a single pixel share a percentage of their collected charge with the neighbouring pixels. The charge deposited in a volume directly neighbouring only one other pixel is shared with a ratio of 2:1: two-thirds remain in the original pixel and one-third of the charge is assigned to the neighbouring one. If one of the four sub-volumes in the corners are hit, one-ninth of the deposited charge goes to the neighbouring pixel on the diagonal. The other two direct neighbours receive two-ninth of the deposited charge each. If the large central volume is hit no charge is being shared with the neighbouring pixels. This simple model of charge sharing represents the charge shared between pixels in a real silicon sensor due to the diffusion of charge carriers but it does not simulate the charge sharing between pixels due to the induced signals from moving charge carriers.

The size of the charge sharing zone was estimated from the average diffusion distance of electrons in silicon and the size was optimised using high precision tracking measurements done at DESY, Hamburg for the CMS Phase 1 upgrade[Pit15].

8.1.2 Simulated Physics

In *Geant4* the user can decide which physics models to use. In some cases it makes sense to neglect certain effects to speed up simulation time and save computing resources. For the simulation of the High Rate Pixel Telescope only a short list of elementary particles and hadrons were considered. The list of particles and the simulated physics processes through which they interact with matter and other particles is shown in table 8.2.

8.1.3 Primary Particles

Apart form the detector geometry and the simulated physics processes the last mandatory user input to the *Geant4* simulation are the primary particles. To simulate the High Rate Test Beam the necessary input values where taken from the information given by the Fermilab Test Beam Facility [FNA15]. The simulated particles are protons with a kinetic energy of 120 GeV. In every event a single proton is generated randomly distributed on a surface of 1 cm × 1 cm at $z = 0$ cm in the simulation's coordinate system. The first plane of the tilted telescope is positioned at $z = 15.5$ cm. Every generated primary particle has as momentum

Table 8.2: **List of particles and interactions included in the full telescope simulation** [Ago03]

Category	Particle	Interactions included in simulation
Bosons	Photon	Photo electric effect Compton scattering Photon conversion
Leptons	Electron Positron Muon Antimuon	Multiple scattering Ionisation Bremsstrahlung Pair production and annihilation
Hadrons	Proton Antiproton Pion Antipion	Multiple scattering Ionisation Bremsstrahlung Pair production
Ions	α particle Generic ion	Multiple scattering Ionisation

direction associated with it. The momentum direction is determined by a narrow Gaussian distribution around the z-axis.

8.1.4 'Monster' Clusters

An unexpected feature found in the 2014 test beam at Fermilab were the unusually large circular or ring-like shaped clusters. The simple *Geant4* simulation is not able to reproduce these not yet understood findings. Since the large amount of pixel hits in a large cluster on the readout chip can affect the readout efficiency, the large clusters needed to be reproduced in the simulation. To do this two power law distributions were fit to the cluster size distribution found in the measured data, as shown in the upper left panel of figure 8.4. Based on these two distributions, when generating tracks in the *Geant4* simulation, large clusters are added randomly in the simulation. All large clusters in the simulation of the high rate particle telescope are part of a track. In figure 8.4 the comparison between the simulated and the measured cluster size distribution is shown in the lower right panel. The two distributions agree by construction apart from the statistical fluctuations. Since the source of the large cluster events is still unknown it was not possible to link the creation process to a simulated physical process in *Geant4*.

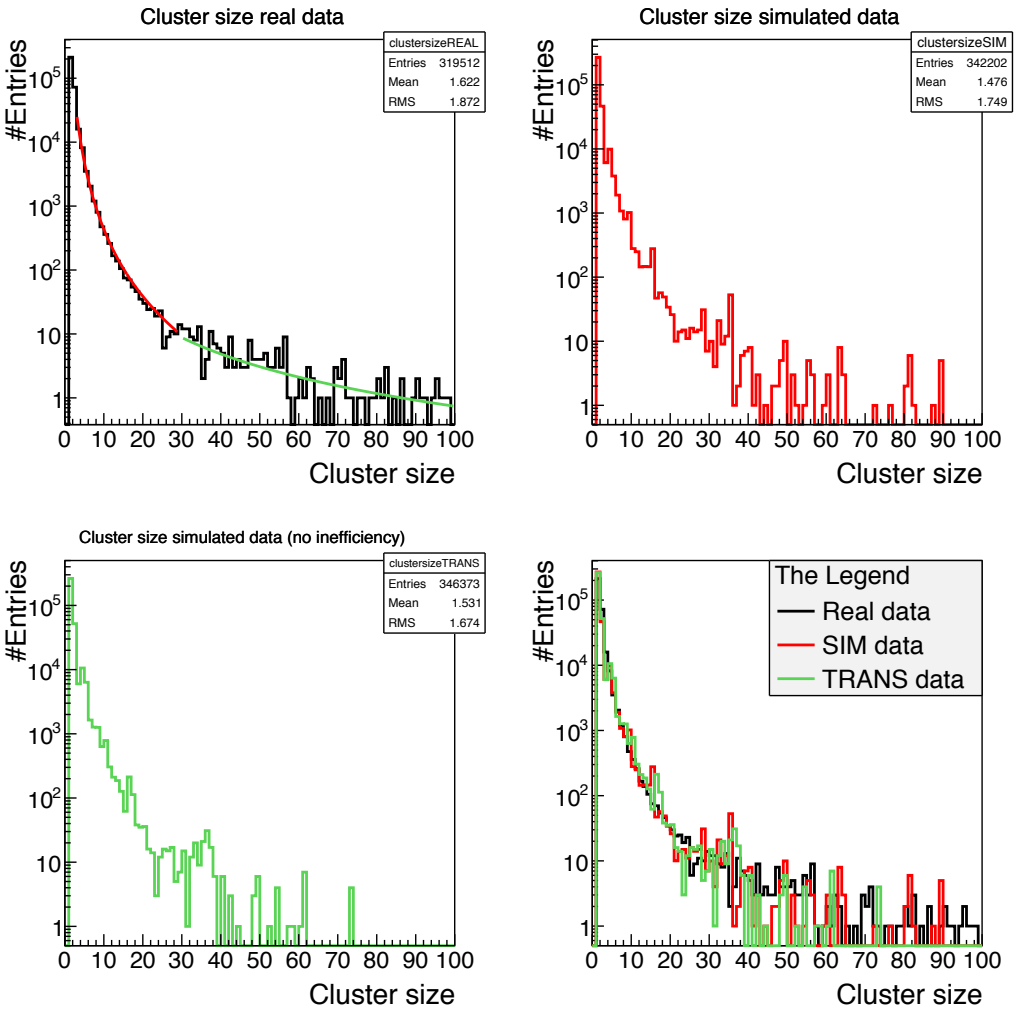

Figure 8.4: **Simulation of monster clusters**
To simulate the effect of 'monster' clusters on the reconstructed efficiency, circle or ring shaped clusters have been randomly added to the simulation. To adjust the cluster size distribution correctly, two power laws were fitted to the measured distribution, as shown in the upper left panel. The plot on the upper right side shows the cluster size distribution on a simulated ROC after all inefficiencies have been applied. The lower left figure shows the same simulation without any inefficiencies in the readout chip. All three distributions are compared again in the last plot. The different cluster size distributions match by construction apart from statistical variations.

8.2 PSI46dig Readout Simulation

An important part in replicating the High Rate Test Beam experiment is the correct simulation of the PSI46dig's readout mechanism. For this purpose the already existing C++ ROC simulation, used for the Technical Design Report for the Phase 1 upgrade of the CMS detector [Col12], was used as a starting point for the development of a stand-alone ROC simulation. After evaluating the simulation code, several crucial corrections were made, to closer replicate the readout logic of the PSI46dig chip. This section will describe the C++ ROC simulation and the validation of the simulation code against laboratory measurements.

8.2.1 C++ Readout Simulation

The readout simulation described here is written in the C++ programming language. C++ was chosen due to its fast execution speed of the finished compiled program, needed to simulate a large number of clock cycles of the readout chip.

The ROC simulation is called *DataFlow*, it describes the flow of hit information from the hit creation in the pixel unit cell of the readout chip up to the point where data is read out from the Front End Driver. The DataFlow simulation reads from an event file with a certain number of pixel hits, pixels that have been activated, per event. The number of hits per 25 ns clock cycle defines the hit rate seen on the readout chip. Each hit is processed individually and on a 25 ns clock cycle basis. Pixel hits that get lost due to readout inefficiencies are marked and internally accounted for, separatly by the cause of inefficiency. The final result of the simulation is a text output of how many pixel hits were processed and how many got lost, allowing to compute the total inefficiency of the simulated readout.

Event File Creation

The DataFlow simulation framework is able to simulate the readout of an arbitrary number of CMS Barrel Pixel modules at the same time. This way the performance of the detector as a whole can be studied. However, for the studies done in this work only a single module was simulated. All pixel hits that have been simulated are created on a single readout chip. To study the readout efficiency as a function of the pixel hit rate the ROC sees, a short program was written, that creates input files with a uniform distribution of hits over all the pixels of the ROC studied. Two input parameters can be varied: the pixel hit rate and the cluster size distribution. The hit rate can be changed to study the dependence of the hit rate on the simulated readout efficiency of the readout chip, whereas the cluster size distribution can be changed to simulate different types of particles, that is, X-rays with an average cluster size of 1 or charged particles from LHC collisions with an average cluster size of 1.6.

DataFlow Simulation

The DataFlow simulation program was originally written by Hans-Christian Kästli to simulate the performance of the upgraded CMS Barrel Pixel detector [Col12]. To make use of the DataFlow code for the simulation of the High Rate Test Beam it was important to compare it with the intended behaviour of the readout chip and to compare the results with measurements.

The DataFlow simulation is built from several classes that together simulate the readout of the CMS Phase 1 Upgrade Barrel Pixel detector. These classes are:

`Hit`

The `Hit` class stores all important information about a simulated pixel hit on a ROC. Basic information, such as the ROC on which the hit occurred, the position of the hit and the pulse height are registered. Every hit has its own timestamp and a flag if it is triggered on.

`Event`

An `Event` is a collection of `Hit`s that are added to the DataFlow simulation. The `Event` also stores trigger information for the readout.

`EventReader`

The task of the `EventReader` class is to read new `Event` from a collection in the previously created event file. These `Event`s and the `Hit`s they contain are then added to the simulation and placed on the corresponding `Module`s, see below.

`Module`

This class is the software implementation of a CMS Barrel Pixel module. Each `Module` consists of up to 16 `ROC`s that are controlled by one or multiple Token Bit Managers represented by the `TBM` class. The `Module` class itself has two important functions: The first is `Module::AddHit()` that adds hits to the different ROCs and `Module::Clock()` that advances the clock on the `Module` and consequently all associated `ROC`s.

`TBM`

The C++ implementation of a single `TBM` core controls the same aspects of the simulation as the real TBM does. The trigger signals from the main program are fed to the connected readout chips. After a short time delay a token is sent out that collects hits from all readout chips. The `TBM` class registers how long the token takes to pass all `ROC`s. Up to 16 triggers can be stacked while a readout token is passing though the detector already.

`ROC`

The `ROC` class handles all incoming commands from the `TBM` and relays them to the 26 `DoubleColumns`, see below. The `ROC` class is also responsible for the readout buffer, a FIFO that collects the readout data from all `DoubleColumns` before the readout token from the `TBM` arrives. The internal token chain for transferring data from the `DataBuffer`s of a `DoubleColumn` to the readout buffer is also controlled by the `ROC` class.

`DoubleColumn`

The `DoubleColumn` class is the heart of the simulation. Here `Hit`s are added to the readout and processed on a clock-by-clock basis. The `DoubleColumn` class controls which `Hit`s are read out and which `Hit`s are being discarded during the processing steps. If a `Hit` is inefficient the reason is for its inefficiency is recorded by the `DoubleColumn` object.

`DataBuffer`

Each `DoubleColumn` class contains a single `DataBuffer` with 80 storage cells for `Hit`s. In every clock cycle it is checked if `Hit`s have expired and should be removed from the `DataBuffer` or if they are triggered on and consequently read out.

`TimeStamp`
: If there is at least one new hit in a `DoubleColumn` a new `TimeStamp` is created in the time stamp buffer. If a `TimeStamp` expires all associated hits are removed from the `DataBuffer`.

`Statistics`
: The statistics class collects information from all `ROC`s about the number of `hits` that have been added to the readout, how many triggers were sent and how many hits got lost during the readout process. The inefficient hits are separated into six different categories.

Pixel Overwrite
: When a pixel is hit a second time, while the hit was waiting for the column drain token to arrive, the hit is lost.

Column Drain Busy (3rd Hit)
: When a double column is hit in three consecutive bunch crossing, the third hit will be associated with the wrong ColOR line, see chapter 4. After the hit is drained from the PUC to the periphery it is associated with an incorrect time stamp, thus making it inefficient.

Time Stamp Buffer Overflow
: After all cells in the time stamp buffer of a double column are occupied no new time stamps can be assigned to incoming hits. All future hits are associated with the last timestamp added to the buffer and thus marked as being inefficient, until a time stamp buffer cell is freed.

Data Buffer Overflow
: When all buffer cells of the data buffer are full, the double column resets itself, deleting all hits previously stored. The hits in the data buffer that have not already been flagged as inefficient are now added to the statistics of inefficient hits

Column Blocked For Readout
: While the hits in the data buffer of a double column are transferred to the readout buffer of its ROC, no new hits are being saved. All incoming hits during the readout process are marked as inefficient.

Reset After Readout
: After the transfer of data from the data buffer to the readout buffer has finished the double column resets itself. Hits still in the data buffer and hits arriving during the three clock cycles long reset are marked as inefficient.

An example summary statistics output for a single ROC looks as followed:

```
*******************************************************
Statistics for Roc number 0
Total number of hits:      3477163
Pixel overwrite:                 16938 ,   0.49%
Column drain busy (3rd hit):     43825 ,   1.26%
Time stamp buffer overflow:        137 ,   0.00%
Data buffer overflow:                0 ,   0.00%
Column blocked for readout:      11459 ,   0.33%
Reset after readout:             80256 ,   2.31%
Overall inefficiency:                      4.39%
Pixel hit rate:               222.90 MHz/cm2
*******************************************************
```

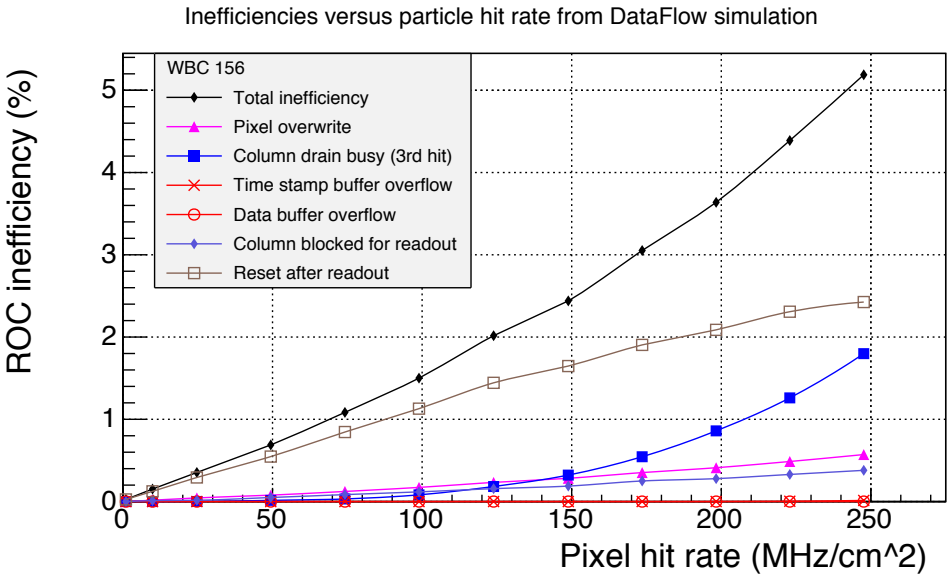

Figure 8.5: **Simulated inefficiency for the upgraded pixel detector**
The readout inefficiencies and random data loss of the PSI46dig chip are simulated. Several sources of data loss can be identified: pixel overwrite, column drain busy, time stamp buffer overflow, data buffer overflow, column blocked for readout and reset after readout. The simulation counts each pixel hit that is added and also counts how many hits are lost due to several reasons. A separate simulation has to be made for each of the different pixel hit rates. The lines between data points are eye guides.

Some changes had to be made to the original code of DataFlow to correctly simulate the behaviour of the PSI46dig readout chip.

The `EventReader` class had to be changed to accept the newly generated hit files for a single ROC. The original code would accept data from the CMS Monte Carlo simulation creating hits in several layers of the detector and on many modules at the same time. The modified code would only see hits on a single readout chip of a single module. Especially the handling of clock cycles without a hit had to be revised.

The changes made to the `DoubleColumn` class were more substantial. The collection of hits from the pixel unit cells to the double column periphery via the column drain mechanism was implemented. This made the simulated pixel hit inefficiency from this source more realistic. Additionally a function to remove hits with expired time stamps from the data buffer was added. This brought the simulated number of lost hits from data buffer overflows and the total number of buffer overflows in accordance with expectations from the chip's theoretical functionality.

An example of the simulated inefficiency with respect to the pixel hit rate the readout chip is subjected to can be seen in figure 8.5. This example simulates the performance in an LHC scenario where the average cluster size is 1.6 and the readout chip is triggered with a random trigger of 100 kHz. The Level 1 trigger latency, or WBC, for this example is 156. This value is very close to the current trigger delay used in the CMS experiment.

8.2.2 Efficiency Simulation and Simulation Validation

To fully validate the simulation, the simulated inefficiencies were compared to results from the laboratory. Since a continuous particle beam with a fixed rate and even particle distribution was not available, all measurements were performed using an X-ray apperatus.

For measuring the efficiency of the PSI46dig readout chip a special measurement method was used. While the X-rays create a stable rate of incoming hits with a fixed cluster size of 1, one pixel at a time in a small fraction of events is activated by the internal calibration pulse of the readout chip. The efficiency is measured by the fraction of events for which this special pixel is activated and found in the readout. During the measurement the trigger is periodic at a fixed rate smaller than 100 kHz. This has a serious impact on the measured inefficiency, since the time between two triggers $t_{\text{trigger gap}} > 10\,\mu\text{s}$ is always larger than the maximum trigger latency of $255 \times 25\,\text{ns} = 6.375\,\mu\text{s}$. Under this condition the reset of the double column after a readout can never be the cause of an inefficient hit.
To compare the measurement from the X-ray test stand with the simulation, the simulation was run under the conditions of a periodic trigger of 1 Hz, what results in only two triggers during the simulated time. This very low trigger rate is done to make the simulation results and the measurement comparable. The resulting comparison plots for two different trigger latency settings of WBC = 200 and WBC = 100 are shown in figure 8.6 and figure 8.7 respectively. Each time panel (a) shows the simulated inefficiency for the PSI46dig readout chip differentiated between the different sources. The second panel (b) shows an overlay of the simulation results and the data from the measurement.

With the longer delay setting of $WBC = 200$ the predominant source of inefficiency is the time stamp buffer overflow. Other mechanisms like the column drain busy or pixel overwrite only contribute little to the hit detection inefficiency, as seen in figure 8.6a. For a smaller setting of the internal delay value of $WBC = 100$, as shown in figure 8.7a, the time stamp buffer overflow does not contribute to the overall inefficiency anymore. The short time between trigger and readout is not long enough to completely fill the time stamp buffers even at the highest rates of simulated X-rays. The most common source for missing hits in the readout are the pixel overwrite and the column drain busy effect. While the pixel overwrite is a constant contributor to the pixel hit inefficiency that is largely unaffected by the WBC setting, a comparison between the $WBC = 100$ and $WBC = 200$ settings shows that with a shorter delay time the column drain inefficiency increases.

The comparison of the simulated and the measured pixel hit efficiency shown in figure 8.6b and figure 8.7b. For the larger delay value of $WBC = 200$ the simulated efficiency follows the measured value very well until a pixel hit rate of $180\,\text{MHz}\,\text{cm}^{-2}$ is reached. Then simulation and measurement diverge, with the simulation overestimating the inefficiency. This is most likely an effect caused by the implementation of the time stamp buffer overflow, since this is the predominant source of inefficiency in the simulation at the concerned pixel hit rates. For the shorter delay of $WBC = 100$ the simulation compared well with the measurements performed in the laboratory up to a pixel hit rate of $75\,\text{MHz}\,\text{cm}^{-2}$.

Since the simulation is more accurate for larger values of WBC the rest of the chapter will concentrate on simulations running at $WBC = 200$.

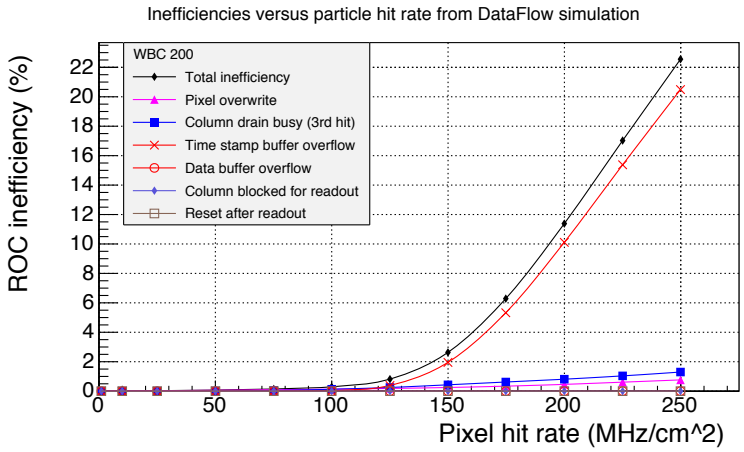

(a) **Readout inefficiency simulation for X-rays at** $WBC = 200$

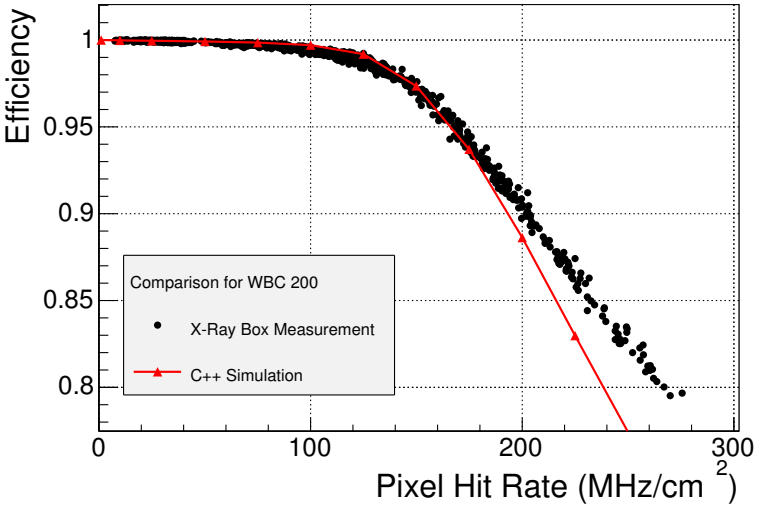

(b) **Comparison between simulation and lab measurement**

Figure 8.6: **Simulation validation for** $WBC = 200$
The simulation is validated against measurements done on the PSI46dig chip inside a X-ray tube. The time stamp buffer overflow is the predominant source of inefficiency for $WBC = 200$ as shown in (a). The simulation and the measurements agree well for low rates, but diverge for larger pixel hit rates.

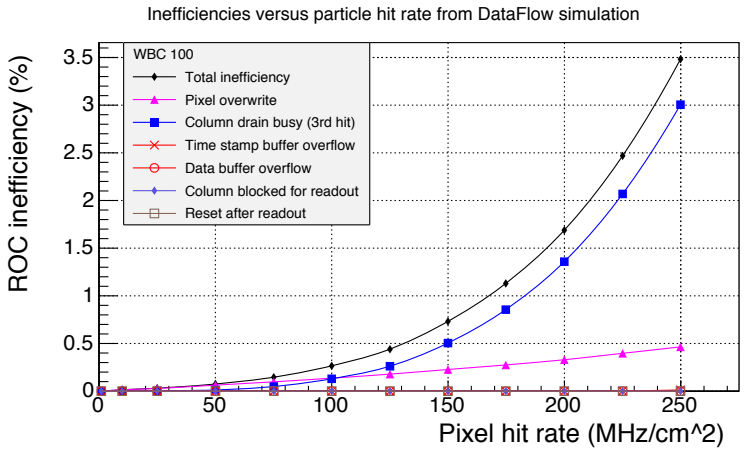

(a) **Readout inefficiency simulation for X-rays at** $WBC = 100$

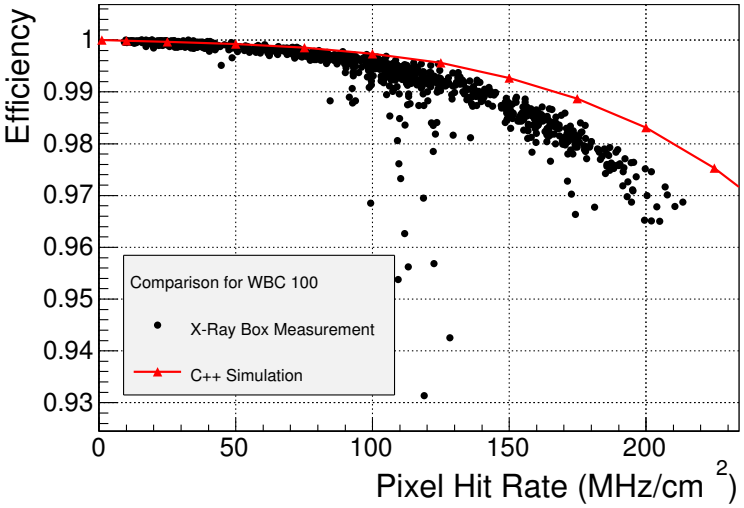

(b) **Comparison between simulation and lab measurement**

Figure 8.7: **Simulation validation for** $WBC = 100$
For the short delay value of $WBC = 100$ the column drain busy effect is the leading cause of random data loss, see (a). The simulation and the measurements agree well up to a pixel hit rate of $75\,\mathrm{MHz\,cm^{-2}}$, but then start to diverge with the simulation underestimating the inefficiency (b).

8.3 High Rate Beam Test Simulation

The High Rate Test Beam performed at Fermilab showed some unexpected results as previously shown in chapter 7. To explain some of the findings the test beam simulation was written. It is based directly on the previously shown DataFlow simulation. While the functionality of the readout chip was directly transferred to the test beam simulation, parts of the program had to be rewritten to simulate features of the test board readout, the telescope setup of eight ROCs and the timing of the beam. Many sources of inefficiency have been implemented into the simulation and their effects can be studied one at a time. The simulation also works as a way to verify the function of the analysis chain described in chapter 7.1.

8.3.1 The High Rate Pixel Telescope Simulation

The simulation of how charge is deposited in the silicon sensors of the High Rate Pixel Telescope described in 8.1 and the verified simulation of the ROC readout mechanism are used to simulate the behaviour of the High Rate Pixel Telescope in the 2014 Fermilab test beam. The program is required to:

- simulate eight readout chip controlled by the RAL test board,
- simulate the variations in the beam current,
- reproduce the periodic trigger conditions from the test beam,
- simulate the phase shift between the 18.3 ns clock of the Fermilab Main Injector and the 25 ns clock cycle of the ROCs (see section 6.3.1),
- simulate the cluster size distribution with very large clusters,
- and simulate bunch crossing shift of hits arriving early/late in a 25 ns clock cycle.

The High Rate Pixel Telescope simulation uses the track collections created in the *Geant4* simulation as input values. A second input are the bunch by bunch beam rate values measured with the QIE device described in section 6.3.1. The particle rate distribution follows exactly the measurements from the test beam and by randomly creating large clusters in the Geant4 simulation the cluster size distribution in the simulation follows the real measurements.

The simulation itself is based on the DataFlow program described earlier, yet some major modifications have been made. The code now simulates eight readout chips. The functionality of the ROCs was directly copied from the DataFlow simulation. The Module and TBM classes have been removed and their functionalities of controlling and relaying triggers and readout tokens have been replaced by a `Testboard` class. While the test board, like in the real test beam setup, replaces most features of the TBM there is one large difference. The delay between a trigger to the ROCs connected to a TBM is fixed and only of the order of five clock cycles (225 ns). In the test beam setup this delay is variable and larger values were used. This feature was also added to the simulation of the test board functions. When simulating a certain run number, the trigger delay values are read from a database to correctly replicate the conditions of data taking.

To simulate the phase shift between the Fermilab Main Injector clock and the ROC clock, the HRPT simulation runs on a 18.3 ns clock. Every cycle of the simulation is a new 18.3 ns long bunch of the simulated beam. With every new cycle of the simulation new hits are added to the eight simulated readout chips. The clock of the test board and all ROCs is only

advanced after 25 ns have passed. The arrival time of hits on a ROCs is modified by the time of flight of a proton at the speed of light moving through the eight telescope planes, creating the track.

Just like in the real experiment, a trigger signal is sent at a fixed time during the simulated Main Injector turn. This simulates the periodic trigger of 92.4 kHz. The exact bunch the trigger is sent on is again read from the recorded run data from the 2014 Fermilab beam test. The number of triggers is used to control the running time of the simulation. During a single simulation run exactly 369.000 readout triggers are sent to the simulated readout chips.

Laboratory measurements show that the PSI46dig readout chip is not fully efficient over the full 25 ns clock cycle which the readout logic is running on [Pit15]. Only a narrow time window of 11 ns remains in which all occurring hits are detected in the correct bunch crossing. The hit is not lost if it occurs outside of this time window, but is either detected in the previous or the following bunch crossing. In the simulation the exact arrival time of a hit is known. This information is used to move a hit one bunch crossing up or down if it arrived outside the 11 ns-window.

8.3.2 Sources Of Inefficiency

With the simulation of the High Rate Pixel Telescope in place and all identified possible sources of inefficiency added to the simulation it is possible to evaluate their individual influence on the inefficiency measured in the beam test. The possible sources were identified to be:

- ROC readout inefficiency,
- Misalignment of telescope plane,
- Bunch crossing shift of hits,
- 'Monster' clusters,
- Large beam rate variations,

In order to determine the ROC's readout inefficiency all of these sources were controlled in the simulation.

ROC Readout Inefficiency

The original goal of the High Rate Beam Test was to measure the ROC readout inefficiency of the PSI46dig. In section 8.2.1 it was shown that the DataFlow simulation accurately reproduces the readout inefficiencies by counting inefficient hits up to a rate of 175 MHz cm^{-2}. What remains to be seen is whether the analysis framework that relies on track counting comes to the same conclusion.

To study the behaviour of the simulated readout inefficiency and the analysis framework a simulation with special running conditions was created. In *Geant4* a set of tracks was created that does not have random large clusters attached. Additionally all readout chips are perfectly aligned with each other, placing the same pixels from all telescopes behind each other in the path of simulated primary proton. In the telescope simulation all hits are associated with the 25 ns in which they arrive. To avoid the large variations in particle rates from bunch to bunch, the feature of reading QIE data has been disabled. Instead the pixel hit rate changes slowly over the course of the 180,000 simulated Main Injector turns. This

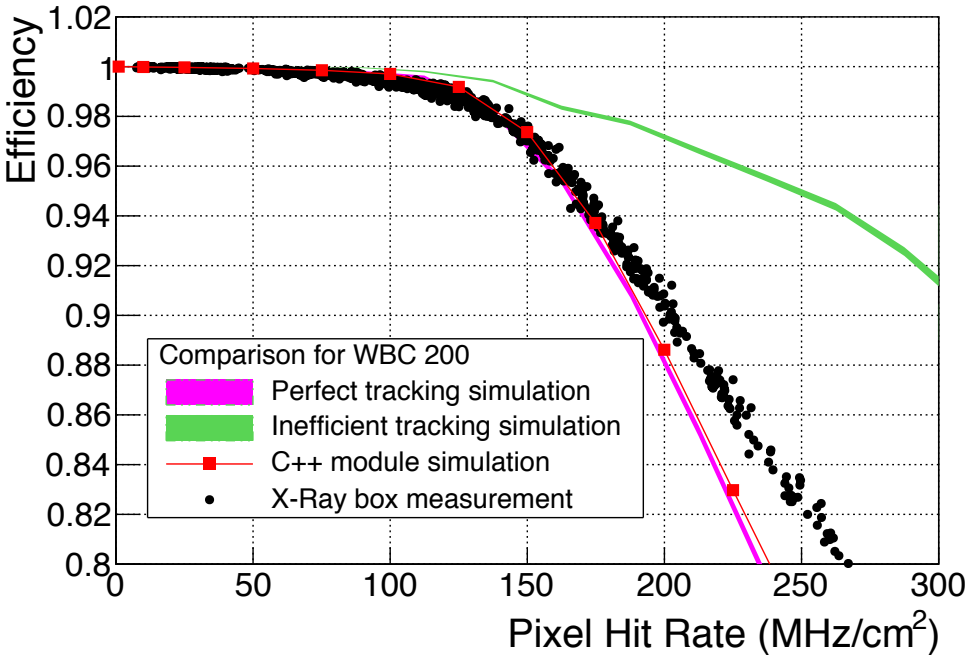

Figure 8.8: **Comparison of pure C++ simulation, X-ray measurements and telescope simulations**
The figure compares pixel hit efficiency from the original C++ simulation of the readout chip, as already shown in 8.6a, with the X-ray measurements and the results from the perfect tracking telescope and the inefficient tracking telescope. The perfect tracking telescope is a simulation with seven simulated pixel chip planes that do not experience any readout inefficiencies, while the eighth plane of the simulated telescope, the DUT, is inefficient. The efficiency is measured by matching hits on the DUT to tracks found in the seven perfect planes. The reconstructed efficiency from the perfect tracking telescope matches very well with the results obtained by hit counting from the original C++ module simulation. The inefficient tracking telescope is modelled after the real High Rate Pixel Telescope. All eight planes are made from the same inefficient readout chips. Due to the correlation between the tracking planes and the DUT the reconstructed efficiency is overestimated compared to the real value given by the C++ simulation.

means a large range of particle flux is covered, while a well defined flux can be assigned to each triggered event. The simulated pixel hit rate ranges from 0 MHz/cm^2 to up to 400 MHz/cm^2. The only remaining simulated process reducing the hit efficiency is the ROC readout itself.

To be able to compare the results from the simulation with the measurement in from the X-ray test stand, the charge sharing between pixels was disabled. The average cluster size for the simulated hits is 1.01. This value is very close to the one pixel clusters created by the X-rays. The periodic trigger in the telescope simulation, and thus the long time between two triggers, again suppresses the inefficiency from the readout reset. The comparison to the simulated hit efficiency of a single ROC, that was obtained from the original readout simulation and shown in figure 8.6, is made in figure 8.8. Two different designs for a particle tracking telescope and its device under test are simulated. In the first design the DUT and the telescope are separate devices. The telescope is assumed to have no inefficiencies for tracking particles, while the DUT has inefficiencies. In the plot this is referred to as 'Perfect tracking simulation'. In the second design all planes of the tracking telescope and the DUT are built from the same front-end readout electronics. As a consequence all telescope planes show similar inefficiencies. This is referred to as 'Inefficient tracking simulation' and simulates the measurement case from the High Rate Pixel Telescope.

The result for the perfect tracking simulation shows that if the number of hits on the DUT is known well enough, the two approaches of hit counting in the simulation and track matching in the measurement are on par. The result for the perfect tracking telescope follows the simulated rate dependence of the single ROC efficiency very well, for the inefficient tracking simulation this is not the case. The efficiency measured by track matching for a telescope of eight equally inefficient readout chips is generally higher than for the perfect tracking simulation. This effect is due to the high correlation of the ROC readout inefficiencies of all eight ROCs of the telescope. The efficiency of a hit, whether it is read out or not, in the PSI46dig readout chip is dependent on the buffer status when the hit occurred on the ROC and the number of hits that arrive until the hit is read out. By having the ROCs perfectly aligned, and the simulation creating almost straight tracks, double columns placed behind each other all experience the same number and sequence of hits. Hits created by the same track tend to be inefficient in all ROCs simultaneously. Entire tracks disappear due to the ROC inefficiency and do not contribute towards the track matching based efficiency measurement, thus increasing the measured efficiency. This perfect correlation between sensor planes is an effect of the simulation but can also happen to a lesser extend in the measurement.

Charge Sharing

In the simulation case of the previous paragraph the simulated tracks created only clusters with a very small cluster size in every telescope plane. For a telescope equipped with the CMS silicon pixel sensor, even with its planes positioned orthogonally to the incident particle beam, the measured average cluster size > 1 due to the diffusion of charge carriers in the sensor material. With the simple charge sharing mechanism activated in the creation of Geant4 tracks, the average cluster size for the simulation rises to 1.2. The larger clusters have an influence on the measured efficiency in the two telescope simulation cases. In figure 8.15 it is shown that the measured efficiency of the DUT increases for a larger average cluster size. Clusters are spread over double column borders. Even if one part of the cluster is inefficient, it is not completely lost. In the data analysis the hit can still be matched to its track in the perfect tracking telescope.

The same effect can be observed in the inefficient tracking telescope, although to a smaller

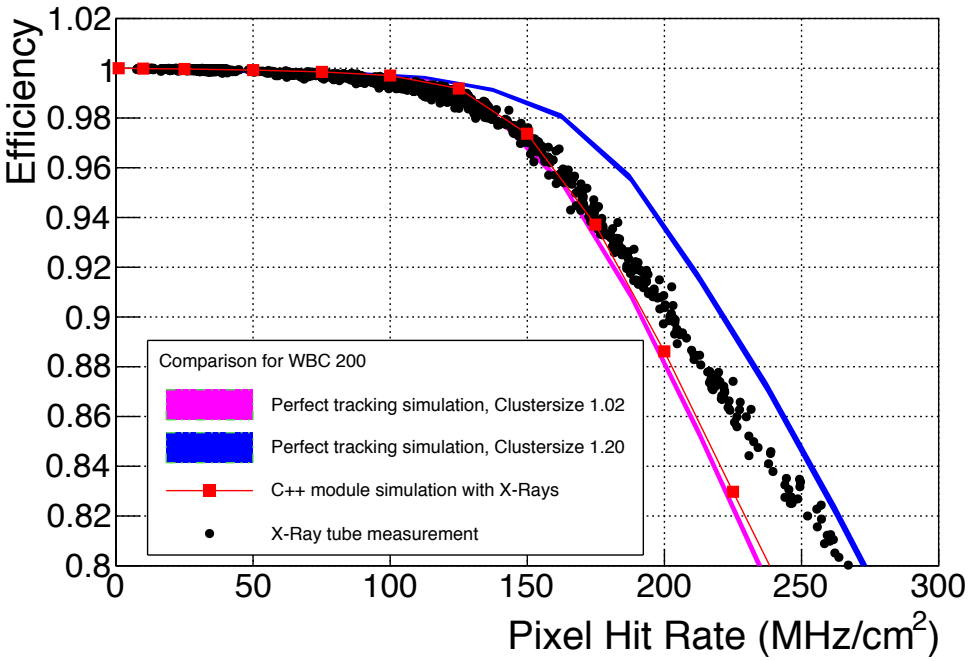

Figure 8.9: **Simulated readout efficiency with corrected cluster size** After a simple charge sharing mechanism was introduced in the simulation, the average cluster size increased from 1.02 to 1.20. The increased average cluster size leads to a higher measured readout efficiency when the track based hit matching algorithm is used. As shown for the example of the perfect tracking telescope, the measured inefficiency decreases by 50%.

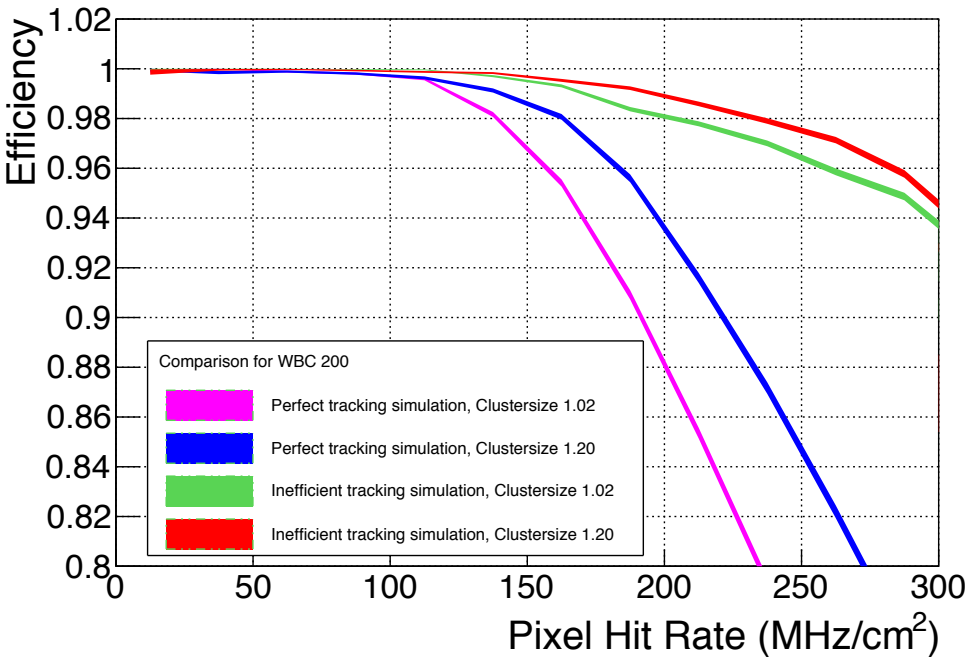

Figure 8.10: **Simulated readout efficiency with corrected cluster size** Like for the perfect tracking telescope, the measured efficiency for the inefficient tracking telescope increases with a larger average cluster size.

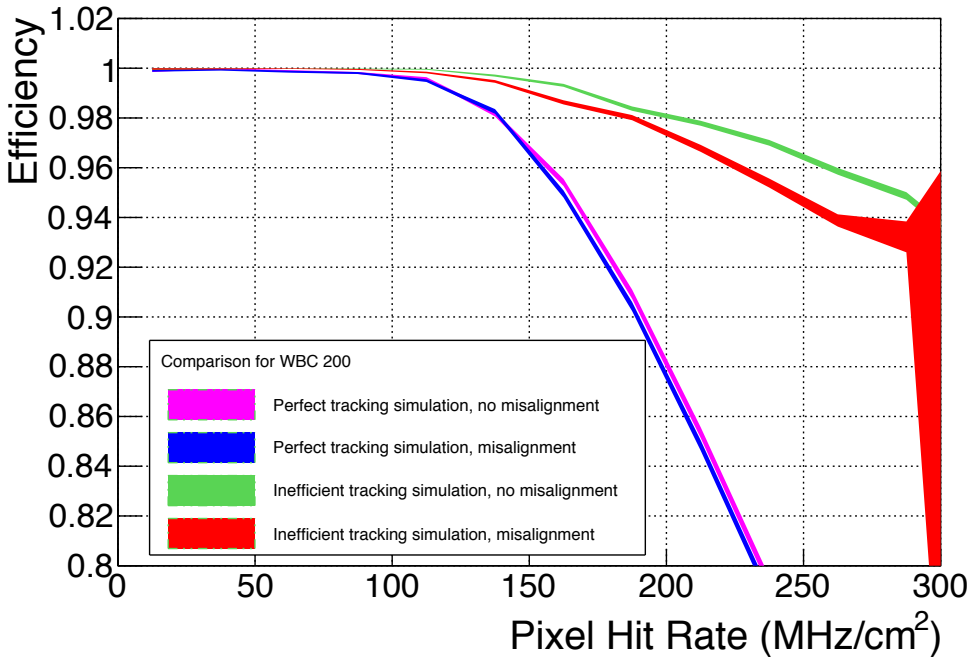

Figure 8.11: **Effect of misalignment on reconstructed efficiency, cluster size 1.02**
No charge sharing has been simulated in the pixel telescope. For the perfect tracking telescope the effect of misaligning the telescope planes is minimal. This is a good cross check for the alignment algorithm of the analysis chain, see section 7.2.4. For the inefficient tracking telescope the reconstructed efficiency decreases. This is a desired effect, since the measurement moves closer to the expectation (perfect tracking telescope). However, the effect is smaller than originally anticipated when the High Rate Pixel Telescope was designed.

degree (the corresponding simulation result can be seen in figure 8.10). The larger cluster size increases the measured efficiency by about 1% over what would be expected by only single pixel hit clusters.

Misalignment

In reality, including the High Rate Beam Test, the misalignment of detector planes reduces the correlation of double column inefficiencies between hits in different telescope planes. By implementing this in the simulation a particle does not pass through the same pixels and double columns on all ROCs of the telescope. This was the original idea for the High Rate Pixel Telescope to be able to measure the PSI46dig readout inefficiencies. In figures 8.11 and 8.12 this theory has been put to the test. Figure 8.11 compares the measured efficiencies for runs with a small average cluster size of 1, while figure 8.12 compares efficiency simulation results for an average cluster size of 1.2. The first thing to notice is that in both cases the alignment step of the analysis process works. For the perfect tracking telescope only a very small difference between the aligned and misaligned telescopes can be seen. For the inefficient tracking telescope, however, the measured efficiency for the simulation case of the misaligned telescope planes is smaller. Not all correlations between hits of the same track have been removed. Double columns are still placed behind each other, always showing a very similar

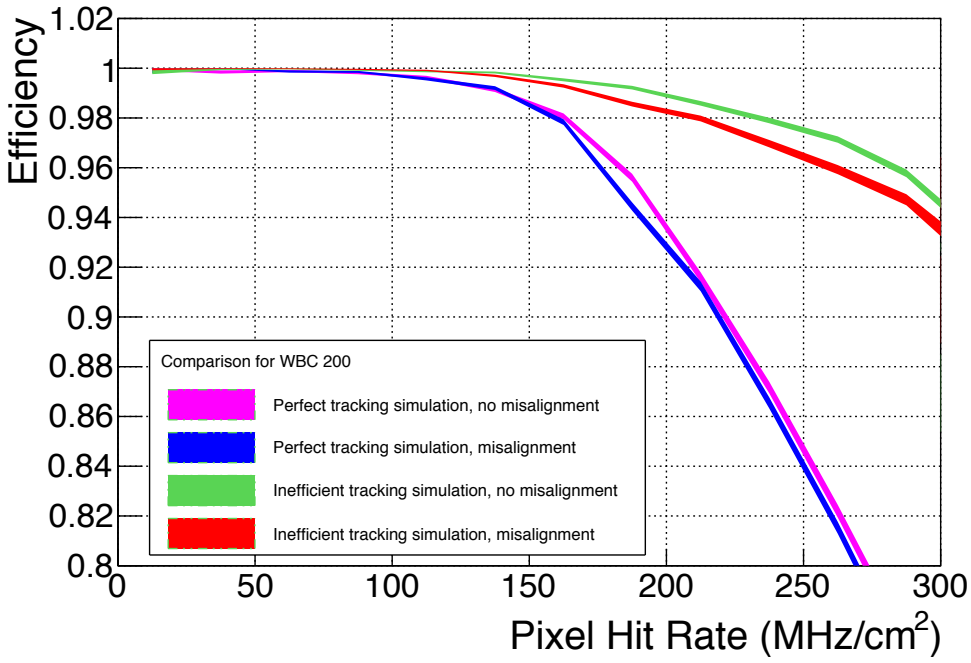

Figure 8.12: **Effect of misalignment on reconstructed efficiency, cluster size 1.20**
Also with a realistic cluster size distribution the misalignment cannot fully remove the correlations between the separate telescope planes. The reconstructed efficiency for the inefficient tracking telescope still overestimates the real value.

hit pattern created by the straight tracks simulated in *Geant4*.

The simulation confirms that the correct way to measure the hit efficiency is to decouple the hits on the tracking telescope planes from the hits on the DUT. This is usually done by using different types of readout electronics like in the EUDET telescope [Rub12]. In the case of the High Rate Pixel Telescope this was not possible since only few other pixel detectors, like ATLAS pixel detector based on the FEI4 chip [Bar11], or strip detector systems exist, that provide the needed high rate capability, radiation hardness and position resolution. The conclusion can be drawn, that the originally made assumption that the misalignment between the chips would de-correlate the inefficiencies was overestimated. This results in a reduced sensitivity of the measurement on the random data loss in the PSI46dig readout chip.

Clock mismatch and bunch crossing shift of hits

Due to the clock mismatch between the Fermilab accelerator and the readout chip in the 2014 High Rate Test Beam, hits can occur at any time during the 25 ns clock cycle of the ROC readout. With the readout chip only fully efficient in a small time window, this effect was identified as a potential additional source of inefficiency in the real test beam.

To study the effect of this inefficiency source, the simulation was perfomed in which the ROC readout inefficiency and the clock mismatch are the only activated sources of inefficiency. Tracks from *Geant4* do not have 'monster' clusters and all 8 ROCs are perfectly aligned. The simulation result for WBC = 200 and a uniform particle rate over time can be seen in figure 8.13 and also in figure 8.14. The simulation with the clock mismatch shows an overall 2% lower efficiency than the simulation without clock mismatch. Yet the curve of the simulated

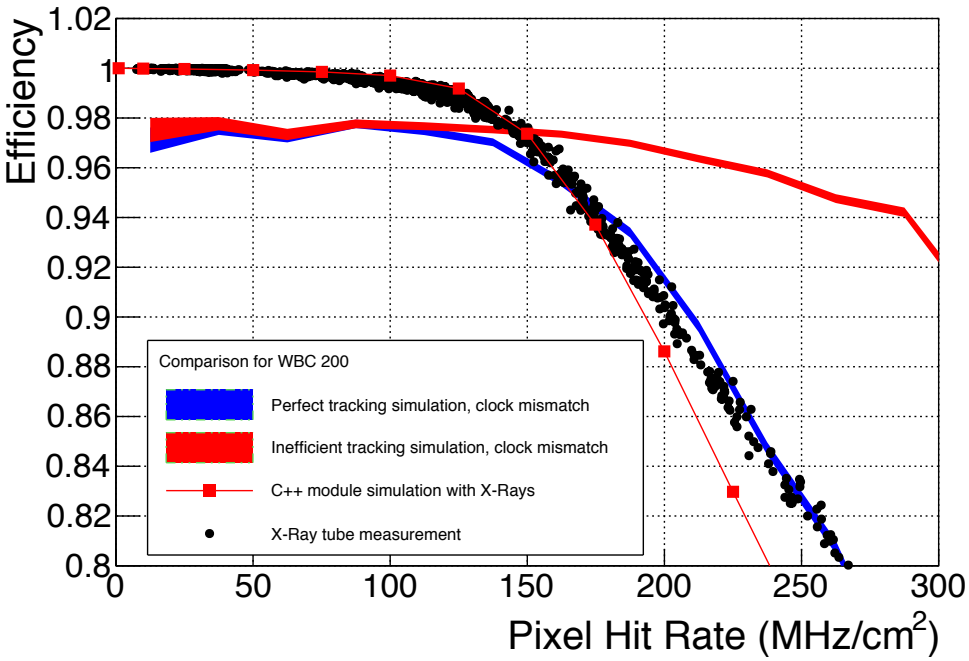

Figure 8.13: **Effect of clock mismatch between Main Injector and ROC** The reconstructed efficiency from the telescope simulations with the clock mismatch between Main Injector and ROC clock is compared to the theoretical expectations, represented by the X-ray measurements and C++ simulation. With the clock mismatch simulated telescopes do not reach the full 100% for small pixel hit rates. This effect was also observed in the real measurements.

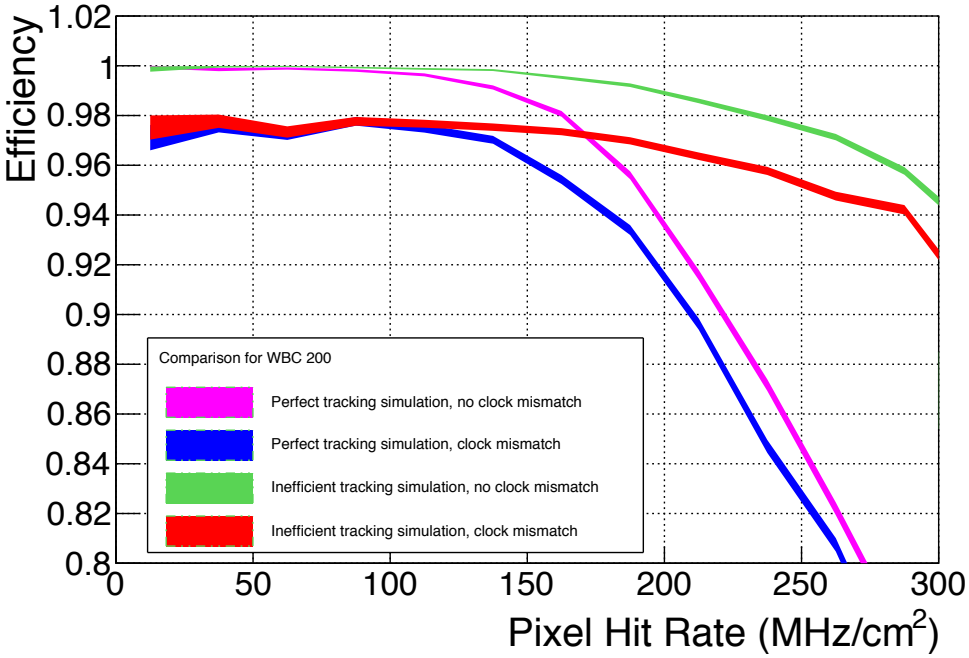

Figure 8.14: **Effect of clock mismatch between Main Injector and ROC** The activated clock mismatch reduces the reconstructed efficiency measured by track matching by 2% for the perfect and the inefficient tracking telescope.

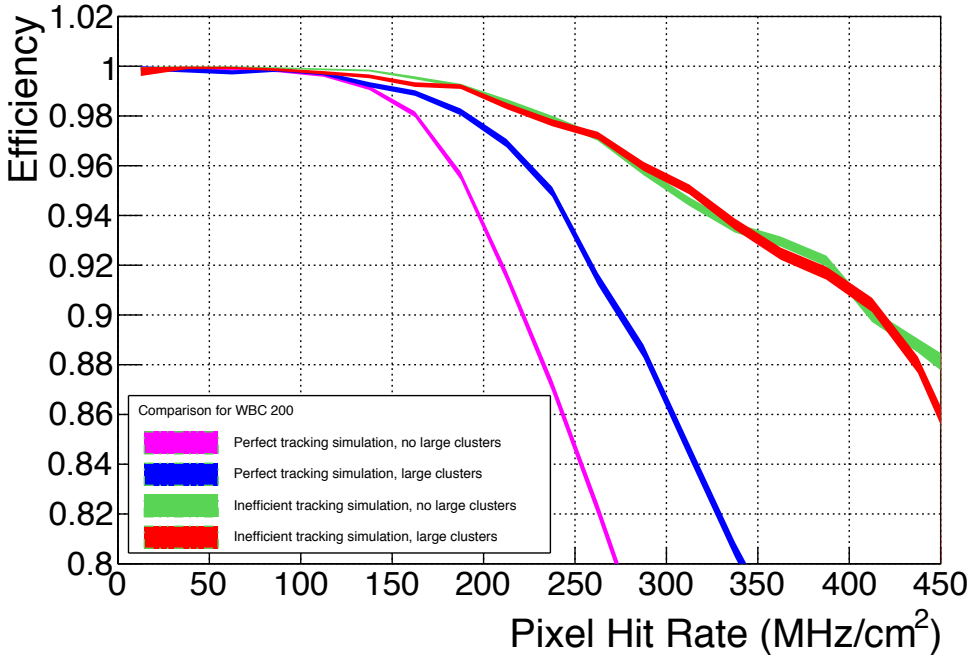

Figure 8.15: **Effect of monster clusters**
When plotted against the number of pixel hits, the addition of very large clusters, or 'monster clusters', to the simulation has no effect in the inefficient tracking telescope. For the perfect tracking telescope simulation the addition of monster clusters increases the reconstructed efficiency, as larger clusters are less likely to be fully inefficient. A hit can still be reconstructed and matched to a track.

efficiency still follows the same slope as observed in the laboratory measurement with X-rays. Even for very low pixel hit rates on the readout chips the track efficiency does not reach 100%. The exact same behaviour was seen in the measurements from the 2014 Fermilab test beam, see section 7.4.2.

'Monster' clusters

As another potential source of inefficiency, the very large clusters, also called 'monster' clusters, were identified. No detailed studies have been made so far on how the ROC readout efficiency behaves with frequent spikes in occupancy of a single or several readout chips. The simulation case for the monster clusters is again different from the cases discussed before. The simulated ROCs' readout inefficiency is activated, but the ROCs are not misaligned to each other. Also the clock mismatch and bunch crossing shift are disabled. The only change to the nominal simulation is the addition of large clusters.

The simulation results of the perfect tracking simulation in figure 8.15 shows that a larger cluster size of hits on the Device Under Test increases the tracking efficiency with respect to the same number of pixels hit per time. This makes sense, as larger clusters are less likely to be fully inefficient as they are spread over several double columns. At the same time the effect of the larger clusters does not improve the tracking efficiency on the simulated telescope made from eight inefficient readout chips.

In the real beam test experiment the number of hits per bunch crossing on the telescope cannot be measured. Only in the simulation is it possible to correctly count the number of

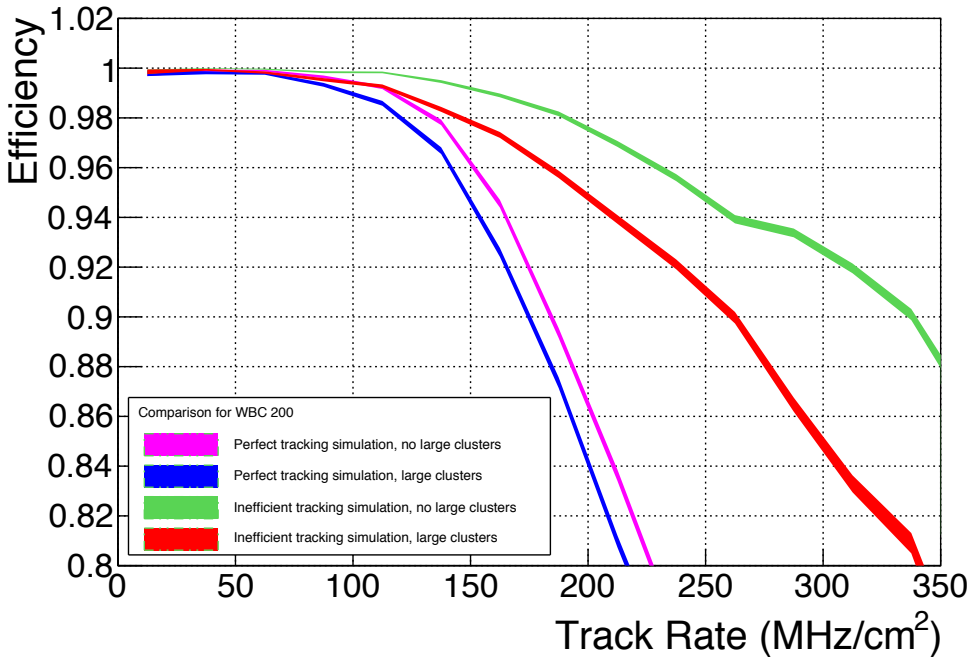

Figure 8.16: **Effect of monster clusters**
When measured against the track rate instead of the pixel hit rate, the 'monter clusters' decrease the reconstructed efficiency for both, the perfect tracking telescope simulation and the inefficient tracking telescope simulation. The high occupancy on the readout chips created by the large clusters created spikes in the fill levels of the data buffers, effectively causing them to overflow and erasing triggered on data in the process. Also the longer readout time of events with high occupancy blocks the double column, during which no new hits are accepted.

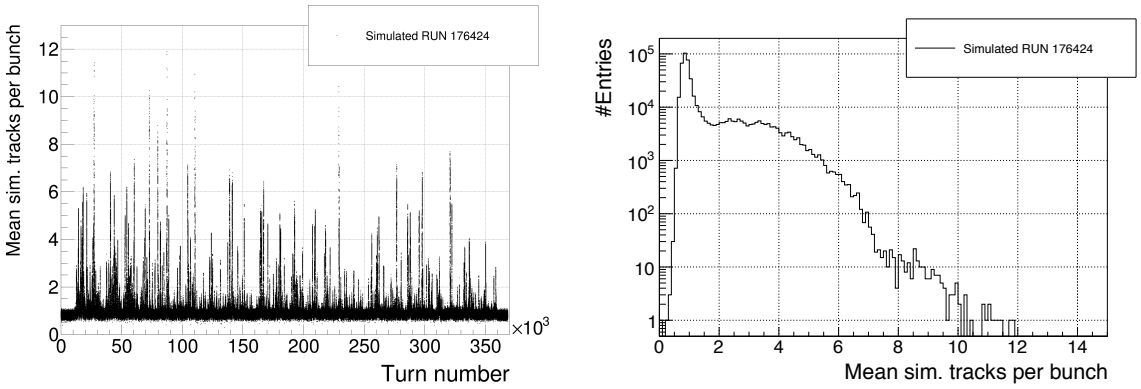

(a) **Average number of tracks per simulated turn**

(b) **Distribution of average number of tracks per simulated turn**

Figure 8.17: **Average number of tracks per simulated turn**
Each turn of the Fermilab Main Injector has 588 bunches. For each of the 369,000 turns of a single extraction the averaged number of protons per bunch has been calculated as it was measured by the QIE device, see section 6.3.2 and section 7.2.8, and plotted in figure (a). Simultaneously the distribution over all turn is shown in figure (b). The example plots demonstrate well the large variations in the beam on a turn-by-turn basis. Measurements from the QIE device also show that the variations are equally large on a bunch-by-bunch basis.

pixel hits the DUT receives with each bunch crossing. Hence the rate of hits in the test beam has to be estimated from the number of particles passing through the telescope, a parameter measured by the QIE device in the real experiment. To later directly compare the simulation results with the measurements performed at Fermilab the efficiency is evaluated against the rate of particles or tracks through the High Rate Particle Telescope. In the simulation the number of tracks is well known for every bunch of the beam and also for every 25 ns clock cycle of the simulated telescope readout. The influence of the random large clusters on the beam test results can be studied by evaluating the efficiency of matching a hit on the DUT to a track found in the seven tracking planes against the track rate. The simulation result is shown in figure 8.16. When plotting the efficiency over the rate of tracks the efficiency is generally smaller after introducing large clusters to the simulation. The random large clusters, with up to 30 pixels per double column, create sudden spikes in the fill status of the data buffer, causing it to overflow and reset the double column periphery. In this process the hits triggered on are lost. At the same time the large number of hits in a double column can block the readout for a long time: draining the hit information of a single pixel hit from the pixel unit cell to the periphery takes 50 ns and while a pixel is waiting to be drained hits occurring on the same pixel are lost, contributing to the measured inefficiency. This decrease of hit efficiency can be seen in the perfect tracking telescope simulation as well as in the inefficient tracking telescope simulation.

Large beam rate variations

One of the biggest difficulties in the High Rate Beam Test at Fermilab in 2014 was the large variations in the beam intensity on a bunch-by-bunch basis. In the previously shown simulations the beam rate is constant throughout every turn of the Fermilab Main Injector,

with the number of tracks per bunch following a Poisson distribution with the simulated rate as its mean value. In the beam test the number of particles in each beam bunch were less deterministic and had larger variations. This complicates assigning a particle hit rate to a certain time interval and thus makes the efficiency measurement harder.

To study the influence of large beam variations on the simulated inefficiency run 176424 was chosen. This run was executed under the same conditions for WBC and the readout token delay as in the simulations shown previously without large beam variations. The rate variations measured by the QIE device during the run are used as input for the simulation. In a first step the large variations in the beam current on a bunch-by-bunch basis have been averaged out over the 588 bunches of a Fermilab Main Injector turn. For every turn of the simulation the number of protons measured in the Fermilab test beam are determined and a turn average is calculated. The number of tracks added to the simulation for every bunch of the turn follows a Poisson distribution with the turn average as its mean value. The average number of tracks for each turn, determined from the simulation, can be seen in figure 8.17b. While the majority of turns are in the low range of one track per 18.3 ns bunch, which corresponds to $\approx 55\,\mathrm{MHz\,cm^{-2}}$, the values go up to an average of 12 tracks per bucket, which is close to $650\,\mathrm{MHz\,cm^{-2}}$.

The large rate variations have drastic influence on the simulated inefficiency as shown in figures 8.18. For the perfect tracking telescope simulation it can be seen that the variations in the beam structure reduce the simulated readout efficiency greatly. Even for low pixel hit rates or track rates the efficiency does not reach the full 100%. Especially for very low rates the measured efficiency is drastically reduced, a feature that was also observed in the real test beam analysis. Although the same range of pixel hit rates is covered in the two simulation (with large rate variations and with constant rates over each turn) the inefficiencies creating the loss in tracking efficiency are quite different. With the full control over the readout in the simulated telescope it is possible to identify sources of inefficiency like the high occupancy of time stamp buffers and data buffers, as shown in figure 8.19. In the simulation with a stable beam rate the most dominant source of inefficiency by far is the time stamp buffer overflow due to the constant creation of new pixel hits on the readout chips. With an unstable beam rate this is not the case anymore: the short bursts of many particle hits during a few clock cycles of the readout chip make the data buffer overflow and the busy column drain mechanism more prominent sources of inefficiency.

8.3.3 Full beam test simulation

The last step of the simulation is to combine the inefficiency sources described in the previous section in a single simulation run. This brings the readout inefficiencies together with the effects of the timing mismatch between the Fermilab accelerator clock and the readout clock and the large clusters. In figure 8.20 the simulation results for the inefficient tracking telescope and the perfect tracking telescope are shown. The results from the simulation with only the ROC inefficiencies activated are compared to the results of a simulation with all possible sources of inefficiency.

The first thing to note in figure 8.20 is that neither the inefficient tracking telescope nor the perfect tracking telescope reach 100% efficiency in matching the reconstructed tracks to hits on the DUT. This can be attributed to the phase mismatch of the two clocks in the system as described previously. Again the reconstructed efficiency is higher for the inefficient tracking telescope, which was attributed to lost tracks from a correlation between double columns. Although a random misalignment in the order of $\pm 300\,\mu\mathrm{m}$ in the x- and y-axis

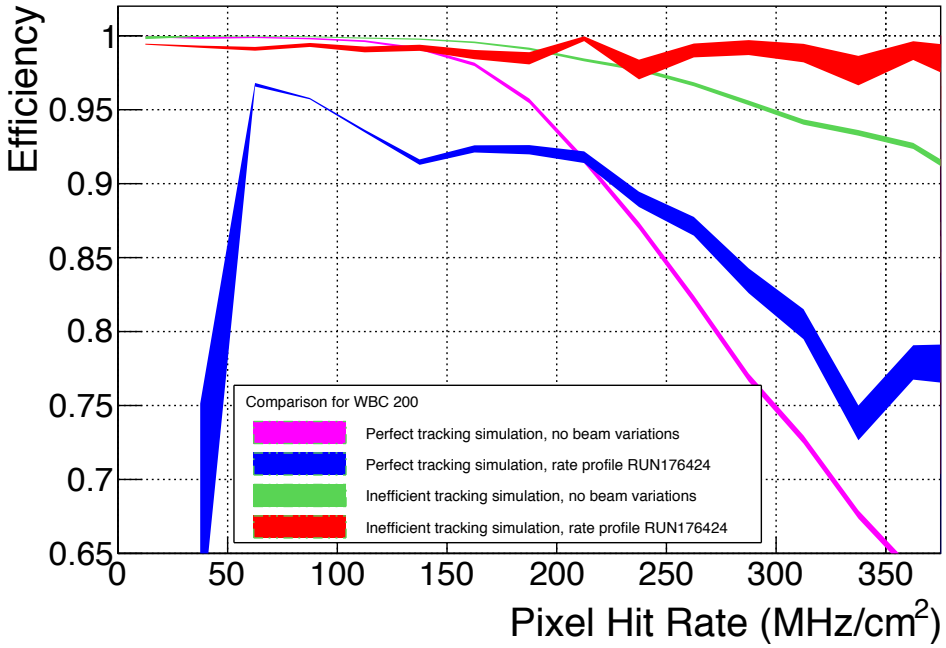

Figure 8.18: **Effects of large beam variations**
A comparison between a simulation with stable beam conditions and a simulation with large beam variations is made for the perfect tracking telescope simulation and the inefficient tracking telescope. For both telescope cases the large beam variations result in a reduced starting value for low rates. The first point of the perfect tracking simulation is skewed due to low statistics and should be ignored. The large beam variations result in a less steep decrease of efficiency. The measured curves for both telescopes flatten out. This change in behaviour was created by a change in the predominant inefficiency source, see figure 8.19. At the same time the uncertainty on the measured efficiency increases (width of drawn band).

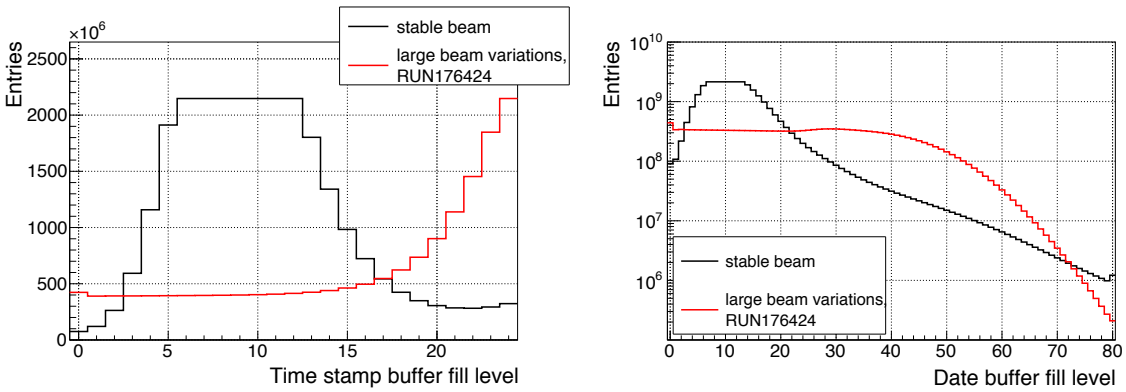

(a) **Time stamp buffer fill level** (b) **Data buffer fill level**

Figure 8.19: **Buffer level comparison**
For different beam conditions also the way the buffers in the PSI46dig readout chip are filled changes. For stable beam conditions the data buffer overflow is the predominant source of inefficiency. This can be seen from figure 8.19b, the buffer creates an overflow when it reaches a value of 80. For the large beam variations the time stamp buffer overflow is much more common, as seen in figure 8.19a. Large spikes in the number of average particles per turn create many hits in consecutive events that easily fill the 24 cells deep buffer.

and a rotational misalignment of $\pm 0.8°$ has been simulated for all detector planes, a high correlation between the double columns hit by the straight particle tracks still reduces the overall number of tracks found in the reconstruction introducing a bias in the efficiency measurement. Comparing the dataset created from the QIE profile of RUN 176422 with all other inefficiencies included with the data set created from a flat hit rate distribution and only the ROC internal inefficiency included, one can also see that the reconstructed efficiency from the perfect tracking telescope is distorted. The high fluctuations in the number of protons in the beam create a large uncertainty on the flux assigned to every event, introducing a large distortion on the measured efficiency vs. pixel hit rate curve. This reduces the overall reconstructed inefficiency and also influences the slope of measured curve.

The full test beam simulation compared to the measurements done during the 2014 Fermilab beam test is shown in figure 8.21. To make the two reconstructed efficiencies comparable, the measured flux from the test beam measurement was converted to an average pixel hit rate, by multiplying the particle flux with the average cluster size $< CS >= 1.6$ for the straight telescope. Additionally the large errors for the first point of the simulation have been removed to make the plot more clear.

At low rates simulation and measurement converge to the same value. This value $< 100\%$ efficiency has been seen in all beam test measurements. The simulation is also able to reproduce the less steep slope of the reconstructed efficiency at higher pixel hit rates. This effect was attributed to the inefficiencies in the double columns of the telescopes being highly correlated together with the large beam intensity variations.

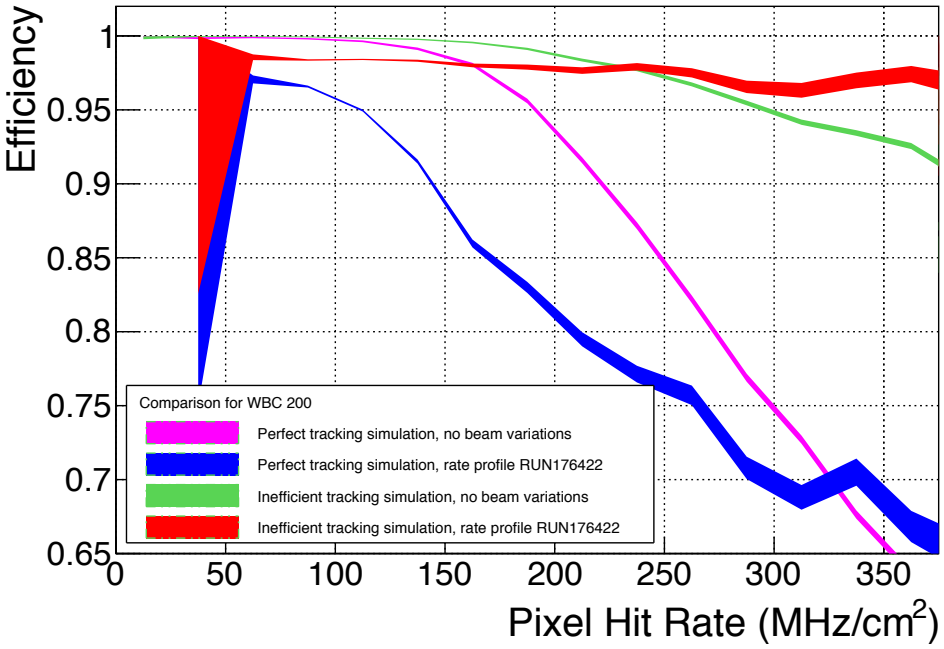

Figure 8.20: **Full beam test simulation**
This plot compares the results of the telescope simulation with only the ROC inefficiency added to the outcome of the simulation will all possible sources of inefficiency combined. The effect of the mismatching clocks between Main Injector and ROC is clearly visible from the reduced starting efficiency. The starting values for the full test beam simulation have large error bars and should be ignored. All previously discussed effects of the reconstructed efficiency flattening out due to the large beam variations and also the the larger uncertainty on the efficiency measurement can be identified in this plot.

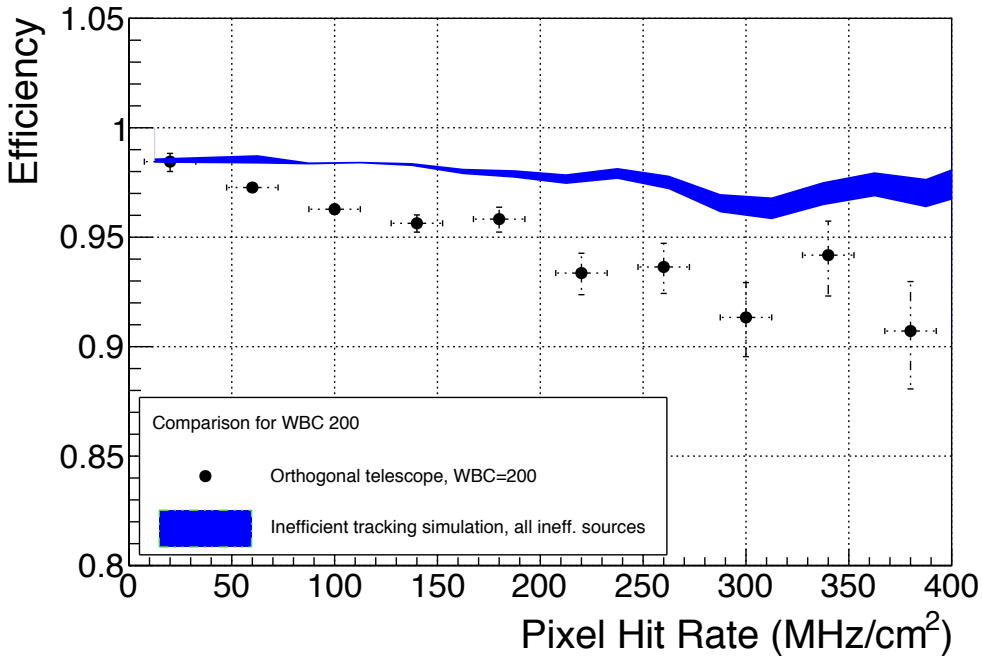

Figure 8.21: **Comparison of measurement and simulation**
Measurements from the Fermilab beam test are compared to the full simulation with all inefficiency sources added. Both curves do not start at 100%. This effect can clearly be attributed to the mismatch between Fermilab Main Injector clock and ROC clock. Both curves show a less steep decrease in efficiency towards higher pixel hit rates than expected from X-ray measurements. This effect is caused by the high correlation between the inefficiencies of double columns in the telescope and the irregular beam rate on a turn-by-turn and bunch-by-bunch basis.

8.4 Conclusions

The simulation of the PSI46dig readout chip is able to accurately describe the flow of data in the chip and to estimate the rate of random data loss the chip experiences under a wide range of conditions. It can be used to predict the chip's efficiency in the CMS experiment, but it is also possible to extend this pure readout chip simulation to a full simulation of the High Rate Pixel Telescope. Several effects that contribute to the efficiency reconstructed in the telescope setup have been implemented and studied. The effect of higher efficiency for larger WBC values could not be reproduced by simulation. The mismatch between the Fermilab accelerator clock and the ROC clock has been found as the reason for why the measurements never reach the full efficiency of 100% for low pixel hit rates. The beam particle rate variations, the large clusters and the DUT not being decoupled from the telescope are the reason for the limited decrease in measured data loss for larger pixel hit rates. This greatly reduced the sensitivity of the efficiency measurement.

Within the sensitivity limits of the experiment the PSI46dig readout chip was shown to have a dynamic inefficiency compatible with specifications.

Chapter 9

Summary and Recomendations For Future Beam Tests

The innermost part of the CMS experiment is the CMS Pixel detector. The currently installed detector will be replaced and upgraded at the end of the year 2016. Two generations of pixelated detectors have been studied in the scope of this work. The first detector was based on the PSI46v2 readout chip, that is currently installed in the CMS Pixel detector. A new use case for the hybrid pixel detector assemblies based on this readout chip were found in the Pixel Luminosity Telescope.

For the upgrade of the CMS Pixel detector a new readout chip was designed. The PSI46dig chip can be described as an evolutionary step further from its predecessor. The number of changes introduced was kept to a minimum, while at the same time the readout chip had to fulfil all the requirements posed by the strong performance of the LHC. A beam telescope was designed to study the behaviour of the new readout chip under LHC-like conditions. A full simulation of the beam telescope and the beam environment was written to explain unexpected features found in these measurements.

9.1 Pixel Luminosity Telescope

The Pixel Luminosity Telescope (PLT) is a new luminometer for the CMS experiment. It is based on 16 small angle particle tracking telescope placed on both ends of CMS. Each of the telescopes is built from three planes of pixelated particle detectors using the PSI46v2 readout chip and the standard n-in-n type CMS silicon pixel sensor. Based on the same readout architecture as the CMS Pixel detector, the PLT uses the fast cluster counting signal, or Fast-OR signal, of the readout chip to measure the number of particles passing through a telescope in every given 25 ns bunch crossing. Each plane of a telescope creates its own Fast-OR signal. In the backend electronics a coincidence is created from three planes of a telescope at a 40 MHz rate. At the same time the pixel hit position data can be read out with up to 100 kHz trigger rate.

In the scope of the thesis at hand a new in-situ calibration method for the pixel thresholds was developed. The response of the pixel to a charge deposited in the sensor material is zero-suppressed. Only signals passing a threshold that is set for every pixel separately are acknowledged by the readout chip. Variations during the production process of the silicon ASIC chip result in a large variation of pixel thresholds across a readout chip and also from chip to chip. By using a readout chip internal calibration pulse, two settable voltage registers in the readout chip and a voltage divider in each pixel unit cell the presented calibration algorithm unifies the thresholds on all readout chips of the Pixel Luminosity Telescope. The results of this calibration show that the calibration is successful and a narrow threshold distribution is achieved.

The way in which the PLT uses zero-counting to measure the luminosity provided by the LHC to the CMS experiment is shown and it is explained why a Van-der-Meer scan is necessary to obtain an absolute calibration on the measured luminosity. First measurements done by the PLT are presented, that the luminosity values obtained by the PLT match well with what is seen by the already established luminometers, the Hadron Forward Calorimeter and the Beam Condition Monitors.

9.2 High Rate Beam Test

For the Phase 1 Upgrade of the CMS Pixel detector a new readout chip, the PSI46dig, was developed. This new chip is based on the original PSI46v2 ROC but contains a series of improvements. The buffers in the pixel periphery have been increased from 12 to 24 cells for the time stamps and from 32 to 80 cells for the pixel hit data. An additional readout FIFO has been introduced that holds hit information until an external readout token arrives at the chip. The biggest changes were made to the output format of the data. While the PSI46v2 chip encodes the pixel hit address in analogue output levels and also transmits the measured pulse height of a pixel as an analogue voltage level, the output of the PSI46dig readout chip is fully digital. The data output is converted to a binary data stream, with the measured pulse height expressed in the levels of an 8-bit ADC.

To test the newly designed readout chip under conditions as close as possible to the LHC environment the High Rate Beam Test was conceived. With the help of the CMS group at the Rutherford Appleton Laboratory, UK, the High Rate Pixel Telescope (HRPT) was designed. The HRPT is a low cost and compact beam telescope with eight planes equipped with the new readout chip. A new telescope was necessary since all other available particle tracking telescopes are not able to cope with the high rate of particles the chip should be measuring or are not suited for the high radiation environment the high rate particle beam creates. The HRPT was the first use of the IPBus software and firmware suit in the CMS experiment. For the analysis of the collected data a software framework based on EUTelescope was set up. The High Rate Beam Test was performed in 2014 in the High Rate Tracking Area of the Fermilab Test Beam Facility.

With the data collected in the beam test the hit detection efficiency of the readout chip with respect to the particle rate of the beam was measured. In these measurements unexpected features were found:

- The efficiency does not reach 100% for low particle fluxes.
- The efficiency does not drop as much as expected for high fluxes
- The efficiency for the different WBC settings behaves obverse to expectations.

A full beam test was simulated in order to understand the sources of these features and to ensure that the chip works as expected. Tracks were generated in a Geant4 simulation of beam telescope setup. A simple charge sharing method was implemented to mimic the charge sharing behaviour of the real CMS pixel detector. The readout of the separate telescope planes was simulated with a C++ simulation that was verified against laboratory measurements with X-rays. The simulation revealed several findings about the beam test and the telescope:

- The initial drop of measured efficiency seen for all measurements can be explained by a clock phase mismatch between the particle beam and the readout chip.

- A small misalignment between the sensor planes is not enough to avoid correlations of inefficiencies in the telescope which bias the efficiency measurement towards higher efficiency.
- The flat gradient of measured hit detection efficiency over the measured rate is caused by a combination of effects
  - the correalation between the readout chips,
  - the large beam variations
  - the 'monster' clusters
- A telescope and a separate DUT is superior to a telescope for which the DUT is part of the telescope when it comes to measuring hit detection efficiencies.

Summarising the simulation did not show that the measurements performed with the ROC lay outside of its specifications. The unexpected effects seen during the test beam were caused by external factors and cannot be traced back to the PSI46dig readout chip.

9.3 Recommendations For Futre Beam Tests

Looking at the results of the beam test, confirmed by the simulation, one sees that the efficiency measurement does not correspond to the one expected from X-ray measurements. The main reasons are:

- strong intensity variations, enhanced by the difference of the frequency of the bam and the internal readout chip clock,
- correlation of inefficiencies of the DUT and the telescope, both using the same readout chip.

An ideal beam would be one with a high particle energy, a 40 MHz frequency and a variable intensity, constant within a run. And an ideal telescope should be built with highly efficient detectors. While many beam lines exist that provide high energy particles beams at low rates or low energy beams at high rates, only few beam lines combine high energy with high particle rate as it is found close to the interaction point of the LHC. The measurement of the beam intensity needs to be one of the priorities for this ideal beam, that needs to be done well if detectors should to be tested unter realistic conditions in the future.

A similar picture can be drawn for the currently existing beam telescopes. While most of them, especially the telescopes of the EUDET family, are built for maximum position resolution, no telescope exists that can be used in the high particle rate environment of $> 100\,\mathrm{MHz\,cm^{-2}}$ that is created close to the interaction points of the LHC. Hence a combined effort by the two largest high energy particle physics experiments, ATLAS and CMS, should be made to create a telescope with which tracking detectors for the HL-LHC era can be accurately studied.

Bibliography

[A+08] Y. Allkofer et al. Design and performance of the silicon sensors for the CMS barrel pixel detector. *Nuclear Instruments and Methods in Physics Research Section A: Accelerators, Spectrometers, Detectors and Associated Equipment*, 584(1):25 – 41, 2008.

[Ago03] S. Agostinelli. Geant4 - A simulation toolkit. *Nuclear Instruments and Methods in Physics Research Section A: Accelerators, Spectrometers, Detectors and Associated Equipment*, 506(3):250 – 303, 2003.

[Bar03] M. Barbero. *Development of a radiation-hard pixel read out chip with trigger capability.* PhD thesis, Basel U., Basel, 2003. `https://cds.cern.ch/record/467141`.

[Bar05] E. Bartz. The 0.25um Token Bit Manager Chip for the CMS Pixel Readout, 2005. `https://cds.cern.ch/record/920426`.

[Bar09] E. Bartz et al. The PLT: A luminosity monitor for CMS based on single-crystal diamond pixel sensors. *Nuclear Physics B - Proceedings Supplements*, 197(1):171 – 174, 2009. 11th Topical Seminar on Innovative Particle and Radiation Detectors (IPRD08).

[Bar11] M. Barbero. FE-I4 pixel readout chip and IBL module. Jun 2011. `http://cds.cern.ch/record/1360698`.

[Bel13] A. J. Bell. Luminosity, beam monitoring and triggering for the CMS experiment and measurement of the total inelastic cross-section at $\sqrt{s} = 7$ TeV. 01/23 2013. `http://archive-ouverte.unige.ch/unige:26494`.

[Blo07] V. Blobel. Millepede II – Linear least squares fits with a large number of parameters, May 2007. `http://www.desy.de/~blobel/Mptwo.pdf`.

[Bre11] J. Bregeon. Design and performance of the silicon strip tracker of the fermi large area telescope. *Journal of Instrumentation*, 6(12):C12043, 2011.

[Bur14] A. Burgmeier. *Position Resolution and Upgrade of the CMS Pixel Detector and Search for the Higgs Boson in the $\tau^+\tau^-$ Final State.* PhD thesis, KIT, Karlsruhe, 2014.

[C+12] S. Chatrchyan et al. Observation of a new boson at a mass of 125 GeV with the CMS experiment at the LHC. *Phys. Lett.*, B716:30–61, 2012.

[CDF+09] G. Cerati, M. Dinardo, A. Florez, S. Kwan, A. Lopez, S. Magni, S. Malvezzi, D. Menasce, L. Moroni, C. Newsom, D. Pedrini, M. Rovere, S. Sala, P. Tan, S. Taroni, M. Turqueti, and L. Uplegger. Radiation tolerance of the CMS forward pixel detector. *Nuclear Instruments and Methods in Physics Research Section A: Accelerators, Spectrometers, Detectors and Associated Equipment*, 600(2):408 – 416, 2009.

[CMS10] Measurement of CMS Luminosity . Technical Report CMS-PAS-EWK-10-004, CERN, 2010.

[Col06] T. C. Collaboration. *CMS Physics: Technical Design Report Volume 1: Detector Performance and Software*. Technical Design Report CMS. CERN, Geneva, 2006.

[Col12] T. C. Collaboration. CMS Technical Design Report for the Pixel Detector Upgrade. Technical Report CERN-LHCC-2012-016. CMS-TDR-11, CERN, Geneva, Sep 2012.

[Col13] C. Collaboration. CMS Luminosity Based on Pixel Cluster Counting - Summer 2013 Update. 2013.

[Dab14] A. Dabrowski. Upgrade of the CMS instrumentation for luminosity and machine induced background measurements. Technical Report CMS-CR-2014-362, CERN, Geneva, Oct 2014.

[Dev15] A. Devices. ADCMP604 Rail-to-Rail, Very Fast, 2.5 V to 5.5 V, Single-Supply LVDS Comparator, 2015. `http://www.analog.com/en/products/linear-products/comparators/adcmp604.html`,[Online; accessed 21-October-2015].

[Erd10] W. Erdmann. The CMS pixel detector. *Int.J.Mod.Phys.*, A25:1315–1337, 2010.

[FNA15] Beam delivery path of MTest, 2015. `http://ppd.fnal.gov/ftbf/beam/delivery.html`,[Online; accessed 17-August-2015].

[Fri01] M. Friedl. *The CMS silicon strip tracker and its electronic readout*. PhD thesis, Technische U. Wien, Wien, 2001.

[Gab05] K. Gabathuler. *PSI46 Pixel Chip - External Specification*, 2005.

[GM12] R. Gross and A. Marx. *Festkörperphysik*. Oldenbourg, München, 2012.

[Gra53] F. Gray. Pulse code communication, March 17 1953. US Patent 2,632,058.

[Gri05] D. J. Griffiths. *Introduction to quantum mechanics*. Pearson international edition. Pearson Prentice Hall, Upper Saddle River, NJ, 2. ed edition, 2005.

[Har09] F. Hartmann. *Evolution of silicon sensor technology in particle physics*. Springer, Berlin, 2009.

[HM06] W. Herr and B. Muratori. Concept of luminosity. 2006. `https://cds.cern.ch/record/941318`.

[Ins15a] T. Instruments. 8-PORT LVDS REPEATER (SN65LVDS108), 2015. `http://www.ti.com/lit/ds/slls399e/slls399e.pdf`,[Online; accessed 21-October-2015].

[Ins15b] T. Instruments. DS90LV001 800 Mbps LVDS Buffer, 2015. `http://www.ti.com/lit/ds/symlink/ds90lv001.pdf`,[Online; accessed 21-October-2015].

[K+06] H. Kästli et al. Design and performance of the CMS pixel detector readout chip. *Nuclear Instruments and Methods in Physics Research Section A: Accelerators, Spectrometers, Detectors and Associated Equipment*, 565(1):188 – 194, 2006. Proceedings of the International Workshop on Semiconductor Pixel Detectors for Particles and Imaging PIXEL 2005 International Workshop on Semiconductor Pixel Detectors for Particles and Imaging.

[Kle14] K. Klein. The DC-DC Conversion Power System of the CMS Phase-1 Pixel Upgrade. Technical Report CMS-CR-2014-354, CERN, Geneva, Oct 2014.

[Kli07] C. Klingshirn, editor. *Semiconductor Optics*. Springer-Verlag, Berlin, 3rd edition, 2007.

[L+15] C. G. Larrea et al. IPbus: A flexible ethernet-based control system for μTCA hardware. *Journal of Instrumentation*, 10(02):C02019, 2015.

[LHC15] LHCb Outreach. The LHCb Detector, 2015. `http://lhcb-public.web.cern.ch/lhcb-public/Objects/Detector/CERNMap.jpg`,[Online; accessed 07-November-2015].

[Loo15] R. Loos. private communication, 2015.

[Man04] R. Mankel. Pattern recognition and event reconstruction in particle physics experiments. *Reports on Progress in Physics*, 67:553–622, April 2004.

[Mol99] M. Moll. *Radiation damage in silicon particle detectors: Microscopic defects and macroscopic properties*. PhD thesis, Hamburg U., 1999.

[O'L15] C. O'Luanaigh. Low-energy collisions tune LHC experiments, 2015. `http://home.web.cern.ch/about/updates/2015/05/low-energy-collisions-tune-lhc-experiments`,[Online; accessed 18-July-2015].

[Pit15] D. Pitzl. private communication, 2015.

[R+04] T. Rohe et al. Fluence Dependence of Charge Collection of irradiated Pixel Sensors. *Nucl. Instrum. Methods Phys. Res., A*, 552(physics/0411214. 1-2):232–238. 11 p, Nov 2004. `http://cds.cern.ch/record/807069`.

[Ros06] L. Rossi. *Pixel Detectors : from fundamentals to applications; with 177 Figures*. Particle Acceleration and Detection. Springer, Berlin, 2006.

[Rub12] I. Rubinskiy. An EUDET/AIDA Pixel Beam Telescope for Detector Development. *Physics Procedia*, 37:923 – 931, 2012. Proceedings of the 2nd International Conference on Technology and Instrumentation in Particle Physics (TIPP 2011).

[S+05] A. Starodumov et al. Qualification Procedures of the CMS Pixel Barrel Modules. *Nucl. Instrum. Methods Phys. Res., A*, 565(physics/0510165):67–72. 7 p, Oct 2005.

[Sem15] O. Semiconductor. NB7L86M 2.5V/3.3V 12 Gb/s Differential Clock/Data SmartGate, 2015. `http://www.onsemi.com/pub_link/Collateral/NB7L86M-D.PDF`,[Online; accessed 21-October-2015].

[SM14] T. Sakuma and T. McCauley. Detector and Event Visualization with SketchUp at the CMS Experiment. *J. Phys. Conf. Ser.*, 513:022032, 2014.

[Spa] S. Spannagel. A High-Rate Beam Test for the CMS Pixel Detector Phase I Upgrade. Karlsruhe Institute of Technology, Diplomarbeit, 2012.

[Spi06] H. Spieler. *Semiconductor detector systems*. Series on semiconductor science and technology ; 12. Oxford Univ. Press, Oxford [u.a.], repr. edition, 2006.

[TLP08] P. Trüb, U. Langenegger, and F. Pauss. *CMS pixel module qualification and Monte-Carlo study of $H \to \tau^+\tau^- \to l^+l^- ET$*. PhD thesis, Zurich, ETH, 2008. presented 2008.

[vdM68] S. van der Meer. Calibration of the effective beam height in the ISR. Technical Report CERN-ISR-PO-68-31. ISR-PO-68-31, CERN, Geneva, 1968.

[Ves13] V. Veszpremi. Operation and performance of the CMS tracker. Technical Report CMS-CR-2013-437, CERN, Geneva, Nov 2013.

[Xil15] Xilinx. Spartan-6 FPGA SP605 Evaluation Kit, 2015. `http://www.xilinx.com/products/boards-and-kits/ek-s6-sp605-g.html`,[Online; accessed 21-October-2015].

[Ye92] R. Yarema et al. A fast, wide range charge integrator and encoder asic for photomultiplier tubes. In *Nuclear Science Symposium and Medical Imaging Conference, 1992., Conference Record of the 1992 IEEE*, pages 381–383 vol.1, Oct 1992.

List of Figures

List of Tables